DISSERTATION

BRILLOUIN LIGHT SCATTERING SPECTROSCOPY OF PHONONS, MAGNONS, AND MAGNETOELASTIC WAVES

Submitted by

Katherine Elise Nygren

Department of Physics

In partial fulfillment of the requirements

For the Degree of Doctor of Philosophy

Colorado State University

Fort Collins, Colorado

Fall 2022

Doctoral Committee:

Advisor: Kristen S. Buchanan

Stuart Field
Samuel Brewer
Matthew Shores

Copyright by Katherine Elise Nygren 2022

All Rights Reserved

ABSTRACT

BRILLOUIN LIGHT SCATTERING SPECTROSCOPY OF PHONONS, MAGNONS, AND MAGNETOELASTIC WAVES

This thesis discusses three projects that involve the propagation of waves through the utilization of an optical measurement technique known as Brillouin light scattering (BLS) spectroscopy. BLS spectroscopy measurements were completed using a six pass tandem Fabry-Pérot interferometer to detect light that has inelastically scattered from vibrational, spin, or magnetoelastic waves in a sample. This measurement method is noncontact, so wires do not need to be connected to the sample, nondamaging (unless the laser power is too high, and only for sensitive samples), and can detect nonlinear signals.

The first project uses an antenna called an interdigital transducer to produce a surface acoustic wave. This wave travels across a piezoelectric substrate and couples to a spin wave in a nickel film. The coupled wave known as a magnetoelastic wave is then studied using BLS as a function of the external applied magnetic field. These results are used to help us understand how the magnetic resonance contributes to the coupled wave. Further BLS measurements as a function of distance across the nickel film are used to calculate a decay length of the magnetoelastic wave two orders of magnitude larger than the decay length for a pure spin wave in nickel.

Second, we explore a device using a thin film of an organic ferrimagnet called vanadium tetracyanoethylene (VTCNE) that is magnetic at room temperature and has low damping, which rivals damping in high quality YIG films commonly used in microwave applications. Because VTCNE is oxygen sensitive it is encapsulated between two pieces of glass using an epoxy. The encapsulation does not change the damping, however due to magnetostriction, the strain of the epoxy may change the magnetic properties of the film. To understand how the epoxy strain can effect this device and others with similar encapsulation, we study thermal phonons in the encapsulation materials using

Brillouin light scattering. The thermal phonon measurements along with phonon simulations allow us to calculate both the wave speeds and the elastic properties of the materials. These calculated properties can then be used to model future VTCNE devices.

The final major project uses BLS spectroscopy to study spin waves in a Y-shaped structure of an iron nickel alloy. Using an in-plane externally applied magnetic field and an antenna across the top of the Y, we excite magnons in each arm of the Y, which then propagate into the base of the Y. BLS measurements are taken in each arm and the base of the Y, as a function of the driving frequency, and a 2D spatial map of the spin waves in the Y-structure was obtained to gain additional information on the modes that propagate past the junction of the Y. The BLS data in conjunction with simulations, demonstrate an indirect way to efficiently excite Damon-Eshbach spin waves as well as convert low wavevector spin waves in the arms of the Y into higher wavevector spin waves as they propagate into the base of the Y. The wavevector conversion and more efficient method of generating Damon-Eshbach spin waves are tools that can be exploited in magnonic device designs.

Three additional spin wave projects are also discussed briefly. The projects include a yttrium iron garnet (YIG) confined structure, a VO_2 film with a metal-insulator-transition near room temperature, and a heavy metal-ferrimagnet-heavy metal sample that should have a strong interfacial Dzyaloshinskii-Moriya interaction.

ACKNOWLEDGEMENTS

My graduate career and this thesis would not have have been possible without the support of many different people. First and foremost, I would like to thank my advisor Kristen Buchanan for her patience, guidance, and encouragement while navigating all the twists and turns of research. Her commitment to pursuing and sharing new science, along with her financial support, has lead to some truly amazing and unique experiences at meetings, conferences, and an interferometer training.

I am indebted to the graduate students who came before me, Jason Liu and Grant Riley, who have taught me so much about BLS and gave me practical lab advice to keep research progressing as smoothly as possible through some of the common hiccups of our system. David Marchfield and Mitchell Swyt thank you for all of your help running long BLS scans. You guys shared my enthusiasm when research was going well and were also there to commiserate when it wasn't.

A big thank you to Carl Patton for asking the hard questions and getting me to think critically about the small details, while always being ready to discuss my questions about magnetization dynamics. I would also like to thank Stuart Field and Gus DeMann for all of their photolithography help.

My family and friends outside of school, you have have helped keep me grounded and I appreciated your occasional insistence that I get out of the lab and come to lunch with you. To my mom, thank you for always being my role model, instilling a love of science in me, and helping me to keep things in perspective.

For the VTCNE project discussed in Chapter 5, the sample design and fabrication, measurements, and theory work was all funded by National Science Foundation DMR award number 1741666.

For the Y-structures project discussed in Chapter 6, fabrication using photolithography facilities was supported by the National Science Foundation under Grant No. NSF-DMR 1727044, the measurements and simulations at Colorado State University were supported by the W. M. Keck

Foundation and fabrication at CSU was further funded by the National Science Foundation DMR grant number 1709525.

DEDICATION

I want to dedicate this dissertation to my family for their love, unwavering support, and encouragement to stay curious and follow my dreams.

TABLE OF CONTENTS

ABSTRACT ii
ACKNOWLEDGEMENTS iv
DEDICATION vi
LIST OF TABLES ix
LIST OF FIGURES x
LIST OF SYMBOLS xii
LIST OF ACRONYMS xiii

Chapter 1 Introduction 1
1.1 Motivation 1
1.2 Objectives 1
1.3 Thesis Outline 2

Chapter 2 Waves Introduction 4
2.1 Phonon Introduction 4
2.1.1 Motion 4
2.1.2 Elastic Constants 7
2.2 Magnon Introduction 10
2.2.1 Static Magnetization and Magnetic Fields 10
2.2.2 Dynamic Magnetization: Ferromagnetic Resonance and Spin waves . . 11
2.3 Magnetoelastic Waves 15

Chapter 3 Measurement Techniques/Methods 17
3.1 Brillouin Light Scattering 17
3.1.1 Sample Interaction 19
3.1.2 Interferometer 24
3.1.3 BLS Configurations 34
3.1.4 BLS Software 38
3.1.5 Other BLS Capabilities 43
3.2 Vector Network Analyzer 44
3.3 Cavity Ferromagnetic Resonance 47
3.4 Magnetometry 48
3.5 Summary 49

Chapter 4 Magnetoelastic Waves Generated by Surface Acoustic Waves 50
4.1 Context 50
4.2 Motivation 50
4.3 Sample Design and Fabrication 53
4.4 Experimental Set Up 56
4.5 Electrical (VNA) Measurements 57
4.6 BLS Measurements 61

4.7 Summary and Future Directions . . . 68

Chapter 5 Vanadium Tetracyanoethylene . . . 70
5.1 Context . . . 70
5.2 Sample Design . . . 71
5.3 Experimental Setup . . . 73
5.4 Experimental Results . . . 75
5.5 Phonon Simulations . . . 81
5.6 Ongoing Work and Future Directions . . . 87
5.7 Summary . . . 90

Chapter 6 Spin wave up conversion of K-vectors in Y structures . . . 91
6.1 Context . . . 91
6.2 Paper Overview . . . 91
6.3 Research Article . . . 92
6.4 Summary and Future Directions . . . 100

Chapter 7 Other Projects . . . 101
7.1 Yttrium Iron Garnet Confinement and Traveling Waves . . . 101
7.2 Vanadium Oxide Spin Waves . . . 104
7.3 Dzyaloshinskii-Moriya Interaction Measurements . . . 105

Chapter 8 Conclusions . . . 108
8.1 Summary . . . 108

Bibliography . . . 110

Appendix A Supplemental Materials: Spin wave up conversion of K-vectors in Y structures 131

LIST OF TABLES

2.1 Elastic Constants and Moduli 9

5.1 Glass Phonon Simulation Parameters 84
5.2 Glass-Epoxy-Glass Phonon Simulation Parameters 85
5.3 VTCNE Elastic Moduli 87
5.4 Glass-VTCNE-Epoxy-Glass Phonon Simulation Parameters 88

LIST OF FIGURES

2.1 Phonon Modes . . . 6
2.2 Kittel Equation for a Nickel Film . . . 13
2.3 Magnon Dispersion Curves . . . 15

3.1 Feynman Diagram for BLS Scattering . . . 20
3.2 Effect of Using 2 Fabry-Pérot Etalons in Tandem . . . 25
3.3 Effect of Using a Scanning Interferometer . . . 26
3.4 Beam Paths Inside the TFP1 Interferometer . . . 27
3.5 TFPDAS4 Reflection Mode . . . 28
3.6 Plexiglas Alignment Check . . . 30
3.7 Beam Paths Inside the TFP2-HC Interferometer . . . 33
3.8 D4B BLS Optical Table Beam Paths . . . 36
3.9 D8 BLS Optical Table Beam Paths . . . 37
3.10 GHOST . . . 39
3.11 MicroBLS Software Windows . . . 41
3.12 Micro-BLS Camera Image Transformation . . . 42
3.13 Frequency Swept FMR . . . 45
3.14 Smith Chart . . . 47
3.15 Field Swept FMR . . . 48
3.16 Hysteresis . . . 49

4.1 Magnetostriction in Nickel . . . 52
4.2 SAW-BLS Processes . . . 53
4.3 XY Map of Magnetoacoustic Coupling Intensity . . . 55
4.4 SAW Sample Micrographs . . . 56
4.5 SAW Sample Schematic . . . 57
4.6 Delay Line Characterization . . . 58
4.7 SAW-Nickel Transmission: S31 . . . 59
4.8 Nickel Absorption: S33 . . . 60
4.9 Nickel Absorption: S31-BLS . . . 62
4.10 Measurement Positions on Micro-BLS camera . . . 63
4.11 BLS Scans for SAW Sample . . . 64
4.12 Nickel Dispersion Curves . . . 66
4.13 Magnetoelastic Decay Lengths . . . 67

5.1 CVD Deposition of VTCNE . . . 72
5.2 VTCNE Encapsulation . . . 73
5.3 Encapsulation Materials Frequency vs. Angle (θ) Fits . . . 74
5.4 Visible Laser Damage of VTCNE . . . 75
5.5 Glass BLS Measurements . . . 76
5.6 Glass-Epoxy BLS Measurements . . . 78
5.7 Encapsulation Materials Frequency vs. Angle (θ) Fits . . . 80

5.8 Glass Dispersion Curves 84
5.9 Glass-Epoxy-Glass Dispersion Curves 86
5.10 Glass-VTCNE-Epoxy-Glass Dispersion Curves 89

6.1 BLS Scans of Y-Structure at Select Locations 94
6.2 2D Spatial BLS Map of Y-Structure 96
6.3 Y-structure Micromagnetic Simulations 97

7.1 YIG-Resonator Alignment 102
7.2 VNA Resonances 103
7.3 Antennas for VO_2 Excitation 104
7.4 DMI Measurements at Varying Angle 107

A.1 Y-structure Micromagnetic Animation Still 45° Case 132
A.2 Y-structure Micromagnetic Animation Still Y Case 133
A.3 Y-structure Micromagnetic Animation Still Y Case Skewed Field 134
A.4 Y-structure Wavevector Components Diagram 135
A.5 Strip Width Dependence of Sample Properties 137

LIST OF SYMBOLS

α	longitudinal bulk speed	(m/s)
β	transverse bulk speed	(m/s)
C	elastic moduli	(Pa)
ϵ	strain	(unitless)
f	frequency	(Hz)
$\gamma/2\pi$	Gyromagnetic ratio	(Hz/Oe)
H	Magnetic field	(Oe)
k	Wavevector	(rad/μm)
$k_\perp$	Wavevector perpendicular to the sample surface	(rad/μm)
$k_\parallel$	Wavevector parallel to the sample surface	(rad/μm)
λ	Wavelength	(nm)
M	Magnetization	(emu/cm^3)
$4\pi M_s$	Magnetic Saturation	(Oe)
N	Demagnetization factor	(unitless)
q_i	Incident photon wavevector	(rad/μm)
q_s	Incident photon wavevector	(rad/μm)
ρ	density	(g/cm^3)
σ	stress	(N/m^2)
t	thickness	(nm)
ω	angular frequency	(rad/s)

LIST OF ACRONYMS

BLS . . . . . Brillouin light scattering

BVSW . . . . . Backward volume spin wave

DE . . . . . Damon-Eshbach

DM/DMI . . . . . Dzyaloshinskii-Moriya interaction

FMR . . . . . Ferromagnetic resonance

FP1 . . . . . First Fabry-Pérot cavity

FP2 . . . . . Second Fabry-Pérot cavity

FSR . . . . . Free spectral range

FVSW . . . . . Forward volume spin wave

GGG . . . . . Gadolinium gallium garnet

IDT . . . . . Interdigital transducer

LB . . . . . Longitudinal bulk mode

$LiNbO_3$ . . . . . Lithium niobate

LM . . . . . Longitudinal surface mode

MCD . . . . . Magnetic circular dichroism

MOKE . . . . . Magneto-optic Kerr effect

PEEM . . . . . Photoemission electron microscopy

PSSW . . . . . Perpendicular standing spin wave

ROI . . . . . Region of interest

RW . . . . . Rayleigh wave

SAW . . . . . Surface acoustic wave

SHM . . . . . Shear horizontal mode

SiO_2 . . . . . Silicon dioxide

SQUID . . . . . Superconducting quantum interference device

TFP . . . . . Tandem Fabry-Pérot interferometer

TFPDAS4 . . . . . Tandem Fabry-Pérot data acquisition software (version 4)

TR-BLS . . . . . Time resolved Brillouin light scattering

VNA . . . . . Vector network analyzer

VNA-FMR . . . . . Vector network analyzer ferromagnetic resonance

VSM . . . . . Vibrating sample magnetometer

VTCNE . . . . . Vanadium tetracyanoethylene

XMCD . . . . . X-ray magnetic circular dichroism

YIG . . . . . Yttrium iron garnet

Chapter 1

Introduction

1.1 Motivation

Technology is constantly growing in use and capacity, but research into materials and new applications is required to meet society's demand for smaller more efficient products that are affordable and use materials that are sustainable. This involves research into new materials that can replace existing materials that may be harmful to people or the environment, or to find and exploit a new functionality of a material.

Transistors are the key to electronic devices with the integrated circuitry semiconductor industry worth over 500 billion dollars annually [1]. Transistors currently range in scale from 3 - 22 nm, with a frequency less than 10 GHz but are becoming more difficult to scale down or speed up due to reaching a power dissipation limit from large ohmic heating associated with the electrical resistance of a device [1]. Using alternative signals like surface acoustic waves or spin waves would remove or reduce the need for electrical currents and thereby the heating losses, but these waves need further research into their behavior in confined structures and on the nanoscale before they can be used in widespread commercial applications [1, 2].

Our lab uses a versatile measurement technique called Brillouin light scattering (BLS) spectroscopy that uses a laser and interferometer to study different types of waves in a variety of materials. BLS measurements are used in many areas of science, technology, and engineering to research material properties and how propagating waves behave in a variety of structures.

1.2 Objectives

The focus of this thesis is to measure phonons, spin waves (magnons), and magnetoelastic waves using the Brillouin light scattering measurement technique. Phonon measurements by BLS can give insight into the wave speeds and elastic properties of a material, whereas magnon BLS

measurements can better our understanding of domain wall motion or signal interactions for device applications. We can combine the best of magnons and phonons through magnetoelastic waves and study new control methods and functionality with BLS.

1.3 Thesis Outline

The following describes the structure of this thesis.

An introduction to waves is presented in Chapter 2. The motion of bulk and surface phonons are discussed, along with the elastic tensor and how the elastic moduli relate to phonon wave speeds and elastic constants. Then, ferromagnetic resonance and magnon dispersion relations are discussed with respect to thin films and defining geometries. Lastly magnetoelastic waves are discussed in terms of the phonon-magnon coupling through the magnetostriction of a material.

Chapter 3 describes the Brillouin light scattering (BLS) sample interaction, and then moves on to discuss the interferometer. An overview of the three measurement configurations used in our lab along with the fundamentals of the software interfaces is also discussed. The vector network analyzer is discussed in terms of ferromagnetic resonance measurements as well as transmission and reflection "S" measurements. Two magnetometry measurement methods are mentioned as they relate to BLS and magnetic calculations.

The surface acoustic wave (SAW) project is discussed in Chapter 4, where a microwave signal is used with an interdigital transducer to launch a surface acoustic wave across a $LiNbO_3$ substrate to interact with a small nickel film. The magnetoelastic wave produced in the nickel film is studied as a function of external magnetic field and distance from the front edge of the film. The measurements in this chapter were taken by VNA and by our micro-BLS system.

Chapter 5 describes a project involving an organic ferrimagnet called vanadium tetracyanoethylene, or VTCNE. The sample deposition method is briefly discussed before looking at BLS measurements and phonon simulations to characterize the encapsulation materials' elastic properties. VTCNE elastic properties are discussed along with new sample designs.

A paper exploring spin waves in a Y-shaped structure is presented in Chapter 6. Simulations and BLS mode maps are examined to understand what happens to spin waves traveling along the arm of an iron-nickel alloy in the shape of a Y, and what happens when the spin waves join together and continue traveling into and along the base of the Y.

Chapter 7 includes three spin wave projects that investigate structure confinement, the interfacial Dzyaloshinskii-Moriya interaction, and the dispersion relations around a metal-insulator transition temperature. These projects did not have a definite outcome, but were crucial to finding ways our research group could take better BLS data.

Chapter 8 will give summary of the projects presented in this thesis and some comments on improvements of our BLS systems.

Chapter 2

Waves Introduction

Waves are not only abundant in our daily lives, they are unavoidable. From waves at a beach, to earthquakes, to sound waves, to light, to our microwave ovens, to the radio or television broadcast, to the waves we use to wirelessly connect to the internet, we are constantly surrounded by waves. These wave examples are both on the macro-scale as well as the micro-scale, and include vibrational waves between atoms in a material called phonons, and electromagnetic waves that allow us to see color or communicate wirelessly. Other waves include magnetic waves of precessing electron spins often called spin waves, and waves that combine spin waves and phonons called magnetoelastic waves. This thesis will discuss phonons, spin waves, and magnetoelastic waves.

2.1 Phonon Introduction

Phonons are the quasi-particle for vibrational waves. This section will discuss phonon motion and speeds, ways the different phonons can be identified and distinguished from each other, as well as how these phonons can be used to describe material parameters of a sample [3–5].

2.1.1 Motion

Longitudinal modes (LM) involve stretching and compression of a material along the propagation direction. A common example of this is sound waves, where the pressure differences in air from the wave compression is what the human ear picks up on. The other general type of wave is a transverse wave, where the atom motion is perpendicular to the direction of the overall propagation direction. A couple of examples include waves on a string or a ripple across the surface of water. Some modes are confined to a surface or interface while others can travel through the bulk of a material, referred to as surface or bulk modes, respectively. There are both bulk longitudinal as well as bulk transverse waves. Bulk transverse waves are difficult but not impossible to measure by BLS, however they can be readily measured using other techniques in many cases. There are

also surface longitudinal waves, but the surface transverse waves have more specific material conditions, motion patterns, and names that include but are not limited to Love waves [6, 7], Rayleigh waves [8–12], Stoneley waves [10–16], Sezawa waves [16–18], and Lamb waves [19–21]. Shear horizontal surface waves are also called Love waves, however I will refer to them as waves from a shear horizontal mode (SHM) to avoid possible confusion with multiple waves starting with "L". For a shear horizontal surface wave, the atoms move from side to side as the wave moves forward, similar to how a snake or a shark would move. The Rayleigh wave (RW) is strictly a surface wave that decays exponentially as it travels deeper into a film, but this motion looks very similar to a ripple on water or how an inch worm might move; however, the atoms actually follow an elliptical path. This means that while most of the motion is up and down, perpendicular to the direction of motion, there is also motion along the direction the wave is propagating.

Figure 2.1 shows diagrams of the motion patterns for common elastic waves. Figure 2.1 also displays the material wavevector Q and the laser wavevector k_i, though in this thesis a different notation is used where the wavevector of the wave in the material will be called k and the laser wavevector is $q_i = 2\pi/\lambda_{\text{laser}}$. This will be discussed in more detail in Section 3.1.1.

Due to the different motion patterns, each of the waves discussed above has a different wave speed. Longitudinal waves are faster than their transverse counterparts, and bulk modes are typically a little faster (10% or less) compared to surface modes with similar motion. For example, in Chapter 5, we will calculate a longitudinal bulk wave speed of 5623 m/s for glass, and a longitudinal surface wave in the same material of 5414 m/s, which is a difference of a little less than 4%. A longitudinal surface wave will also be quite a bit faster than any transverse surface wave. Again in Chapter 5 we will calculate a surface shear horizontal mode wave speed for glass of 3268 m/s, which is well below the 5414 m/s surface longitudinal wave speed. Shear horizontal waves tend be slightly faster than Rayleigh waves, in the same material. These rough wave speed relationships can help identify what waves are measured, though a little more information will be needed, again discussed further in Section 5.4 with our actual data and results.

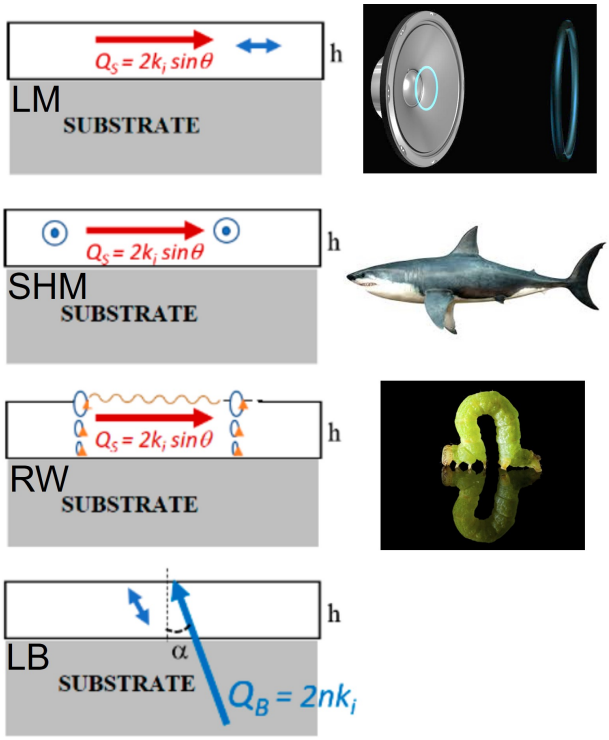

Figure 2.1: Diagram showing longitudinal bulk (LB), longitudinal surface (LM), shear horizontal (SHM), and Rayleigh (RW) surface mode propagation motions along with an analogous motion for a better visual representation. A thin film (white) on top of a much thicker substrate (grey), with the red arrows denoting the propagation direction (to the right) in the surface mode diagrams, with the small blue notations denoting the vibration oscillation direction. In the LB diagram, the large blue arrow at an angle α denotes the wavevector propagation direction the measurement system is sensitive to based on the optical refraction of the laser light in the thin film. The small blue arrow again denotes the vibration oscillation direction. The equations in each diagram are for the measurable wavevector Q_s and Q_B, corresponding to a surface and bulk wave respectively. The incoming laser wavevector is k_i, and where surface waves are sensitive to the angle θ from the sample normal, bulk waves are sensitive to the material's index of refraction n. Figure adapted from Ref. [3].

The motion of these waves can quickly get more complicated for three dimensional materials, especially for low symmetry materials. In some materials, called isotropic materials, all of the axis directions are equivalent so the stiffness and elastic moduli along those axes are all the same. There are also anisotropic materials where elastic constants and hence the wave speeds vary with direction.

2.1.2 Elastic Constants

Elastic waves are typically described mathematically using elastic constants and Hooke's law. According to Hooke's law, the stress σ_{ij} is the force per area applied to the material

$$\sigma_{ij} = [C_{ijkl}]\,\epsilon_{kl}, \tag{2.1}$$

where ϵ_{kl} is the strain, and $[C_{ijkl}]$ is the material's elastic tensor or stiffness tensor, containing individual C values known as the elastic moduli.

To explain the physical characteristic the elastic tensor describes, if you were to poke a piece of Jello the force your finger applies is the stress, and how far the Jello flexes or stretches is the strain. For gentle finger pokes, once you stop pushing on the Jello, it will return to its original shape. If you were to poke the surface of a solid metal block with the same force as the Jello, the metal would deform far less, if at all, as seen by the naked eye. The difference between the Jello and the metal block is described by their different elastic moduli. Soft materials, like Jello, have elastic moduli (C_{ijkl}) with lower magnitudes when compared to hard materials, like the metal block. In the limit of small deformations, the linear Hooke's law applies (Equation (2.1)). However, if you were to push your finger into the Jello hard enough to tear or otherwise damage the Jello, you would be in the nonlinear regime since the Jello would no longer be able to return to its original state. Most situations in this thesis deal with the linear regime.

For a three dimensional system described by axes X, Y, and Z, Equation (2.1) can be expanded to its tensor form

$$\begin{bmatrix} \sigma_{XX} \\ \sigma_{YY} \\ \sigma_{ZZ} \\ \sigma_{YZ} \\ \sigma_{ZX} \\ \sigma_{XY} \end{bmatrix} = \begin{bmatrix} C_{11} & C_{12} & C_{13} & C_{14} & C_{15} & C_{16} \\ C_{21} & C_{22} & C_{23} & C_{24} & C_{25} & C_{26} \\ C_{31} & C_{32} & C_{33} & C_{34} & C_{35} & C_{36} \\ C_{41} & C_{42} & C_{43} & C_{44} & C_{45} & C_{46} \\ C_{51} & C_{52} & C_{53} & C_{54} & C_{55} & C_{56} \\ C_{61} & C_{62} & C_{63} & C_{64} & C_{65} & C_{66} \end{bmatrix} \begin{bmatrix} \epsilon_{XX} \\ \epsilon_{YY} \\ \epsilon_{ZZ} \\ 2\epsilon_{YZ} \\ 2\epsilon_{ZX} \\ 2\epsilon_{XY} \end{bmatrix}.$$

Where the requirements that $\sigma_{ij} = \sigma_{ji}$ and $C_{ijkl} = C_{jikl}$ have been applied, symmetry arguments can be used to simplify the elastic tensor. Different lattice structures, cubic or hexagonal, will produce further simplification. A fully isotropic case, where all three axis directions are identical, will reduce the elastic tensor further by not only eliminating the upper right and lower left quadrants, but also by reducing the number of independent elastic constants. The simplified tensor is shown below where each elastic constant is highlighted with a different color. As noted in Table 2.1, for a fully isotropic case there are only two independent elastic constants since C_{11} is related to C_{12} and C_{44}.

$$\left[\begin{array}{ccc|ccc} C_{11} & C_{12} & C_{12} & & & \\ C_{12} & C_{11} & C_{12} & & 0 & \\ C_{12} & C_{12} & C_{11} & & & \\ \hline & & & C_{44} & 0 & 0 \\ & 0 & & 0 & C_{44} & 0 \\ & & & 0 & 0 & C_{44} \end{array}\right].$$

Our system discussed in Chapter 5 is a transverse isotropic system, which means one plane, in this case, the horizontal XY plane, is isotropic but the vertical Z axis is different from the other two. This is due to the chemical structure, molecule shape, and unbonded atoms along Z. More complex than the isotropic case, the transverse isotropic elastic tensor is

$$\left[\begin{array}{ccc|ccc} C_{11} & C_{12} & C_{13} & & & \\ C_{12} & C_{11} & C_{13} & & 0 & \\ C_{13} & C_{32} & C_{33} & & & \\ \hline & & & C_{44} & 0 & 0 \\ & 0 & & 0 & C_{44} & 0 \\ & & & 0 & 0 & C_{66} \end{array}\right].$$

Elastic constants are commonly used for comparisons between materials to understand how hard or soft they are and the expected wave speeds with their corresponding frequencies. They can also be used in simulations or calculations to model a material in a certain environment or device. To make full use of the elastic constants, possessing information of the crystal symmetry will lead to more accurate simmulations when modeling material properties (e.x. conductivity, critical temperature, saturation magnetization).

Table 2.1: A table of common elastic constants for an isotropic material.

Elastic constant name	Variable	Elastic moduli	Other relationships
Lamé first parameter	λ	C_{12}	—-
Lamé second parameter	μ	C_{44}	$= G$
Shear modulus	G	C_{44}	$= \mu$
Young's modulus	Y (sometimes E)	C_{11}	$= \lambda + 2\mu$
Bulk modulus or incompressibility	K	—-	$= \lambda + \frac{2\mu}{3}$
Poisson's ratio	ν	—-	$= \frac{Y}{2G} - 1 = \frac{\lambda}{2(\lambda+G)}$

As previously mentioned, we can also use the elastic moduli to find the bulk wave speeds. For our transversely isotropic system, there are two different transverse wave speeds; the shear wave speed in the XY plane, and a wave speed that also includes the structural difference in the Z direction.

$$\alpha = \sqrt{\frac{C_{11}}{\rho}} = \text{ longitudinal bulk speed} \tag{2.2}$$

$$\beta_{XY} = \sqrt{\frac{C_{66}}{\rho}} = \text{ XY transverse bulk speed} \tag{2.3}$$

$$\beta_{Z} = \sqrt{\frac{C_{44}}{\rho}} = \text{ Z transverse bulk speed} \tag{2.4}$$

The phonons measured in Chapter 5 are thermal phonons that are not created by external excitation like an antenna or an optical pulse. However in Chapter 4, we create a surface acoustic wave or SAW with an antenna on a piezoelectric substrate. The SAW used in this work is a Rayleigh wave, discussed earlier, which looks similar to a gentle ripple across the top surface of water.

2.2 Magnon Introduction

While phonons are the quasi-particle for vibrational waves, magnons are the quasi-particle for magnetic waves called spin waves. This section discusses the geometries and motion that define different spin waves as well as some description of how these waves can be used. The name spin wave comes from the fact that this is not a wave where an atom's physical motion traces out a wave shape, but instead involves the motion of a magnetization vector where the magnetization is related to the electron's spin.

2.2.1 Static Magnetization and Magnetic Fields

Before discussing magnetic spin waves in samples, it may be helpful to mention the types of magnetic materials we use for our samples. The majority of sample materials we use are ferromagnetic. Ferromagnets are also known as "permanent" magnets because the material maintains a net magnetization without an externally applied magnetic field. Common ferromagnets include iron, nickel, and cobalt, which can be deposited on a sample via RF or magnetron sputtering to create a film. A ferrimagnet is similar to the ferromagnet and has an overall net magnetization, but there is a sublattice that has a magnetization that points in the opposite direction of the overall sample magnetization, thereby reducing the overall sample magnetization. For the purpose of this thesis the ferrimagnets used are approximated as weak ferromagnets. There are numerous other types of magnetic structures beyond just ferro- and ferri-magnets, though they will not be discussed in this thesis.

The majority of the ferromagnetic samples that we study in the lab are thin films, though some samples are patterned structures like the Y-structure investigated in Chapter 6. The shape

of the magnetic material contributes to the magnetization through anisotropy (discussed above) or demagnetization factors (discussed below) and also factors into how spin waves behave in the sample.

2.2.2 Dynamic Magnetization: Ferromagnetic Resonance and Spin waves

While the sample shape can effect how spin waves propagate, there will be a simple form of magnetization dynamics in the sample called ferromagnetic resonance (FMR) or the uniform precession mode, that will be independent of the material's shape in a sample. A magnetic material placed in a magnetic field will precess when it is perturbed from equilibrium. This is implemented in the lab by placing the sample into a strong uniform external magnetic field $\overrightarrow{H}$, to align all of the magnetic moments from the electron spins. Then a small magnetic perturbation field $\overrightarrow{m}$, often from an antenna, is used to kick the magnetization vector $\overrightarrow{M}$ slightly away from the external field where the vector would prefer to align. This slight misalignment between the external magnetic field and the sample magnetization creates a torque on the spin magnetic moment causing it to precess or rotate around the external field direction. The torque is

$$\overrightarrow{\tau} = -|\gamma| \overrightarrow{M} \times \overrightarrow{H}, \tag{2.5}$$

where γ is the gyromagnetic ratio. This motion is called Larmor precession and looks very similar to the motion of a tether ball if the external field was pointing down the pole into the ground, and the string holding the ball was the magnetization vector. If nobody perturbs the tether ball after the initial hit, it will slowly lose energy and spiral closer to the pole until it eventually hangs straight down along the pole. So long as the sample is not perturbed, the magnetization vector will also slowly align with the external field again, due to a process called damping. One tether ball is like one electron's spin magnetization; to understand FMR and describe magnetic motion across the whole sample, you would need a large field of tether ball setups all moving at the same speed (frequency) and at the same point (phase) where all of the balls are on the west side of the pole at the same time. The frequency of this precession is dependent on the shape of the sample and

the saturation magnetization of the sample material. The equation to determine this frequency is called the Kittel equation, named after Charles Kittel who developed the equation in 1948 [22]. The frequency is

$$\omega_0 = |\gamma| \sqrt{\left(H + (N_y - N_z)4\pi M_s\right)\left(H + (N_x - N_z)4\pi M_s\right)}, \tag{2.6}$$

given in CGS units, where γ is the gyromagnetic ratio, H is the external field, $4\pi M_s$ is the saturation magnetization of the sample, and N_x, N_y, and N_z are the demagnetization factors. Crystal anisotropy is ignored here. Equation (2.6) is a general form and can be simplified for certain geometries and external field H orientations. For thin films that can be approximated as being infinite length in the plane of the film and finite thickness, the simplified form for a field pointing out-of-plane (along z), N_z = 1, N_x = N_y = 0, and the frequency will simplify to

$$\omega_0 = |\gamma| \left(H - 4\pi M_s\right). \tag{2.7}$$

Likewise, for a field pointing in-plane (along x), N_x = 1 and N_y = N_z = 0,

$$\omega_0 = |\gamma| \sqrt{H\left(H + 4\pi M_s\right)}, \tag{2.8}$$

which is shown in Figure 2.2 for the nickel film discussed in Chapter 4.

Unlike the uniform precession of the ferromagnetic resonance, spin waves have a phase difference between neighboring spins. This phase difference is where the wave motion comes in. As the spins precess, following a specific magnetization orientation from one spin to the next will result in a traveling wave. Some spin waves, also called thermal spin waves or thermal magnons, are a result of thermal fluctuations in the sample producing the slight change in magnetization for a spin wave. Another classification of spin waves are driven spin waves or driven magnons, which are an excitation from an antenna.

Whether a magnon is thermal or driven, there are three main geometries that produce distinct spin waves for a magnetic thin film. For the sake of simplicity, the geometries are described for

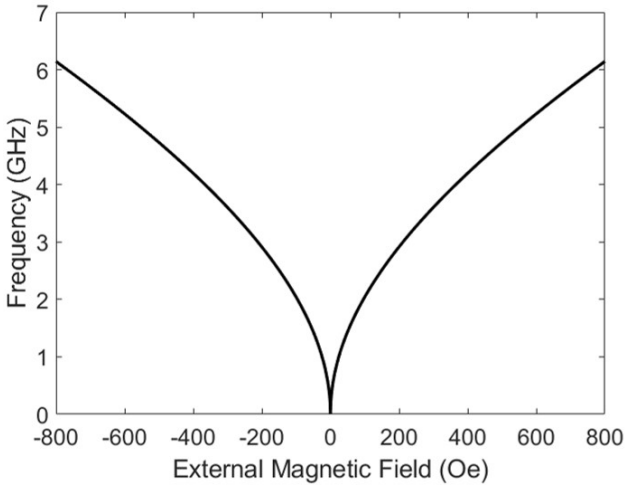

Figure 2.2: The FMR frequency is shown for a thin film of nickel that is magnetized in the plane of the film, using Equation (2.8) where $\gamma/2\pi$ = 2.8 MHz/Oe, $\omega/2\pi = f$, and $4\pi M_s$ = 5125 Oe.

a thin film sample with a thickness of much less than the wavelength of the spin wave. Further details of spin waves and magnetization dynamics can be found in [23]. The first geometry creates a spin wave known as a forward volume spin wave (FVSW), where the external magnetic field $\overrightarrow{H}$ is perpendicular to the plane of the film and perpendicular to the wavevector $\overrightarrow{k}$, or the direction that the wave propagates. The second geometry is when the external field is in the plane of the film and parallel to the wavevector, called a backward volume spin wave (BVSW). Both the forward and backward volume spin wave modes span the thickness of the film, which is why they are volume modes; they interact with the volume of the film. The third geometry is a surface spin wave that propagates across the top and bottom surface (with opposite propagation directions) and the signal decays exponentially as it moves into the film from the surface. The geometry is commonly known by the name Damon-Eshbach (DE) mode, where $\overrightarrow{H}$ is in the plane of the film but perpendicular to the wavevector. The spin wave frequencies for each of these three geometries can be approximated for thin films with waves propagating in the plane of the film, by

$$f_{\text{FVSW}} = \frac{\gamma}{2\pi}\sqrt{H\left(H + 4\pi M_s\left(1 - \frac{1 - e^{-k_\parallel t}}{k_\parallel t}\right)\right)}, \tag{2.9}$$

for the forward volume mode,

$$f_{\text{BVSW}} = \frac{\gamma}{2\pi}\sqrt{H\left(H + 4\pi M_s \frac{1 - e^{-k_\parallel t}}{k_\parallel t}\right)}, \tag{2.10}$$

for the backward volume mode, and

$$f_{\text{DE}} = \frac{\gamma}{2\pi}\sqrt{H(H + 4\pi M_s) + (2\pi M_s)^2(1 - e^{-2k_\parallel t})}, \tag{2.11}$$

for the Damon-Eshbach sample geometry [24]. As previously defined, f is the wave's frequency, H is the external magnetic field, $4\pi M_s$ is the saturation magnetization, γ is the gyromagnetic ratio, t is the thickness of the magnetic film, and $k_\parallel$ is the wavevector parallel to the sample surface. A more complete dispersion curve formulation can be found in [25]. These equations are also plotted in Figure 2.3 as a representation of the dispersion curves for a single thin film sample with parameters appropriate for yttrium iron garnet, a material frequently used for proof-of-concept spin wave studies.

In addition to the three previously described spin wave geometries, for thin films where the thickness is on the order of the wavelength or $k_\parallel t \gg 1$ there can also be perpendicular standing spin waves (PSSW). These are quantized waves across the thickness that look like modes on a string. The dispersion curves can be approximated by Equation (2.12) where the $k_\perp$ is the wavevector component that is perpendicular to the surface of the film, A is the exchange parameter, and the other symbols are the same as the previous three spin wave dispersion equations.

$$f_{\text{PSSW}} = \frac{\gamma}{2\pi}\sqrt{\left(H + \frac{2A}{M_s}k_\perp^2 + \frac{2A}{M_s}k_\parallel^2\right)\left(H + 4\pi M_s + \frac{2A}{M_s}k_\perp^2 + \frac{2A}{M_s}k_\parallel^2\right)} \tag{2.12}$$

Spin waves are investigated in Chapters 6 for confined structures, and other spin wave measurements are discussed in 7. The BLS measurements in these two chapters include both thermal and driven measurements.

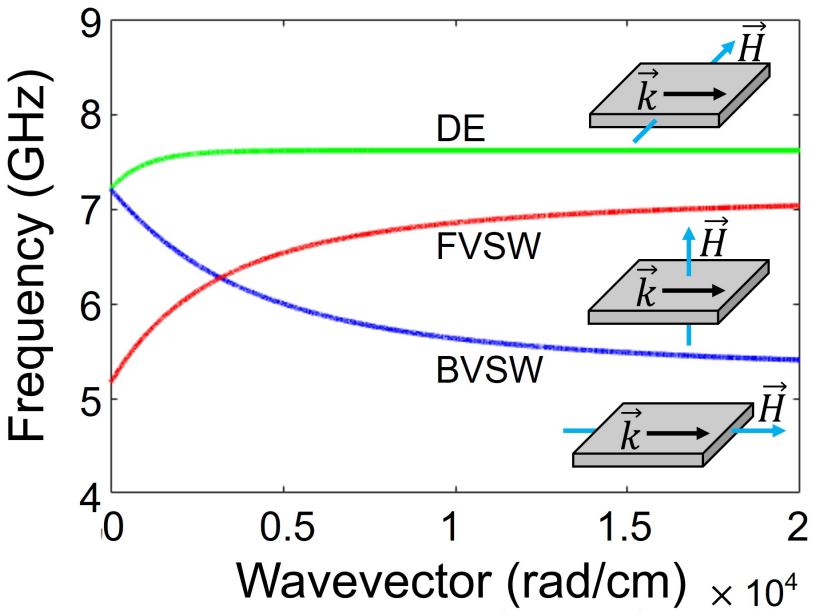

Figure 2.3: This shows the three geometries of spin waves and their representative dispersion curves for a film of yttrium iron garnet with a thickness of $t = 5\,\mu$m, $\gamma/2\pi = 2.8$ MHz/Oe, $H = 1845$ Oe, and $4\pi M_s = 1750$ Oe [24].

2.3 Magnetoelastic Waves

Spin waves and the vibrational waves discussed earlier can also couple together to form what is known as a magnetoelastic wave. These waves have both a magnetic and a physical vibrational wave component, where the waves are coherent and can not be separated from each other. Magnetoelastic waves need conditions where spin wave propagation is favorable along the same direction as the vibrational wave, otherwise the magnetic contribution will be negligible and the wave will just be treated as a phonon. A more extensive review of measurements exploring this coupling has been assembled by Yang [26], which looks at different materials, excitation methods, measurement methods, and resonance conditions. The coupling of these waves brings up the concept of magnetostriction, which will be briefly described here but more details can be found in the magnetostriction chapter of [27].

Some current applications of magnetostrictive materials include magnetic actuators and sensors [28], acoustic wave detection [29], shape memory alloys [30], and magnetic switches [31–34]. While many materials may be considered magnetostrictive, two of the materials with the largest

magnetostrictive values are from the Naval Ordinance Lab called Terfenol-D and Galfenol, which are a terbium-iron-dysprosium alloy and gallium-iron alloy respectively [29, 35]. These materials are commonly included in reviews of magnetostriction material properties, though they also have higher damping and saturation magnetization, so choosing a material for a particular application requires consideration of more than just the magnetostriction values [28–30, 35, 36].

A material is considered magnetostrictive when a magnetic field is applied and the material becomes strained or physically deformed because of the field. This was first reported by Joule in 1842 [37, 38], sometimes called the Joule effect, for the linear expansion of an iron bar. In 1864, the inverse was reported by Villari [39], where a (magnetic) material is strained causing a change of the material's magnetization, known as the Villari effect. Two similar effects, the Wiedemann effect and its inverse the Matteuci effect, that look at the relationship between a material twisting and applied magnetic field, are commonly included in magnetostriction calculations, but will not be discussed here.

Where we previously explored the stress-strain relationship of Hooke's law mediated by elastic constants, here we have a similar magnetism-strain relationship mediated by magnetostrictive values, though it is more complicated since now the crystal structure, crystal anisotropy, shape anisotropy, sample volume, elastic constants, saturation magnetization, external field, and temperature must all must be taken into account.

The magnetoelastic waves explored in Chapter 4 are a result the coupling between a surface acoustic wave and the spin waves in a nickel film. These waves are excited by the magnetostriction of the nickel film when subjected to the strain of the SAW, and studied using Brillouin light scattering measurement techniques.

Chapter 3

Measurement Techniques/Methods

3.1 Brillouin Light Scattering

Brillouin light scattering is an optical measurement technique that involves inelastic light scattered off of a wave in the sample. The inelastically scattered light undergoes a frequency shift that is measured using an interferometer. The measured frequency shift can then be used to find wave properties like the speed, and the intensity of the scattered light can also be used in a driven experiment to map out the propagation of a wave.

The scattering process is named after Léon Brillouin who published his theory (in French) in 1922 [40], though the theory was independently established by Leonid Mandelstam who published in 1926 (in Russian) [41]. A few years later in 1930, the proposed theories were experimentally corroborated by a Russian scientist, Evgenii Gross, using a mercury lamp to look at liquid samples of aniline, toluene, benzene, water, ethyl alcohol, and ethyl ether [42–44]. Before these scattering experiments could become more popular and widely used, two things needed to happen. First was the development of the laser by Theodore Maiman in 1960 [45], which then became a more popular tool for light scattering experiments. Second, the interferometry needed a much higher signal to noise. Although interferometry had been around for decades before Brillouin and Mandelstam developed their scattering theories (Albert Michelson and Edward Morley used interferometry to perform their famous ether experiment in 1887 [46]), the tandem multi-pass interferometer that is used for most BLS experiments today was not developed by John Sandercock until 1970 [47]. Sandercock's interferometer combined previously developed designs that were either multi-pass or tandem Fabry-Pérot interferometers, which, with the addition of a scanning stage and active vibration isolation, has become one of the best and most widely used interferometers in the world for Brillouin light scatting measurements [48–52].

Brillouin light scattering (BLS) is a highly versatile and non-invasive measurement that is used to determine the frequency of dynamics like phonons or spin waves in a sample. It is used in geology for the characterization of the materials that make up Earth's crust [53], in biology to study spider silk [54], and in bio-medical fields to study pig heart cells, mouse corneas, and cancer cells [55–57]. One focus of our lab is the field of magnetics where we study magnetic microstrips [58] and other confined magnetic structures [59, 60], magnon splitting [61], and material characterization for hard drives [62] to name a few past projects. BLS can be used in so many different fields since it can be used to measure samples that are transparent [3, 63, 64], opaque [3, 65], metals [65–67], insulators [68, 69], semiconductors [70, 71], polymers [72], thin films [69, 73], patterned samples [74–76], liquids [42, 56], and nano-particles [72]. By utilizing different geometries and capabilities described later, combined with further knowledge of how elastic or magnetic waves propagate, we can use BLS to study wave speeds [3], extract elastic constants [3, 47, 70, 77], measure two dimensional mode maps [74, 78], map magnetic dispersion curves [79], obtain quantitative measurements of the Dzyaloshinskii-Moriya interaction values [79–81], extract magnetic exchange values [62], determine decay lengths [82], and study non-linear processes [61, 78, 83]. A more complete overview of Brillouin light scattering and its applications can be found in a number of review articles [3, 72, 77, 84–86].

While BLS is one of the most versatile techniques for measuring magnetization dynamics, there are other experimental methods that probe similar magnetic phenomena. Another optical measurement method for magnetization dynamics is called magneto-optical Kerr effect (MOKE), which uses the rotation in polarization reflected off a sample (Kerr effect) to study the orientation of the local magnetization. This polarization rotation is proportional to the magnetization of the sample and can be used to map magnetic domains and spin waves, but is restricted to magnetic materials, whereas BLS is also sensitive to dielectric changes in nonmagnetic samples. Neutron scattering is another method to look at magnetization dynamics, along with photoemission electron microscopy (PEEM) and X-ray magnetic circular dichroism (XMCD); however, these require a particle accelerator or synchrotron as a source for the neutrons or X-rays respectively, whereas

BLS is a tabletop experiment that can be done in a university lab. Ferromagnetic resonance can be measured using either a cavity or a vector network analyzer (discussed in Sections (3.3) and (3.2), respectively), but these FMR measurements look at the magnetization of the entire sample, whereas BLS can look at localized positions across the sample with a resolution based on the laser spot size. BLS is most similar to a measurement technique called Raman scattering, however, BLS is in the gigahertz range, and Raman scattering covers higher frequencies in the terahertz range, which corresponds to molecular vibrations and rotations of chemical bonds.

3.1.1 Sample Interaction

Our BLS measurements use a single mode green, 532 nm (5.64×10^{14} Hz), laser with a narrow linewidth of less than 0.01 ppm. Some of the laser light will inelastically scatter from the sample, conserving energy and momentum (in the plane of the film), and the inelastically scattered light undergo a frequency shift on the order of 1 GHz to 100 GHz, which is much smaller than the frequency of the laser but much larger than the laser linewidth noted above. Much of the incident light will scatter elastically from the sample. Elastically scattered light does not change frequency and is not the focus of BLS measurements. Light can be described as either a particle or a wave and the inelastic scattering process can be similarly described in either framework.

In a particle description the laser light particles (photons) interact with the sample and scatter from quasiparticles like phonons or magnons. Due to the energy and momentum conservation, an incident photon will lose (or gain) energy as a quasiparticle in the sample is created (or annihilated). During an inelastic scattering event that creates a quasiparticle in the sample, the photon will lose the energy, seen as a shift to lower frequency. Conversely, an inelastic scattering event that annihilates a quasiparticle will increase the photon's energy and therefore its frequency. The frequency shift of the inelastically scattered photons with lower frequency, known as the Stokes process, will appear as a negative frequency relative to the initial laser frequency and the higher frequency photons, known as the anti-Stokes process, will appear as a positive frequency relative to the initial laser frequency, which can be seen later in Figure 3.6. The Stokes and anti-Stokes scat-

tering processes are shown in Figure 3.1 where ω is the frequency of the photon or quasiparticle, q is the photon wavevector, and k is the quasiparticle wavevector in the material. The subscripts denote incident light (i), scattered light (s), and material quasiparticle (m) (i.e., phonon, magnon, or another quasiparticle).

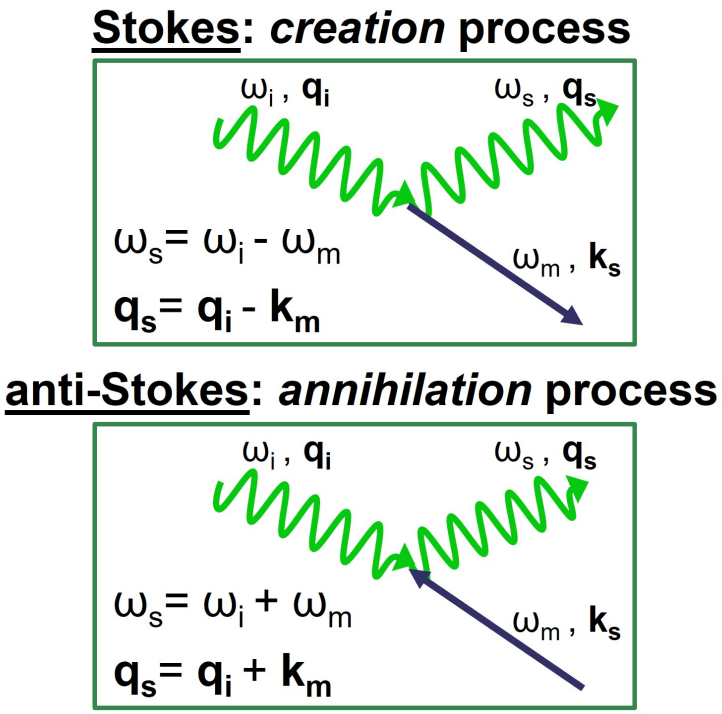

Figure 3.1: The wave creation and annihilation processes for a photon interaction with a generic quasiparticle.

The alternate way to describe inelastic scattering is where light is an electromagnetic wave that interacts with vibrational waves or spin waves through elasto-optical and magneto-optical coupling, respectively [73, 84, 87]. The coupling is also described as a periodic fluctuation of the dielectric constant through which then looks similar to a moving diffraction grating. When the electric field of the light wave interacts with the moving diffraction grating, the scattered light will be Doppler shifted. The previously discussed shift of the photon to lower frequency corresponds to a red shift in the laser light, while a photon shift to higher frequency results in a blue shift of the light.

As noted in Figure 3.1 the energy conservation is discussed in terms of frequency and the momentum conservation is discussed in terms of the wavevector. The wavevector for the incident laser light is denoted by q_i in Equation (3.1), where λ_{laser} is the laser wavelength.

$$q_i = 2\pi/\lambda_{\text{laser}} \tag{3.1}$$

We can similarly look at the wavevectors (k) for thermal phonons or magnons detected by BLS in a sample that has no external excitation. These thermal waves can be separated into surface waves (Equation (3.2)) and bulk waves (Equation (3.3)) traveling though the entire material, which have different wavevectors. The wavevector of a quasiparticle, probed by light with an incident wavevector q_i, traveling a long a surface or interface is

$$k_{\text{surface}} = k_{\text{interface}} = 2q_i \sin\theta, \tag{3.2}$$

where θ is the angle between the sample normal and the incident laser. For a quasiparticle traveling through the bulk of a material, the wavevector is

$$k_{\text{bulk}} = 2nq_i, \tag{3.3}$$

where n is the material index of refraction. Both Equation (3.2) and Equation (3.2) have a factor of 2 from the conservation of the in-plane momentum for a back scattering configuration where the light is scattered back along the incident beam path. As Equation (3.2) suggests, we can control the wavevector of the surface wave by changing the angle θ, within the scattering plane and with respect to the incident laser. Equation (3.2) is also valid for buried interfaces. Snell's law tells us how the angle of the light changes as it goes from one material into another, by the ratio of the refractive indices. The inverse of that same ratio determines how the wavevector changes when moving along the same path between the materials. This results in a cancellation of the refraction

indices, hence Equation (3.2) applies to a wave traveling along any interface, not just the top surface.

Dispersion relations relate the energy and momentum of a wave and can be used to understand how a wave will propagate in a material. When using BLS measurements to map dispersion relations for a sample, the energy and momentum are commonly written in terms of frequency and wavevector. Fitting data with dispersion curves can lead to the extraction of more information like the phase or group velocity of a wave or the material's exchange constant or decay length. Section 2.2 briefly discussed the spin wave dispersion relation geometries for thin films along with their three approximate equations. While spin wave dispersion relations are quite complex, phonons measured by BLS like those in Chapter 5, have more simple dispersion relations because they are often in the elastic regime where the angular frequency is simply $\omega = ck$. This is more commonly written as

$$c = \frac{\omega}{k}, \tag{3.4}$$

where c is referred to as the phase velocity and describes the motion of a single frequency component (like a crest or single spin motion) of the wave. Measuring the frequency shift of a phonon with the BLS, and carefully adjusting the angle (and therefore surface wavevector) allows one to map out a dispersion curve corresponding to Equation (3.4) and calculate wave speeds c for a given material. A similar relationship relates the derivative of the angular frequency and wavevector

$$c = \frac{\partial \omega}{\partial k}, \tag{3.5}$$

where c is then referred to as the group velocity and describes the motion of the wave envelope. The group and phase velocities have the same signs for forward volume and Damon-Eshbach modes, but have opposite signs for backward volume modes. The opposite propagation directions are where the backward volume name comes from, since the phase of the wavefront appears to move backward as compared to the direction of the energy propagation.

As mentioned previously, BLS can be used to measure both phonons and magnons in a sample mediated by elasto-optical and magneto-optical coupling, respectively, through the dielectric constant. For measuring magnons the sample needs a magnetic material with a relatively high magneto-optical signal to obtain BLS measurements with a high signal to noise ratio.

Additionally to obtain a good BLS signal, there needs to be optical access to the sample. This seems obvious, but often materials that we want to measure may oxidize if left in ambient conditions, so a capping layer is put on the material of interest to prevent oxidation. This capping layer can drastically reduce signal and even prevent BLS measurements in some cases where the laser is unable to penetrate the capping layer. This penetration depth depends on the wavelength of light and the complex index of refraction for the material. While deposition of the capping layer is usually well controlled, keeping the capping layer at one or two nanometers is crucial for opaque capping materials to prevent signal loss, though this thickness limit is relaxed for transparent capping materials.

Linearly polarized light is typically used for BLS, and the polarization of the scattered light provides important information. For magnons, the inelastically scattered light used in BLS measurements will have a rotated polarization. This plus the response to an externally applied magnetic field can be used to confirm that a given signal is due to magnons rather than phonons. Additionally, scattered light from surface longitudinal phonons maintains the same polarization as the incoming light, while scattering from surface shear horizontal mode phonons becomes depolarized [3]. To understand what signal is from thermal phonons vs. thermal magnons, a change in the externally applied magnetic field will cause a change to the magnon frequency, while the phonons will remain at the same frequency independent of the magnetic field.

While BLS measures the shifted frequency of a photon that has interacted with a wave in a sample, this information by itself does not provide much insight in the sample or the material. However, knowing the wavevector, polarization of the incident and scattered light, sample geometry, dispersion relation, or if a material is magnetic or not can lead to a more complete understanding of the type of wave, the wave speed, material constants pertaining to stiffness or damping,

ways to manipulate the wave for potential signal processing applications, or novel applications for a material.

3.1.2 Interferometer

The ability to measure the frequency shifts of the laser light after inelastically scattering from waves in the sample is fundamental to BLS measurements. An interferometer is used to separate frequency shifted laser light from elastically scattered laser light by utilizing interference of the light with itself. A Fabry-Pérot interferometer can obtain a frequency resolution of tens to hundreds of megahertz, determined by the finesse and free spectral range (mirror spacing) of the interferometer. Smaller mirror spacings correspond to a larger free spectral range and therefore a larger frequency resolution, whereas larger mirror spacings have a smaller frequency resolution.

Our interferometer is a 3 + 3 pass tandem Fabry-Pérot interferometer from Table Stable (formerly JRS Scientific Instruments) [88]. A Fabry-Pérot etalon is made of two highly (but not perfectly) reflective mirrors that face each other such that any light with a perfect multiple of half its wavelength that fits between the mirrors will constructively interfere. Any wavelength of light that is not a multiple half wavelength of the mirror spacing will destructively interfere and "cancel out" its own intensity. The wave lengths that destructively interfere will not pass through the mirror cavity, but those that constructively interfere will transmit a small percent of the light through the mirror each time it reflects off of the surface, which adds up to a detectable intensity after the mirror cavity. Having a Tandem Fabry-Pérot interferometer means that there are two of the mirror cavities with slightly different spacings to help reduce the presence of harmonics, depicted in Figure 3.2. Because there are multiple half wavelengths of light that each constructively interferes with itself and transmits through an etalon, there will be a signal from each of the different half wavelengths (harmonics) that transmits. By using a second etalon with a slightly different spacing, a single wavelength (frequency) of light can pass through both etalons, but the harmonics will only be able to pass through one of the etalons with a strong signal and will be blocked by the second etalon. Simply put, this configuration allows only one frequency to cleanly transmit through both

etalons at a time. The 3 + 3 component means that the laser light in the interferometer passes through each Fabry-Pérot etalon three times before reaching the detector.

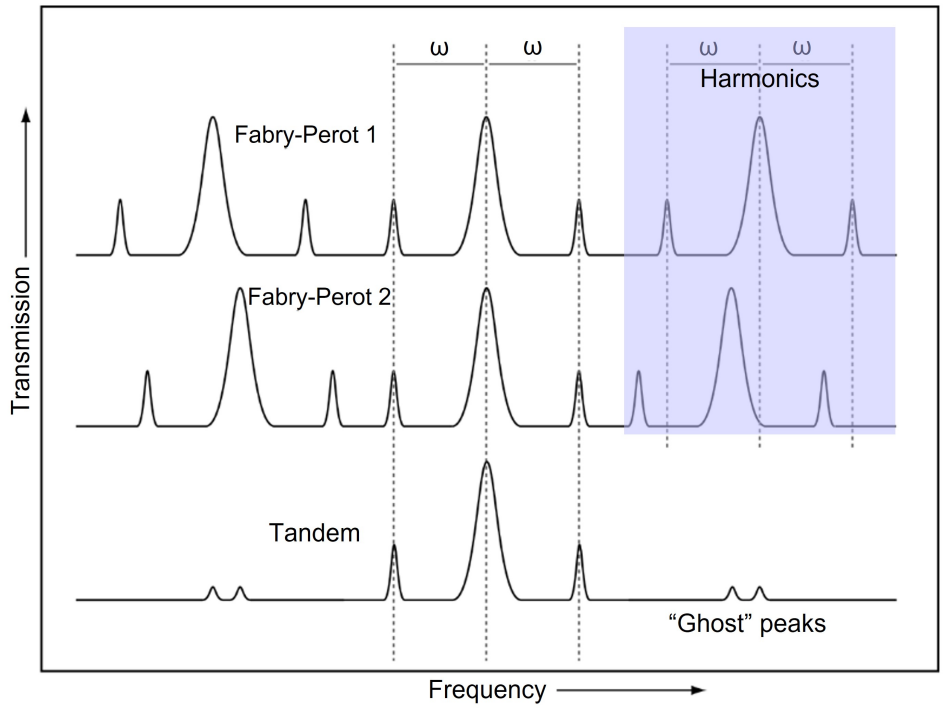

Figure 3.2: Consider a signal beam containing elastically scattered light and inelastically scattered light shifted by frequency ω from the elastic peak. The frequencies that will individually pass through the first and second Fabry-Pérot etalons are shown. The etalons have slightly different spacings so the harmonics will not be at exactly the same frequency. The signal through the etalons used together (Tandem), shows how the harmonics for one etalon are blocked by the other etalon and are transmitted to the detector at a low intensity. The small portion of harmonics that are transmitted through both etalons are called "ghost" peaks. Figure reproduced with permission from Ref. [53].

The setup described above seems like it would only detect one frequency and would require constant realignment for each frequency; however, by setting one mirror of each etalon on a scanning stage we can systematically change the spacings of both etalons and detect a range of frequencies as depicted in Figure 3.3. As previously stated, the frequency resolution of the scan depends on the mirror spacing, a larger mirror spacing will have a better resolution and be able to resolve narrower frequency signals with more accuracy. A typical scanning range is often equal to one or two wavelengths of our laser light ($\pm$ 532 nm or $\pm$ 1064 nm) such that our scan region is bounded

by the harmonics called "ghost" peaks with the elastically scattered light (in practice a reference beam) directly in the middle of our scan region, similar to the Tandem part of Figure 3.2.

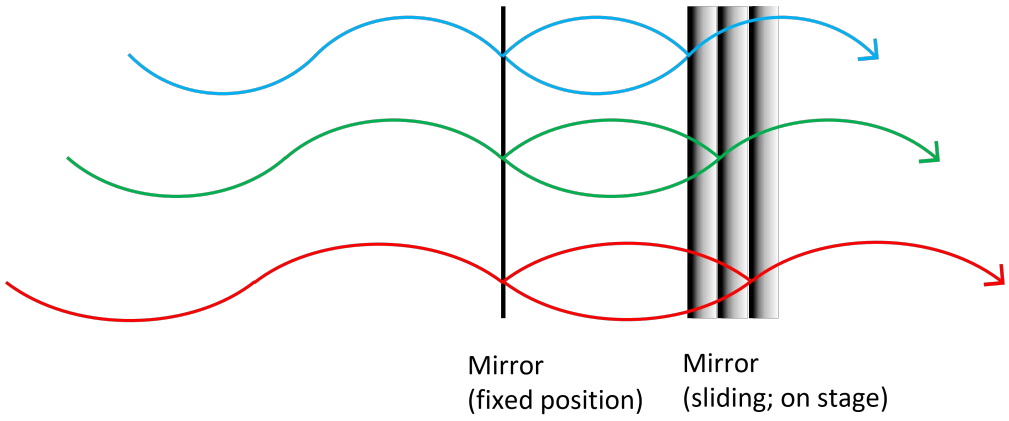

Figure 3.3: Our laser is a green 532 nm laser at the center of the scan region. By scanning one mirror of each etalon we are able to get the blue or red shifted light to fit the mirror spacing in a perfect half wavelength increment, which will constructively interfere in the etalon and transmit through to the detector as the mirror spacing changes with the scanning stage.

The elastic peak is always too intense for the detector, and while the ghost peaks have a lower intensity than the elastically scattered light, depending on the measurement set up, they can also be too intense to safely measure with the detector. To avoid damaging our detector with light at too high an intensity, a double shutter is placed at the front of our interferometer. This allows the inelastically scattered light of the sample beam into the interferometer, but when the stage position aligns with the ghost peaks or the elastically scattered light, the shutter blocks the sample beam and instead lets in a "reference" beam of direct laser light that has been drastically reduced in power so as not to damage the detector. Once out of the elastically scattered light scan region, the shutters switch back to blocking the reference beam and allowing the sample beam through. Additionally, by using a scan range slightly less than the wavelength of the laser, the ghost peaks at the edges of the scan can be excluded.

Figure 3.4 shows the beam path inside the interferometer (a) while taking data (also known as transmission mode/tandem mode), and (b) while in the alignment mode/reflection mode. While

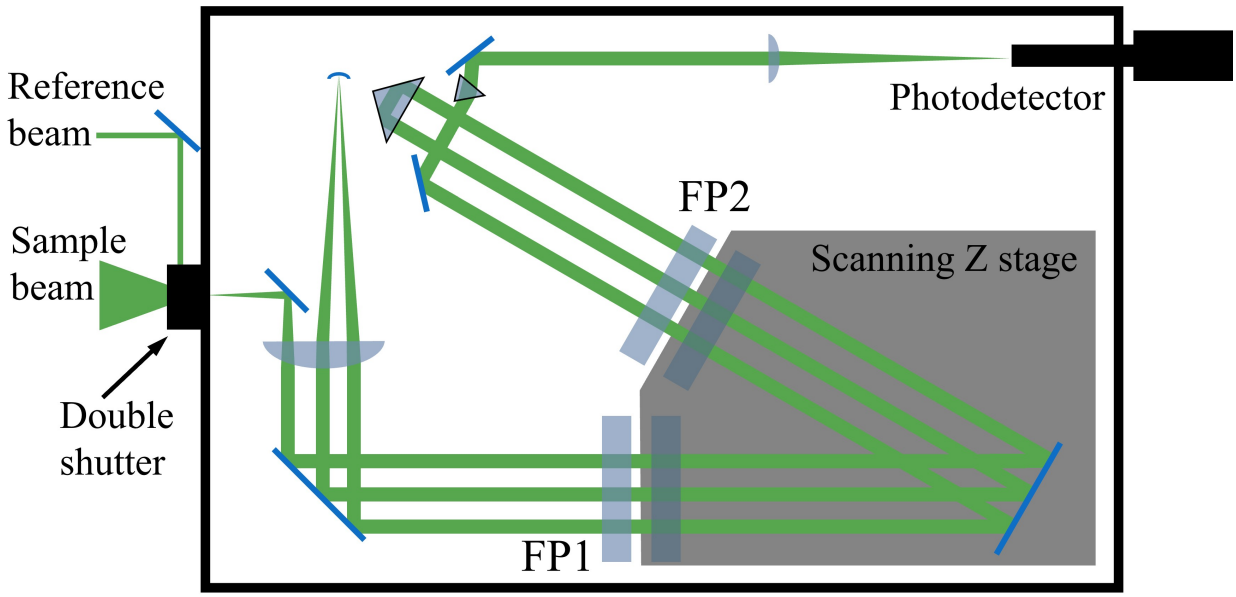

(a) TFP1 Interferometer Showing Transmission Mode Beam Path.

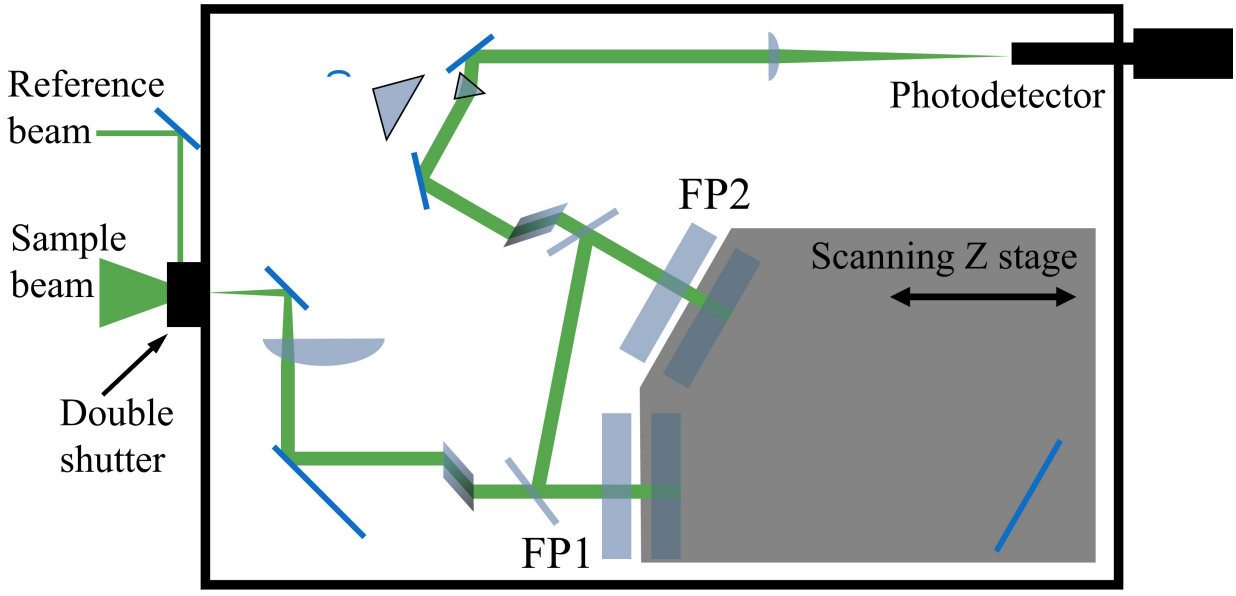

(b) TFP1 Interferometer Showing Reflection Mode Beam Path.

Figure 3.4: The beam paths inside the TFP1 model of the JRS/Table Stable interferometer as seen from above. Using the toggle switch on the side of the interferometer, the beam path can be changed from Tandem/Transmission (a) to Align/Reflection (b) and back. The arrow on the left side points to the black box housing the double shutter. The sample beam (green triangle) enters the double shutter from the front and the reference beam (green line) enters the double shutter through the side.

some alignment needs to be done in the transmission mode to ensure the optimal beam path, the alignment of the mirror pairs (FP1 and FP2) is done in align mode.

Once a mirror spacing is chosen to give an appropriate free spectral range (FSR) where the expected wave frequencies will be visible, the mirrors must be adjusted to be perfectly parallel. If the mirrors are not parallel then a beam that would otherwise be transmitted through the etalon would "walk" its position off the mirror or start to destructively interfere due to the slight spacing differences of each reflection, resulting in a lack of signal. To maintain parallelity between mirrors, there is a coarse adjustment on the side of the interferometer using a mechanical motor to tilt one mirror of each pair to make the inside surface parallel with the inside surface of other mirror in the pair.

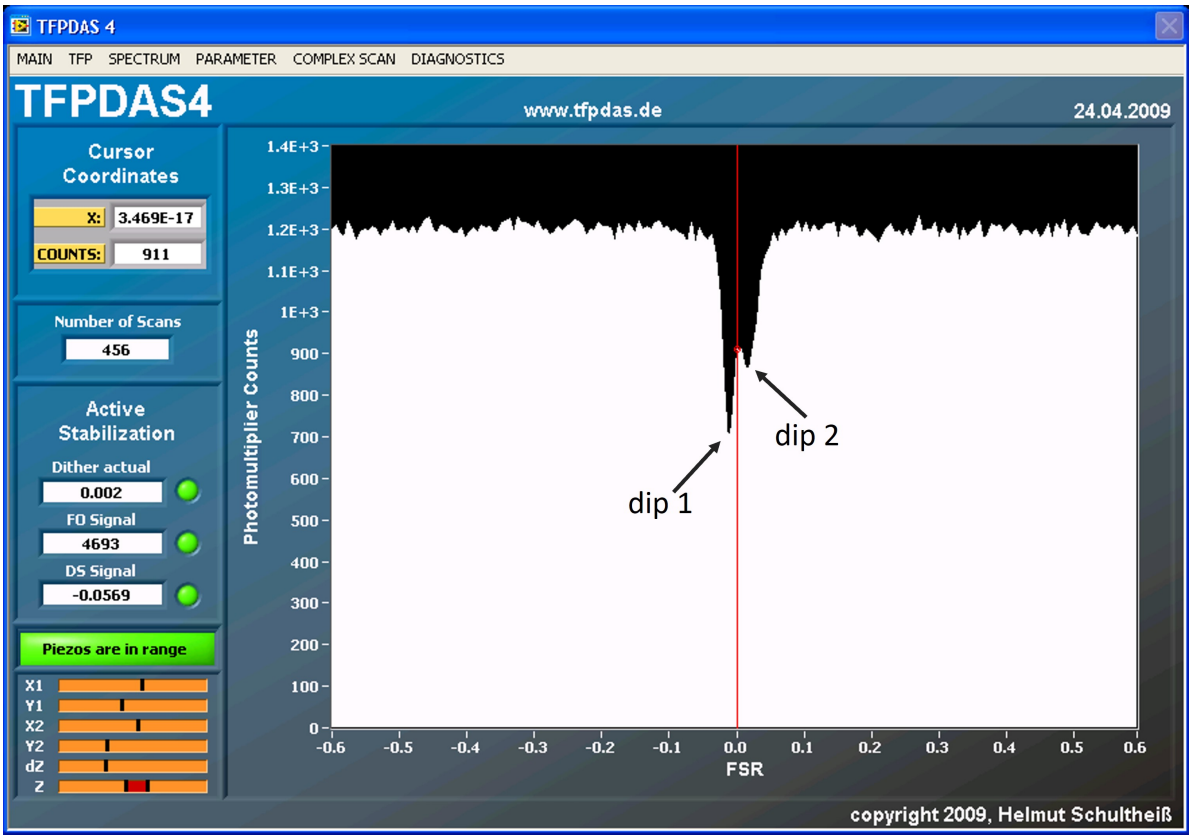

Figure 3.5: A screenshot of the reflection mode view in the TFPDAS4 software showing a typical background level (top of the white section) for the TFP1 showing dips from FP1 and FP2 nearly aligned. The y-axis shows the phonon counts measured at the detector and the x-axis shows $\pm 60\%$ of the free spectral range (FSR) so that the ghost peaks are not included. Reflection mode is the phrase used in the TFPDAS4 software, but it is also known as the align mode.

Figure 3.5 shows the detector signal of the box in align/reflection mode, which corresponds to the beam path shown in Figure 3.4(b). There is a dip in the signal for each mirror pair, one of which is to the left of the red line in Figure 3.5 and the other just to the right of the red line. While the motors can be used to get the mirrors roughly parallel, the fine tuning must be done with a small piezo on top of the motor. The X1 and Y1 peizos are used to tilt one mirror of the first etalon along the corresponding axis. The piezo positions are seen as black markers in orange bars in bottom left of Figure 3.5. To align the mirror, the piezos are adjusted to create the narrowest and deepest dip in Figure 3.5. A narrow, deep dip indicates that only a narrow frequency of light is transmitted through the etalon. The second mirror pair can be similarly adjusted to obtain parallel mirror surfaces. Once the both dips are optimized the two peaks can be brought together with dZ and then centered at zero with the Z adjustment, such that where the dips line up is the only frequency that can transmit through both etalons for that mirror spacing.

After the mirror alignment for the dips in the reflection/align mode, the instrument can be switched to the transmission/tandem mode where the dips become a peak that is transmitted through both mirror pairs. This peak is our reference peak and can now be used for alignment checks of the sample beam. The first sample check is of phonons in a Plexiglas sample, seen in Figure 3.6. The Stokes (negative frequency shift) and the anti-Stokes (positive frequency shift) each show a Plexiglas peak at the same absolute frequency. These peaks allow for real time adjustments to the beam path outside of the interferometer as well as the sample focus to optimize the signal. This Plexiglas signal can reach near the detector upper intensity limit for a great table and interferometer alignment. To get the best alignment though, the interferometer and table optics often require multiple iterative adjustments.

Figure 3.6: TFPDAS4 software window showing a data set from a transparent acrylic plastic like Plexiglas after ∼6 minutes of data collection time. The central white peak (at 0 GHz) is the signal from the reference beam, whereas the white peaks at ± 15.7 GHz are the signal from the acrylic sample. The red dashed lines form the outside edges of two regions of interest (ROI) where the sample data is collected. These red lines denote where the double should should switch between the sample beam and the reference beam or vice versa. The small peaks around -2.5 GHz and +4.5 GHz are bleed-over signal from the elastically scattered light that was not completely blocked by the double shutter. The intensity of the acrylic data peaks can be used to determine quality of interferometer alignment.

After the Plexiglas signal is optimized, the next alignment check is often to measure thermal magnons in iron. It generally takes more time to acquire a thermal magnon signal compared to a phonon signal, and thermal magnon measurements are more sensitive to slight misalignments of the beam path in the interferometer and the other optics on the table. For a typical test scan using the TFP1 interferometer, a laser power of ∼70 mW, an in-plane external magnetic field of 2000 Oe, and a sample angle of $\theta = 45°$ in a back scattering configuration, an iron signal with 1000 photon

counts at its peak and with a background of 700 photon counts will take approximately 10 hours to collect. An iron signal is barely visible above the background after 1 hour of data collection. Once the iron signal is optimized the system is ready for data collection.

While much of the data in this thesis was taken with the TFP1 interferometer from Table Stable (pictured in Figure 3.4), during my time at CSU our lab added a second BLS system with a new TFP2-HC interferometer, also from Table Stable (pictured in Figure 3.7). For the thermal magnon measurement in iron noted above, with the TFP2-HC interferometer it takes $\sim$10 minutes to obtain an iron signal with 1000 photon counts at its peak but only has a background of 10 photon counts. In other words, the new interferometer has 60$\times$ faster data collection times, with a background that is 70$\times$ lower, for the same measurement. After seeing how much faster the TFP2-HC could collect data with a higher signal to noise ratio, the TFP1 was upgraded to a TFP2-HC so both of our interferometers now have the same beam path inside the interferometer.

The beam paths in the TFP2-HC interferometer (Figure 3.7) and in the TFP1 interferometer (Figure 3.4) both include three passes through each mirror set, but in a different order and with slightly different optics. The "HC" in the TFP2-HC interferometer's name stands for high contrast, which is achieved with the introduction of polarization-dependent optics (see Table Stable manual [88] for more details). This also helps to minimize "cross talk" between each of the beam passes through an etalon to further reduce noise in measurements. The TFP2-HC requires that the light of the sample beam entering the interferometer be vertically polarized (or "p" polarized such that the electric field is vertical and in the scattering plane), so depending on what type of wave is being measured, a polarization rotation is required. Any light not vertically polarized upon entering the interferometer will be suppressed long before reaching the detector. Magnons rotate the scattered laser's polarization as compared to the input laser's polarization (light scattered from shear horizontal mode phonons also rotate but the light becomes depolarized so the rotation varies). Magnons were previously measured with the TFP1 by inserting a 90° polarizer between the sample and the interferometer to block any scattered signal with the same polarization as the laser incident on the sample. Now with the TFP2-HC, a half wave plate is inserted before the sample to rotate

the incident laser's polarization such that the scattered light we want to measure will be vertically polarized without any extra optics between the sample and the interferometer where signal can be reduced.

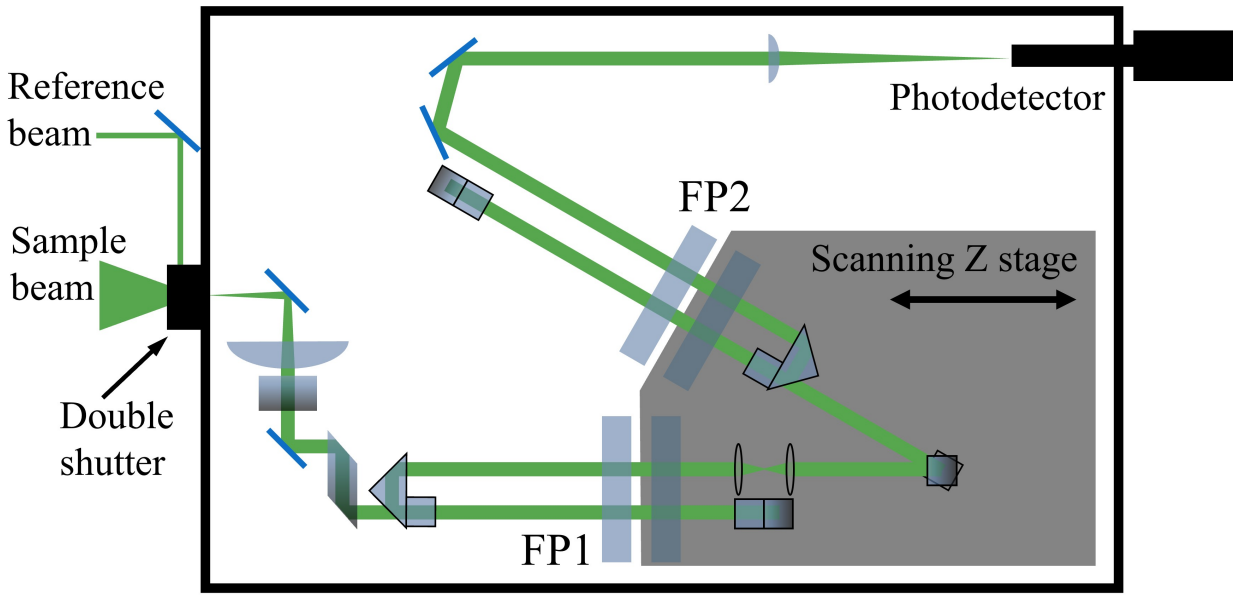

(a) TFP2-HC Interferometer Showing Transmission Mode Beam Path.

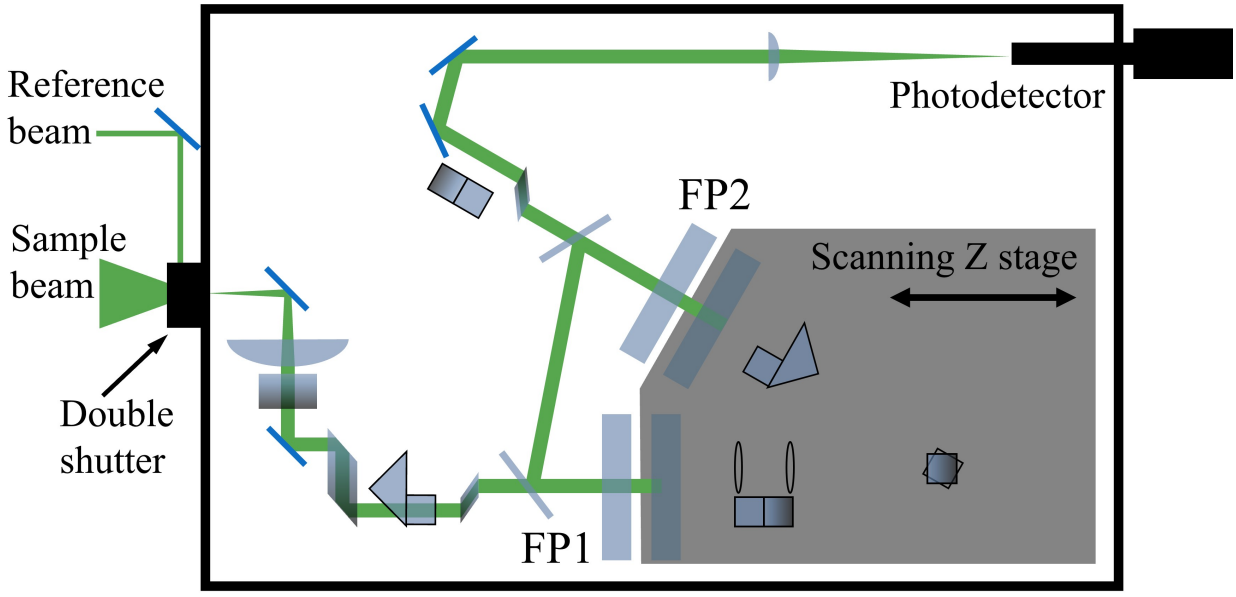

(b) TFP2-HC Interferometer Showing Reflection Mode Beam Path.

Figure 3.7: Similar to the TFP1 model, using the toggle switch on the side of the TFP2-HC model interferometer will change the beam path between Tandem/Transmission (a) to Align/Reflection (b). The order in which the beam passes through the etalons has changed along with the positions at which they pass through the mirrors, but there are still 6 total passes, 3 through each etalon. Polarization optics were also introduced in this version of the interferometer to create the high contrast its name suggests.

3.1.3 BLS Configurations

There are three main configurations of the BLS that are utilized in our lab, two of which are used in this thesis. All three configurations use the green 532 nm laser previously mentioned with a linewidth of less than 0.01 ppm. This laser is a diode-pumped solid state laser with a TEM_{00} or Gaussian mode profile, which is brightest at the center of the beam and then smoothly tapers off at the edges.

The first is a conventional 180° back scattering configuration. Here, the laser light is reflected off the front surface of the sample, back along the same vector as the incident beam, and sent to the interferometer for measurements. For spin wave measurements, the sample sits between two poles of a magnet, such that the external field is in the plane of the sample. The sample can also be rotated about the field direction, such that the field is always in plane, and the reflected laser light that is not 180° back scattered is directed towards the ceiling. As previously discussed, this ability to take measurements at different angles allows us k-vector selectivity. This configuration is most efficient for highly reflective or metallic films. The laser spot size for this configuration is about 30 μm when focused on the sample due the size and focal length of the lens used to collect the back scattered light that is then sent to the interferometer.

The second BLS configuration is the micro-focus BLS or micro-BLS. This is also a back scattering set up, but it uses a 100$\times$ microscope objective with a 4 mm working distance, so that a cone of light is focused on a sample. This cone of light contains many k-vectors, all of which are measured at the same time, which is a bit different from the single k-vector for a single measurement in the conventional 180° back scattering configuration. When focused on the sample, this laser spot size is diffraction limited at roughly 300 nm, allowing for a much more localized measurement than the other configurations. This set up is good for patterned samples with feature sizes of hundreds of micrometers down to single micrometers. While these feature sizes are on the larger end of device components (over 100$\times$ larger than electrical transistors), studying spin waves on this scale is a necessary step before moving to studying spin wave effects in smaller features. To ensure each measurement is on the correct part of the sample, this setup is equipped with a CCD

camera and white light source for sample illumination to view the laser spot location. This setup also has a magnet to apply and in-plane field for forward volume spin wave measurements.

The third and final configuration in our lab is a forward scattering configuration. It is called forward scattering since the laser comes through the back of the sample and exits the front of the sample on its way to the interferometer. This requires that the sample be fairly transparent to 532 nm laser light. Transparent samples in a 180° back scattering configuration would have little back reflected light producing a low BLS signal, but a forward configuration can give a larger signal without the fear of damaging the detector since the elastic light is already blocked by the double shutter. Similar to the conventional 180° back scattering method, the spot size is roughly 30 μm. These two configurations also share a magnet and a beam path after the sample while directing the laser into the interferometer.

The beam paths for these three configurations can be seen in Figure 3.8 as they are laid out on the optical table in our lab.

I also set up a second BLS system for our research group. This uses the new TFP2-HC interferometer, which theoretically should have 4 orders of magnitude higher contrast between the signal and the background noise. In addition to the higher contrast, a new detector with lower dark counts is used to aid in further distinguishing signal from noise. The majority of the samples the lab studies are metal films so this BLS is set up in a 180° back scattering configuration with numerous expansion locations to add other capabilities, like the cryostat currently being installed that will allow for low temperature measurements. This second BLS system has a much smaller, but much more powerful (and more stable) magnet than the one used in our original BLS set up. This new magnet reduces the magnetic field fluctuations by at least 3 orders of magnitude and is bipolar so the field can be swept from positive to negative field (or vice versa) without the need to change electrical connections. The higher signal to noise contrast of the interferometer and the higher stability of the magnet, make thermal spin wave measurements more precise, more reliable, and roughly 60$\times$ faster. The optical table beam paths for this new BLS system can be seen in Figure 3.9.

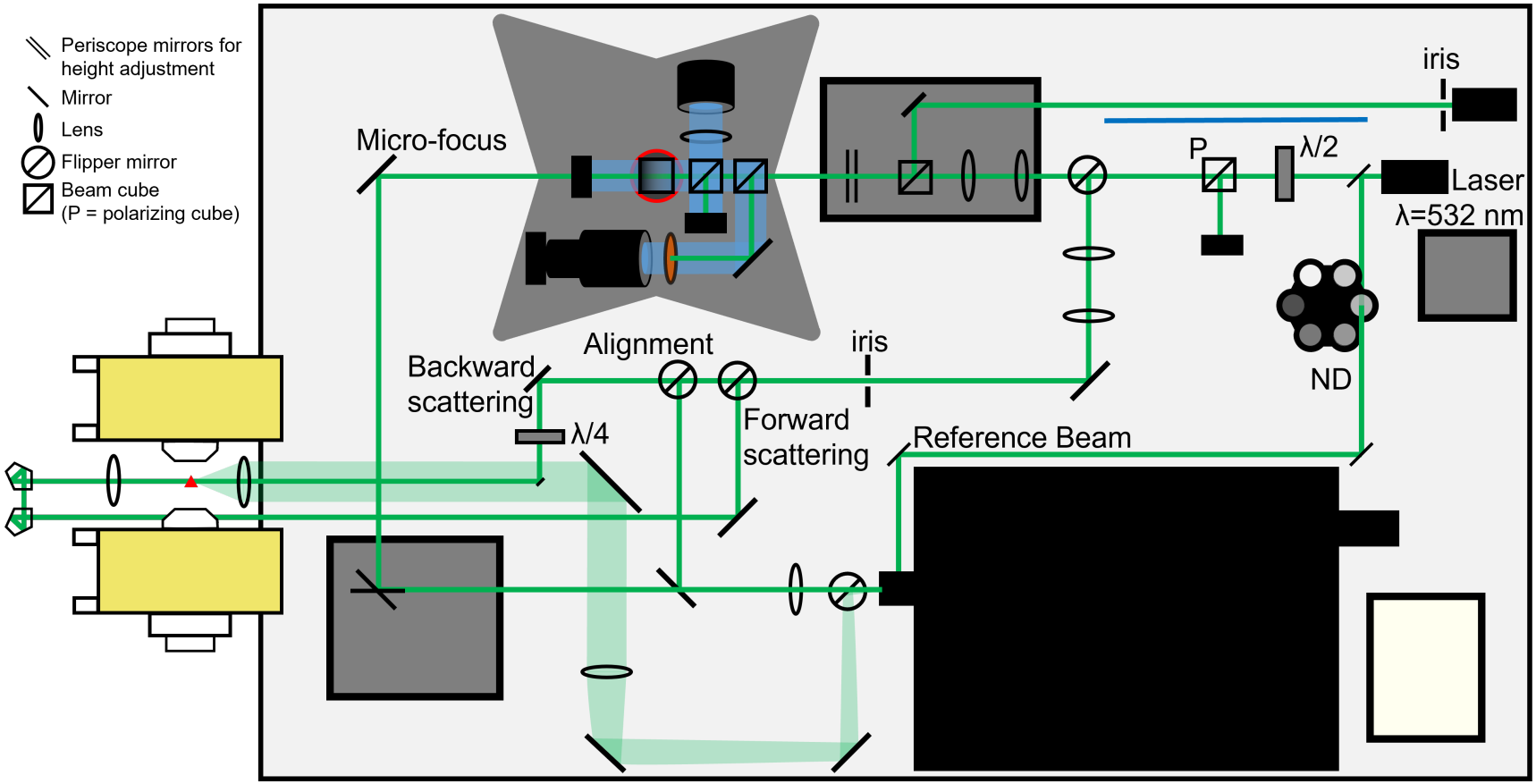

Figure 3.8: This shows the current beam paths with optics (not to scale) on the optical table in labroom D4B, as seen from above. The paths include an alignment beam directly from the laser, a reference beam, a conventional 180° back scattering setup, a forward scattering configuration, as well as the beam path for the micro-focus BLS. The sample for forward and back scattering setups is in the same location between the magnet pole pieces and denoted with a red triangle. The light blue on the Micro-focus setup shows the white light path that illuminates the sample and then reflects back along the beam path before passing through the orange filter to block the laser light and entering the CCD camera. The red circle on the Micro-focus "x-wing" platform is directly above the 100× objective and the sample.

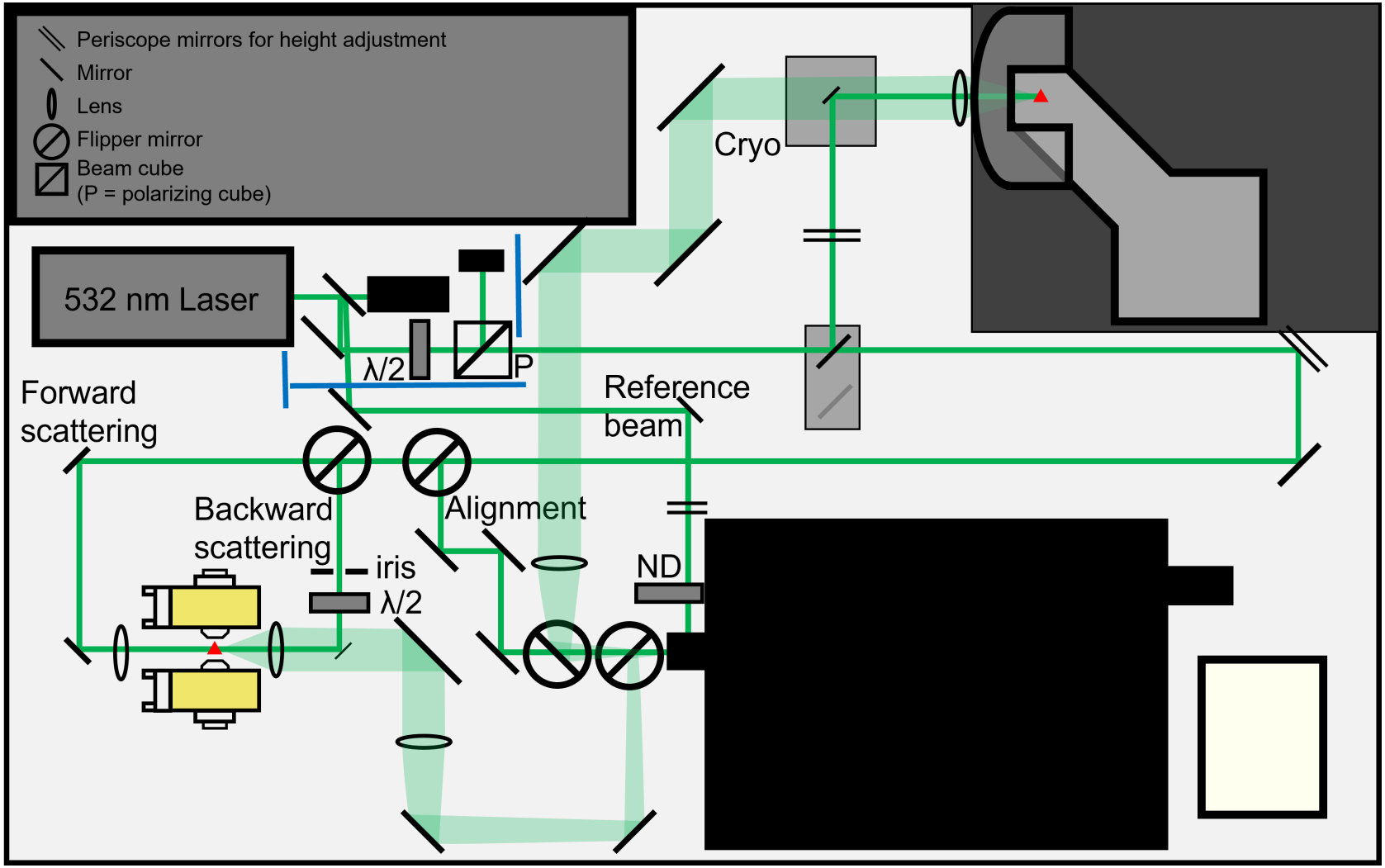

Figure 3.9: This shows the current and proposed beam paths with optics (not to scale) on the optical table in labroom D8, as seen from above. The paths include an alignment beam directly from the laser, a reference beam, and a conventional 180° back scattering configuration. The proposed paths currently include a forward scattering configuration and a beam path for low temperature measurements in a cryostat. Sample locations are denoted with a red triangle.

3.1.4 BLS Software

Once the laser light passes though the interferometer and the detector counts the number of photons of each frequency, this data can be read and displayed in one of two BLS software suites. The first software program is called GHOST written by Table Stable and provided with the interferometer. The second software program is called Tandem Fabry-Pérot Data Acquisition System 4 (or TFPDAS4), written by Helmut Schultheiß with screen shots previously shown in Figures 3.5 and 3.6. Each of these programs will display the photon count vs frequency data from the interferometer, but each has slightly different functionality, described below, that makes one program more favorable for certain measurements.

The GHOST interface for a Plexiglas measurement, shown in Figure 3.10, depicts three purple/pink regions of data. The first is the central peak, the other two are at the edges of the FSR where the ghost peaks or harmonics would be located. All three of these regions are where the double shutter blocks the sample beam and only lets the reference beam into the interferometer. Additionally, Figure 3.10 shows the sample beam signal in green with the two Plexiglas peaks well above the background. For a quick calibration, GHOST needs to be told the scan range as read out on the front of the BLS control box (this is often set at 532 nm or 1064 nm as mentioned previously or is slightly less to move the ghost peaks just out of the detectable range), along with the mirror spacing (using a gauge inside the interferometer that was previously calibrated using conical lenses and laser fringes as described in the interferometer manual [88]). With this information the program will be able to correctly identify the frequency bins as read out by the detector. A more in depth software calibration takes this initial calibration into account and then also uses the frequencies of the ghost peaks on the edges of a scan for a more exact calibration. This program also has an automated acquisition and auto save function performs a measurement, saves the scan, gives the mirror piezos time to adjust and re-optimize the reference beam signal, and then starts another measurement. This feature is helpful for scans that span multiple days and though the sample may heat up a few degrees over this time from the laser, there is generally no damage to the sample with the possible exception of the organic ferrimagnet discussed in Chapter 5. A few other

helpful features included in the software are a statistics function that can give more information on the background and is crucial to knowing the dark counts and the health of the detector, a fit function that will help fit peaks to find the center and width, and two markers that can be moved to identify peak locations while data collection is in progress to confirm the data range is appropriate.

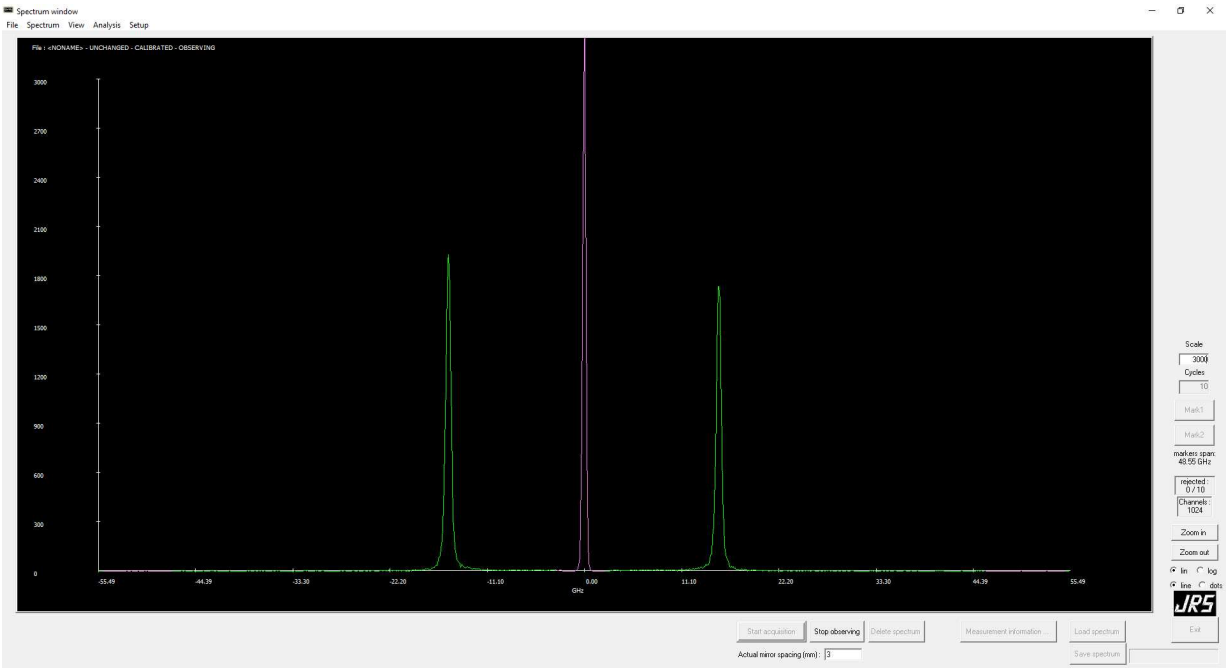

Figure 3.10: A representative image of the GHOST software interface while a measurement of a Plexiglas sample is in progress.The purple/pink central peak is the reference beam, and the two green peaks are the signal from the Plexiglas phonons.

A second piece of software, TFPDAS4, is similar to GHOST but is built using LabVIEW, and gives the user access to part of the stabilization routine through the adjustment of two settings called the FO signal and the dither, shown in the "Active Stabilization" panel of Figure 3.5, to change stability thresholds to try and maintain a "better" alignment. The user must be careful making adjustments to the FO signal and dither because they could force the system to run in an un-optimized state, which will reduce signal quality. This software has one marker to look at approximate frequencies during as scan, but one of the major drawback is the ability to only look at a single FSR. This system overrides the scan amplitude on the interferometer controller and sets it to just below 532 nm so the scan starts and stops without including the ghost peaks. By

forcing all frequencies into the first free spectral range, there can be poor frequency resolution for smaller mirror spacings (larger FSR). The resolution is proportional to the FSR so for some higher frequency signals it can make more sense to halve the size of the FSR but use a scan range covering two FSR. By using two FSR at half the size compared to one FSR, the resolution will be twice as good. However, to measure the second or even third FSR, the GHOST software must be used. For the TFPDAS4 software, the regions where the double shutter blocks the sample beam and lets the reference beam into the interferometer are manually chosen through the ROI table shown in Figure 3.6 and denoted as the vertical dashed red lines set on top of the data. The more powerful aspect of this software is the integration of the TFPDAS4-Micro and TFPDAS4-Time Resolved software.

The TFPDAS4-Micro software interface, seen in Figure 3.11, shows the CCD camera view ($20 \times 22\ \mu\text{m}^2$) of a sample alignment marker with the red crosshairs aligned with the laser location. There is a panel to adjust the camera components like brightness and contrast to obtain the best image possible as well as to move the red crosshairs should the laser or camera be realigned. The other panels control and read out the sample positioning stages along with an option to use a remote. Using a simple USB gaming controller as our remote makes driving around the stages more intuitive and smooth when searching for a specific feature. The final Micro-BLS software panel shown in Figure 3.11 controls the auto focus and focus stabilization. This uses a (secondary) photodetector, different from the interferometer detector, to monitor the laser intensity as a function of the sample stage height. The auto focus routine sweeps the height between the user input start and stop heights. After the sweep the stages will return to the height that produced the maximum intensity. The focus stabilization routine similarly monitors the intensity at the photodetector, but makes continuous height adjustments. A feedback loop then adjusts the sample height to maintain the highest photodetector intensity. This focus can also be visually confirmed through the CCD camera panel if there is any question as to where the focus might be. To fully utilize this software, a CCD camera, light source, secondary detector, and steering optics need to be included on the optical table. These optics can be seen in Figure 3.8 on the “x-wing” platform in

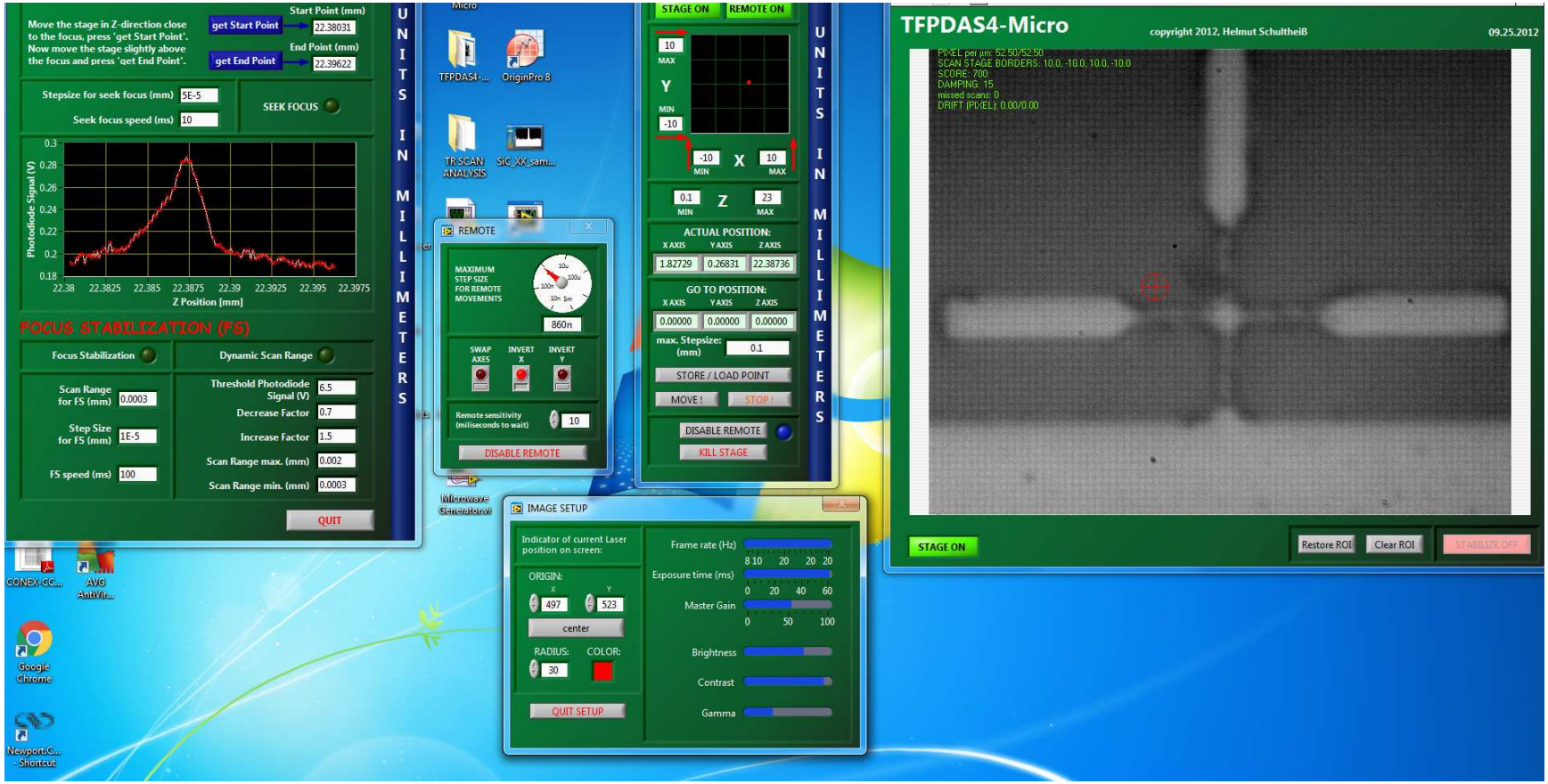

Figure 3.11: Typical TFPDAS4-Micro software interface windows showing a live camera feed with the red crosshairs calibrated to the laser location. There are also windows for image control (brightness and contrast), the sample stage position read out with direct control, and the remote control settings for the stages. The final window shown is the focus stabilization, which shows a plot of the laser intensity from a photodiode as a function of the z-stage position where the maximum intensity corresponds to the in-focus sample position.

the upper left of the optical table and also include an a notch filter to block the green laser light from reaching the CCD camera. The optics added to see the sample through the CCD camera also create a transformation of the sample image as seen in Figure 3.12. For the delay line sample in Chapter 4, the surface acoustic wave is launched from the upper left corner and travels to the lower right corner. However, when viewed through the CCD camera this direction is reversed. Additionally, the external magnetic field points left to right, but seen through the CCD camera the field points bottom to top. Sample symmetries can make this image transformation ambiguous, so the transformation of a capital letter R is included in Figure 3.12 for clarity. Understanding what is seen through the CCD camera and how it is different from looking at the sample by eye is important to ensure that measurements are taken at the correct locations and can also prevent the user from wasting time moving around the sample trying to find the desired feature in the wrong direction and also prevent frustrations when the sample image is different than expected.

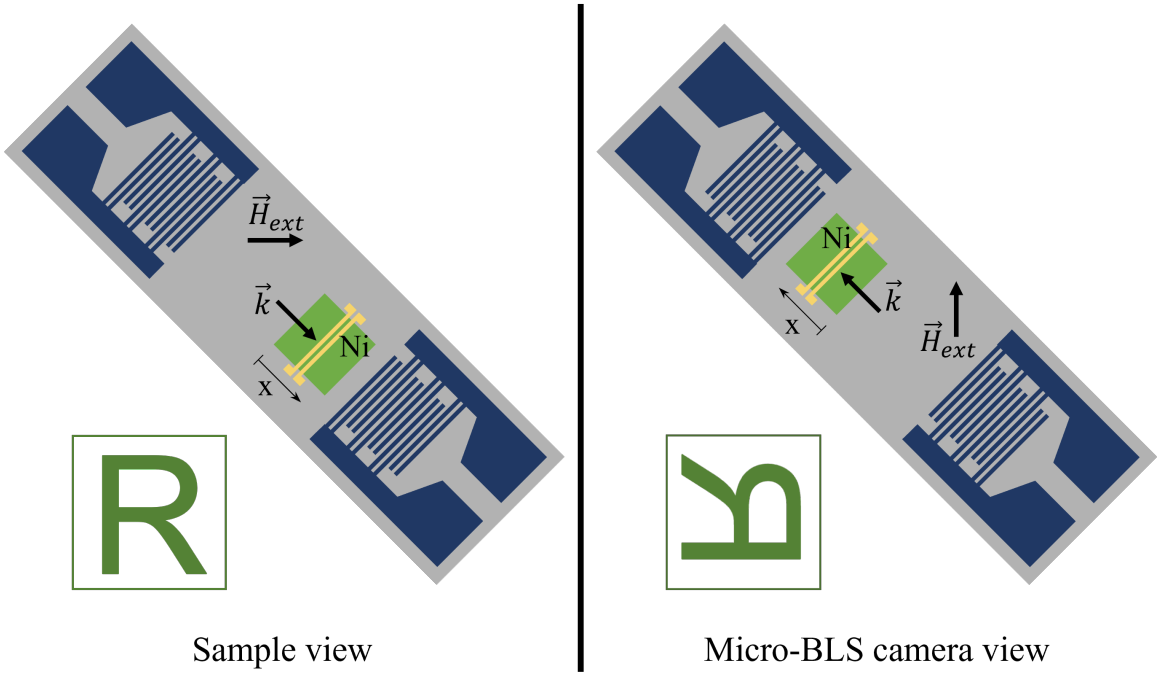

Figure 3.12: The sample view is what the user sees when looking from above, at a sample mounted on the micro-BLS stages. The micro-BLS camera view is what is seen through the CCD camera computer interface. The sample shown is the surface acoustic wave delay line discussed in Chapter 4. The R image is used to remove ambiguity of the transformation due to any sample symmetries.

The TFPDAS4-Time Resolved software uses a trigger sent to both the sample antenna and software to not only measure frequency shifts with the interferometer but keep track of the time between the trigger and when a photon is detected. This "binning" of photons as a function of time after each trigger, creates a time-of-flight measurement, which can help measure wave speed for a known distance between the antenna and the BLS laser location. While much of this is due to the software, a special data acquisition (DAQ) card is needed to achieve a time resolution of 250 ps, but no additional optics are needed.

Once data is collected via GHOST or TFPDAS4, it can be saved as a .dat, or other tab delimited file, which can be imported into any number of software programs for further analysis. The different programs each save out photon counts per bin, where the bin range is labeled with the lowest frequency included in that bin. The informational headers included in the saved files can contain different system parameters like mirror spacing or the time the data were collected.

3.1.5 Other BLS Capabilities

In addition to the different configurations and geometries mentioned, the ability to add a magnetic field is necessary for any spin wave measurements. All of our configurations are equipped with a water cooled magnet, though the magnet stability, field uniformity (based on pole shape and spacing), and maximum sustainable field differ for each of the set ups.

We have the ability to excite antennas with either continuous wave (CW) or pulsed microwave signals, independent of the Time Resolved function. Connections to sample antennas are commonly either a SMA connector directly soldered to the antenna, or a contact probe called a picoprobe. The antenna excitations can lead to faster signal detection or allow us access to k-vectors not otherwise available. These connections can also be used for electrical measurements and characterization described in Section 3.2.

Another capability we have added to our BLS systems is the ability to create a temperature gradient, or to heat or cool our samples $\pm$ 10° C using Peltier heaters. This is currently built into

a sample holder for the conventional forward or 180° back scattering configurations, though a sample holder for the micro-BLS with this capability could easily be fabricated.

One of the more powerful capabilities we can add to any of our three configurations is a 1D or 2D spatial scan. This will take BLS measurements in a line or grid to create a mode map that shows where along that line or grid is more intense to see where the most energy is. This is commonly used for samples with a confined dimension, where a mode profile often shows the wave propagating down a strip. This intensity map helps identify where nodes or anti-nodes are in a given structure to determine which quantized confinement modes are present. The stages used in the micro-BLS configuration have nanometer precision, whereas the actuators for the forward and 180° back scattering configurations have a precision of tens of micrometers, though the limited laser spot size plays a larger role in the spatial resolution of the scan.

The work in this thesis includes angle and polarization dependent measurements using the 180° back scattering configuration and both 2D spatial scans and discrete location measurements using the micro-focus BLS configuration.

3.2 Vector Network Analyzer

A vector network analyzer (VNA), occasionally known as a programmable network analyzer (PNA), is a computer with both a frequency source and receiver that performs electrical measurements by looking at power differences between a source signal and the returned signal after interacting with the antenna and sample [89, 90]. This requires a patterned antenna on the sample or a stripline antenna in contact with the top of a film to transmit the electrical microwave signal from the VNA to the sample. A manual calibration kit or and automatic eCAL module calibrates the system for a specific frequency range and the specific measurement set up. This calibration is cable dependent to better identify a signal that is strictly from the sample and not a cable or connectors. For a single port measurement, the VNA looks at reflection measurement called S_{11} where port 1 is both the signal source and signal receiver. A transmission measurement requires two ports, known as a S_{21} measurement, where port 2 is the receiver and port 1 is the frequency

source. These S-parameters are commonly measured as power loss with units of decibels (dB), which can then be converted to milliwatts (mW) for comparison purposes. Since the VNA has both amplitude and phase information, the S-parameters can be used to study a sample's power absorption from an antenna, a material resonance, or things like complex antenna impedances. The VNA can also find a material's complex dielectric constant, permeability, or permittivity using the S-parameters [91, 92].

For magnetic samples in an external field, the S-parameters can identify the magnetic resonance by the loss in signal power at a specific frequency. The ferromagnetic resonance (FMR) absorption of a thin film can be measured with a VNA using a fixed field and sweeping the frequency as seen in Figure 3.13. If this measurement is taken at many fields, then the M_s value can be calculated using either Equation (2.7) or (2.8) depending on the geometry of the magnetic field.

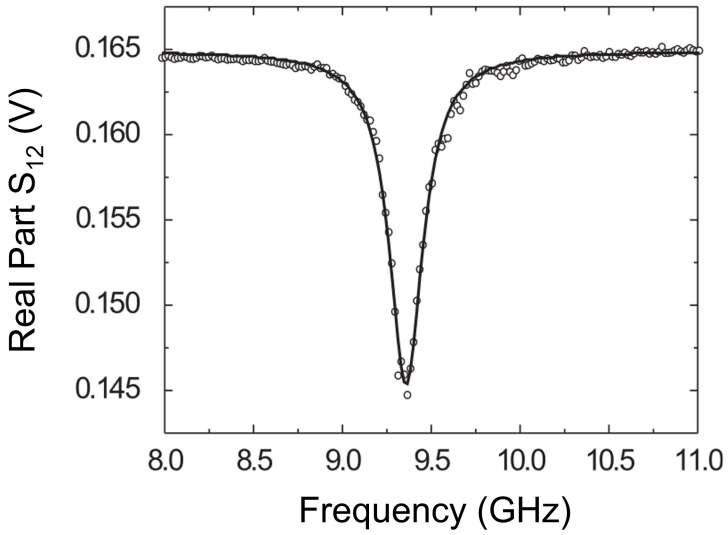

Figure 3.13: This figure shows a typical frequency swept (magnetic field fixed at 210 Oe) ferromagnetic resonance response as measured by a vector network analyzer on a sample of ultrathin (16 molecular layers) thick iron films fabricated with molecular beam epitaxy on a gallium arsenide substrate. Figure reproduced with permission from Ref. [90].

VNA FMR measurements can also be used to determine the full width of the FMR resonance (f_{FWHM}) at half of the maximum, also known as the FMR linewidth ($\Delta f = f_{\text{FWHM}}$) shown in

Equation (3.6) [93]. The FMR linewidth can be used to determine things like the quality factor (Q-factor) of a film ($Q = f/\Delta f$) or the material damping parameter α from

$$\Delta f = |\gamma|\alpha(4\pi M_s) \quad (\text{for } f > 3 \text{ GHz}). \tag{3.6}$$

Here, γ is the gyromagnetic ratio, M_s is the saturation magnetization, and f is the center frequency of the FMR resonance. Equation (3.6) is valid above 3 GHz, but needs an extra term to account for a contribution from inhomogeneous field broadening below 3 GHz.

The VNA-FMR measurement technique is often used in our lab as a quick way to confirm field-frequency combinations for a magnetic resonance to help determine the appropriate BLS mirror spacing and applied magnetic field before attempting BLS measurements. VNA measurements are included in Sections (4.5) and (7.1).

While the S-parameters are fairly straightforward, impedance measurements commonly shown on a complex polar plot called a Smith chart are far less intuitive. The VNA still uses the differences between the source signal and the receiver signal, but it transforms them into the real and imaginary parts of the resistance as a function of frequency. This is used for antenna characterization to study what frequencies transmit well and how much signal loss there will be due to the antenna itself and its wire connections. The Smith chart shown in Figure 3.14 is for the third variation of antenna designed and fabricated for a the project in Section 7.2. The antenna impedance is still not perfectly matched to the VNA frequency source (the real part of the resistance is about 12 Ω too high); however, the imaginary part of the resistance is even across the frequency range we needed. The antenna was able to excite the sample, which could be seen with the S-parameters, but was insufficient to produce a detectable BLS signal.

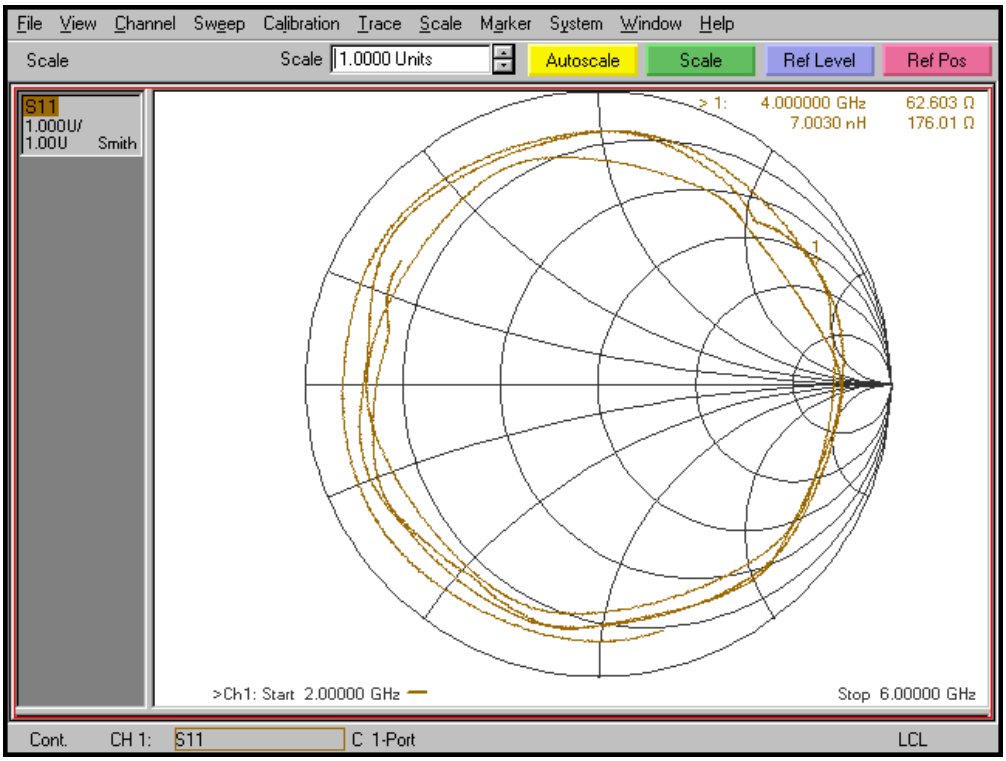

Figure 3.14: This shows the VNA interface of a Smith chart for the third and final iteration of antennas designed and fabricated for a vanadium oxide sample described in Section 7.2. The fairly consistent circle shape is indicative of an even impedance, though the size of the circle indicates that there is an impedance mismatch with the VNA frequency source.

3.3 Cavity Ferromagnetic Resonance

As an alternative to VNA FMR, cavity ferromagnetic resonance uses a cavity instead of strip antenna for mode excitation [89, 90, 94]. This has the more common approach of making measurements by fixing the frequency (what is most efficient for the cavity) and sweeping the field. In this case, the linewidth would be ΔH and further details on the nuanced differences between ΔH and Δf can be found in [93]. While this method of FMR measurement will give similar results as the VNA FMR, the derivative is commonly displayed where the field linewidth ΔH is then the distance between the two peaks.

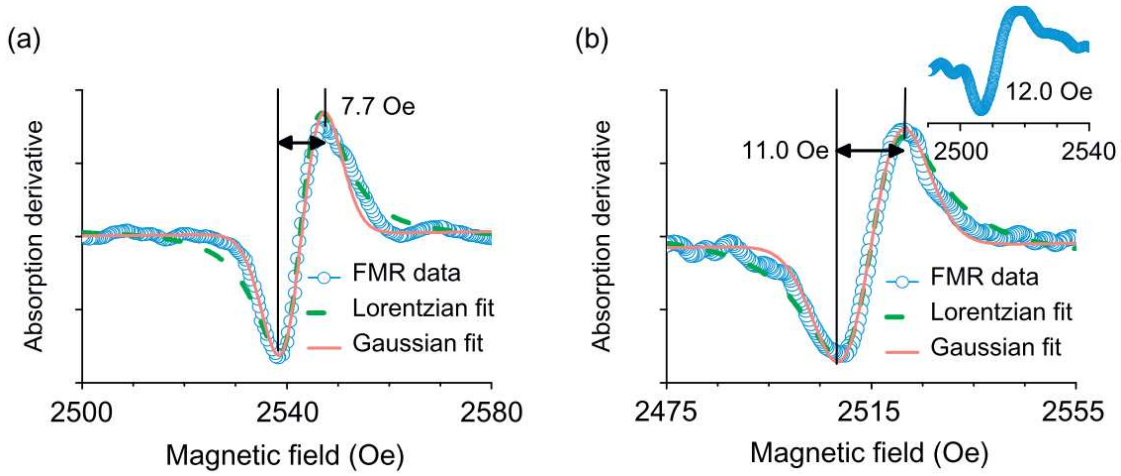

Figure 3.15: A typical field swept (frequency fixed at 9.5 GHz) ferromagnetic resonance response measured by cavity FMR on a sample of 25 nm YIG (a) and 25 nm YIG with a 20 nm capping layer of Pt (b), each with their peak to peak linewidths labeled. The inset to (b) shows the FMR measurement of the YIG/Pt sample excited by an antenna for linewidth comparison. Figure reproduced with permission from Ref. [95].

3.4 Magnetometry

For magnetic samples, it is often helpful to obtain a hysteresis curve (example in Figure 3.16) to measure the saturation magnetization (M_s) as well as the coercive field, to help us choose appropriate magnetic fields applied to a samples in a BLS measurement. Two ways to obtain a hysteresis curve include a vibrating sample magnetometer (VSM) or a superconducting quantum interference device (SQUID) magnetometer [27]. Magnetometry measurements are typically done by sweeping an externally applied magnetic field and measuring the magnetization of sample in response to the external field. A VSM magnetometer vibrates the sample between four pickup coils that measure the magnetic flux as a voltage change as the externally applied magnetic field is swept. A SQUID also measures the flux as a voltage change, but uses a loop with superconducting Josephson junctions, which often produce a higher signal to noise than a VSM. The samples can be at room temperature or cooled for these measurements, though most of our magnetometry measurements are done at room temperature. Additionally, these measurements can be performed on samples with an in-plane magnetization, to aid in surface Damon-Eshbach and backward volume spin wave BLS measurements, or out-of-plane magnetization, for forward volume spin wave BLS measurements.

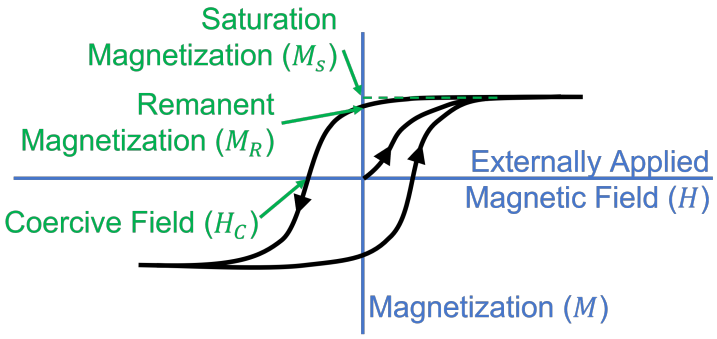

Figure 3.16: A representative hysteresis curve showing the points that determine the saturation magnetization, remanence field, and coercive field.

3.5 Summary

Most of the data presented in this thesis are Brillouin light scattering measurements performed in a back scattering configuration, conventional or micro-focus, to study different types of waves. The main components needed for BLS measurements are the laser, interferometer, sample, and data acquisition software. How the laser interacts with the sample can be described using a quasiparticle scattering framework, a Doppler shifted wave description, or using a sample radiation model, where the latter involves frequency mixing of the electric field of the laser with the dielectric constant modulation due to oscillations from the wave.

To aid us in the collection of BLS measurements, vector network analyzer measurements can help us understand the most efficient excitation frequency of an antenna or sample so we can choose the mirror spacing and scan range to give us the best BLS spectroscopy data. Additional measurements using a magnetometer can help us determine a sample's saturation magnetization, to determine if a sample is still magnetic, and to ensure that the sample is saturated before starting BLS measurements.

Chapter 4

Magnetoelastic Waves Generated by Surface Acoustic Waves

4.1 Context

This chapter summarizes the Brillouin light scattering measurements I took at numerous sample locations and fields, along with the fits and calculations of the decay lengths for a coupled magnetic-surface acoustic wave. This work is a part of a collaboration with the Carman group at University of California at Los Angeles who performed the electrical measurements and the Salahuddin group at the University of California at Berkeley who fabricated the samples. The work described here is part of a manuscript in progress.

4.2 Motivation

Wi-Fi, Bluetooth and other wireless communications are ingrained in modern telecommunication devices, and access to Wi-Fi is commonplace in public places. Wireless communications often use surface acoustic waves (SAWs) as an efficient method to convert wireless electromagnetic signals to wavelengths compatible with the integrated circuits of a device. As devices transition from electronic to "spintronic" and incorporate spin wave signal carriers, it becomes vital to study the spin wave decay lengths. In magnetic metals, spin wave decay lengths are often less than 10 μm, which is far too small to span distances required in a complete device [75, 96]. One way to obtain a larger decay length is to use an insulator with low damping like yttrium iron garnet (YIG) or to couple the spin wave to a surface acoustic wave that has a decay length orders of magnitude larger. Not only can this coupling extend the decay length of the spin waves, but it can also add new functionality of non-reciprocal wave propagation to surface acoustic waves and provide a more efficient way to generate spin waves [97–99]. In essence, the magnetoelastic coupling between the

waves and the magnetostrictive effects of the materials, can allow for SAW control by a magnet, and spin wave control by elastic manipulation.

Previous work measuring acoustically driven ferromagnetic resonance (ADFMR) has included time and spatially resolved photoemission electron microscopy (PEEM) and X-ray magnetic circular dichroism (XMCD) to look at the strain of the (SAW) and the corresponding magnetization. However, these measurements require the use of a synchrotron and are in small patterned ($2 \times 2\ \mu\text{m}^2$) squares [100]. Similar PEEM and XMCD were also done on larger structures but with a copper stripe across the magnetic film [101], where stripes like this are invasive and decrease the signal. Another optical method used to study ADFMR is nitrogen vacancies (NV) in nanodiamonds [102]. Due to the nanodiamond implantation, only specific locations can be measured and the NV signal is sensitive to the magnetization, not the SAW. Electrical measurements are also a common measurement technique for ADFMR studies, and while some electrical measurements performed by our collaborators are included in this thesis, we have found that the striplines are invasive and effect the signal. Additionally, the striplines do not provide localized spatial measurements, but BLS does. We use Brillouin light scattering (BLS) microscopy to study the coupling between spin waves and acoustic waves because measurements can be taken in the lab without the need for a synchrotron and BLS is non-invasive (no diamond implantations or stripline depositions needed). Using BLS we also measure nonlinear signals not achievable with electrical measurements.

This project uses BLS microscopy to look at a magnetic material with high magnetostriction, placed along the path of a surface acoustic wave (SAW) to gain a better understanding of the coupling that gives rise to magnetoelastic waves [102–106]. The high magnetostriction creates a large coupling effect where the physical deformation from the elastic wave, often described as a stress or strain, changes the local magnetization as described in Section 2.3 and shown in Figure 4.1 as it applies to this this project.

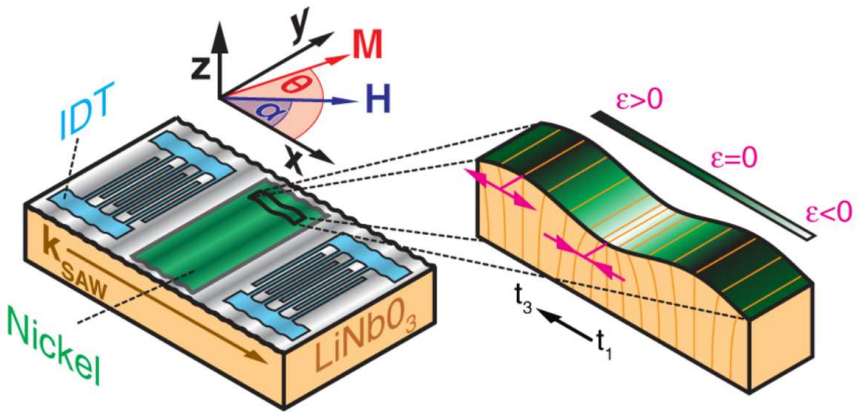

Figure 4.1: Diagram showing magnetostriction in nickel film from a surface acoustic wave. Figure reproduced with permission from Ref. [103].

Figure 4.2 shows a schematic of the energy transfer mechanisms inside the sample for BLS measurements. The energy input to the sample starts with microwaves sent to the antenna on top of a piezoelectric substrate. Much like the inverse magnetostriction in Section 2.3 where a change in magnetization creates a strain, in piezoelectric materials a change in the electric field creates a strain. Due to the antenna structure, discussed later, the periodic strain will oscillate at the microwave frequency creating a surface acoustic wave of the same frequency that then propagates along the top of the substrate. When the SAW reaches a magnetic thin film, the magnetostriction of the film creates a magnetic wave of the same frequency as the SAW, such that the waves are coupled and coherent. This coupled excitation is a magnetoelastic wave. When a laser is focused onto the magnetic thin film, the laser interacts with the magnetoelastic wave as described in Section 3.1.1 where the back scattered light is then sent to the interferometer for frequency detection.

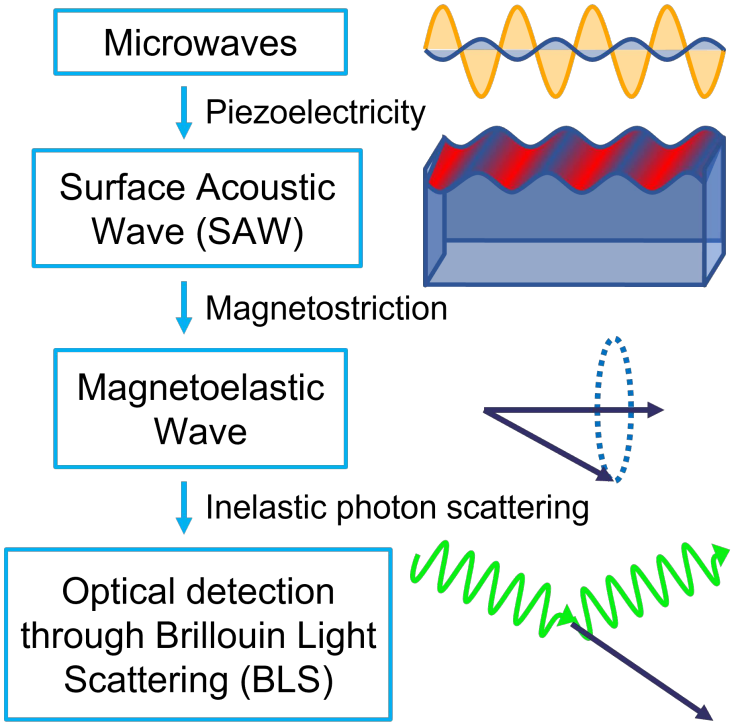

Figure 4.2: Diagram showing the interactions in the sample to produce a SAW, generate a magnetoelastic wave, and obtain a BLS signal from the nickel film.

4.3 Sample Design and Fabrication

Sample design and fabrication, done by collaborators at UC Berkeley and UCLA, starts with the piezoelectric substrate lithium niobate ($LiNbO_3$). A piezoelectric substrate is used to transform an electric microwave input into a stress or strain resulting in a physical deformation and when used in conjunction with an appropriate interdigitated transducer (IDT) design, creates a SAW [103,104, 107, 108]. Using photolithography techniques two aluminum IDTs were deposited roughly 2 mm away from each other to create the SAW delay line. These IDTs had a split or double finger design seen in Figure 4.4 that efficiently excites the third harmonic (Figure 4.6) [105]. The delay line used in this project to create the SAW is already used in commercial devices for wireless communications and for filters, oscillators, and sensors [107, 109]. By adding a magnetic material we take a first step at integrating magnonic devices to current systems and creating "spintronic" devices that utilize both electrical and magnetic signal carriers [35, 110]. The SAW is a physical ripple across the surface of the substrate, so by putting a thin film of a magnetic metal on top, this

material will also feel the ripple. The magnetic metal must have a thickness of less than the SAW wavelength for the ripple to permeate completely through the film. For a thin enough magnetic film, as the SAW passes under a single point, the magnetization changes with the peaks and dips of the SAW creating a (coupled) magnetic spin wave.

Nickel, with its high magnetostriction, was chosen as the magnetic material to maximize the coupling between the SAW and the spin waves in the nickel film [108, 111–113]. The average magnetostriction value of nickel is 30 ppm (parts per million) measured at magnetic saturation. Though Terfenol-D has a magnetostriction value between 30$\times$ and 75$\times$ larger than nickel, nickel has about half the damping allowing spin waves to travel farther in nickel compared with Terfenol-D [29, 35, 36]. Nickel also does not require rare earth elements or any stoichiometry optimization like many alloys with higher magnetostriction. Additionally, nickel is resistant to oxidation, making it an ideal material for our samples.

Our collaborators ran measurements of the intensity of the SAW absorption in the nickel film as a function of the externally applied field, shown in Figure 4.3, since the magnetic field direction is a critical parameter for magnetoelastic waves. The optimal angle of the external field with respect to the SAW propagation direction is predicted to be $\pm 45°$ based on theoretical calculations and simulations [103, 104, 106]. Experimentally, this angle has been seen as low as $\pm 35°$ due to possible mismatches in the substrate crystal cut, magnetic field direction, SAW propagation direction, and shape of the magnetic material, which can alter the coupling efficiency of the magnetoelastic wave [105, 114].

For our experiments, a 25-nm thick nickel film (300 μm^2), was patterned a distance of roughly 1.5 mm from the left (far) IDT as seen in Figure 4.4. The nickel pad was deposited on a 128° YX-cut $LiNbO_3$ substrate via electron beam evaporation and patterned using optical lithography techniques. The SAW is a Rayleigh wave at the surface of the $LiNbO_3$, a physical ripple that permeates the material on the order of the SAW wavelength. To ensure that the 25-nm thick nickel film is sufficiently thin and that the SAW will permeate the full nickel thickness, we can calculate the SAW wavelength for comparison. The SAW speed in $LiNbO_3$ is between 3500 m/s

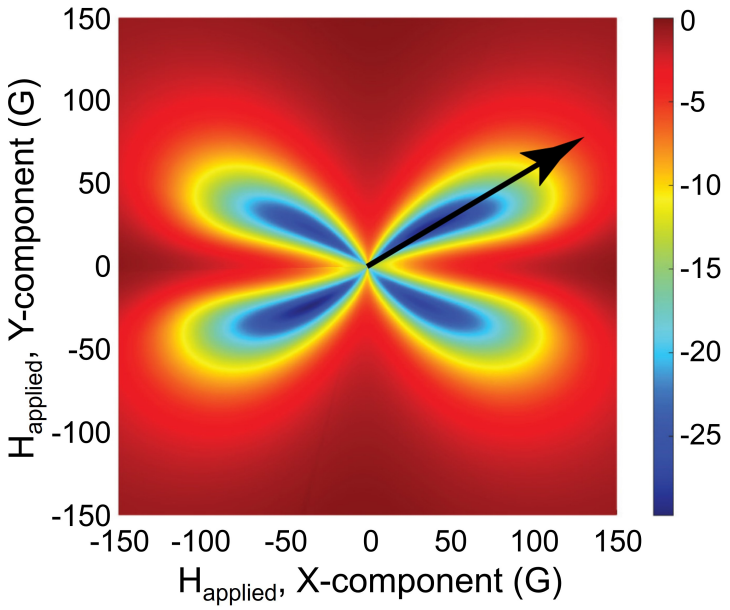

Figure 4.3: This shows an XY map of the intensity of the SAW absorption (in dB) of a 25-nm thick nickel film (500 μm $\times$ 1200 μm) deposited by electron beam evaporation on a Y-cut $LiNbO_3$ and patterned via optical lithography techniques. The SAW is traveling in the $+x$ direction where absorption data was extracted from the S_{21} measurements of a vector network analyzer. This measurement is at 1.992 GHz and shows the highest absorption at $\sim 40°$, which is close to the theoretical angle for maximum absorption of $\sim 45°$. Figure reproduced with permission from Ref. [105].

and 4000 m/s [115], so for a 1.8 GHz SAW frequency, the SAW wavelength will be 1.94 - 2.22 μm. The SAW wavelength is almost two orders of magnitude larger than the 25-nm thick nickel film, making the nickel sufficiently thin to the extent that the strain produced by the SAW is uniform through the thickness of the nickel.

For electrical characterization a shorted gold stripline was placed across the center of the nickel parallel to the SAW wavefront. The gold strip was electrically isolated from the nickel using a 20 nm SiO_2 layer. Titanium adhesion layers were used underneath both the nickel film and the gold stripline. For characterization, samples with two similar delay lines were fabricated: one without both the nickel film and the gold stripline, the other with the gold stripline but without the nickel film. A nickel film was also deposited on a separate $LiNbO_3$ for magnetic hysteresis measurements. The hysteresis loop (not shown) was fairly narrow and rectangular, with a coercivity of 15 Oe, a saturation magnetization ($4\pi M_s$) of 5125 Oe, and with the ability to fully saturate the sample with an externally applied field of 100 Oe.

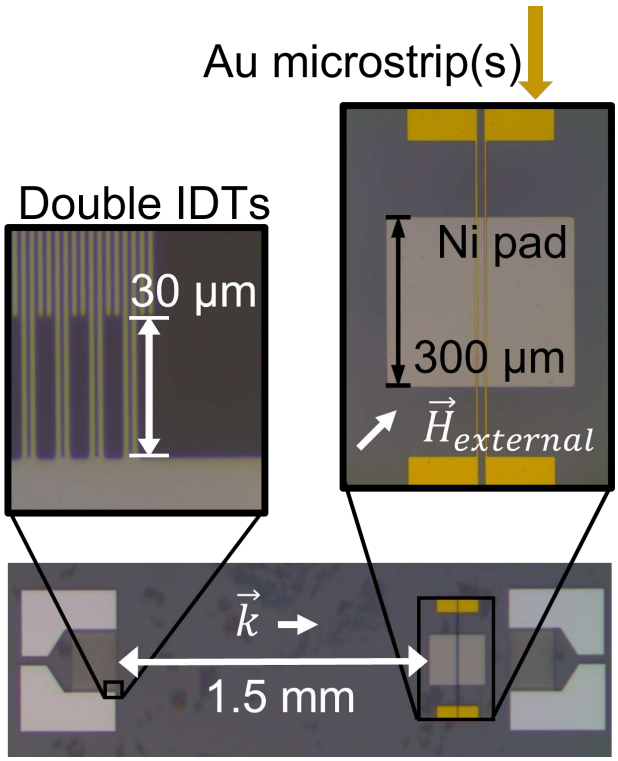

Figure 4.4: Optical microscope images of the SAW delay line showing the split finger design of the IDT and the gold stripline on top of the nickel film.

4.4 Experimental Set Up

Electrical measurements were performed with a network analyzer for both transmission and reflection measurements as described in Section 3.2. The IDTs were characterized with an S_{21} transmission measurement where the frequency swept signal (0.5 GHz to 5.0 GHz) was sent from one IDT (port 1) and received at the other (port 2). The nickel film was characterized with both a field swept transmission measurement and many field swept reflection measurements. The S_{31} transmission measurement at a fixed 1.8 GHz frequency (- 400 Oe to + 400 Oe) sent the signal from the far IDT (port 1) and received the signal at the gold stripline (port 3). The S_{33} reflection measurements used a field sweep of - 800 Oe to + 800 Oe at many frequencies between 0.9 GHz to 8.0 GHz, where the signal was both sent and received by the shorted gold stripline (port 3). The shorted gold stripline consists of two thin strips of gold that are connected at one end using a wire bonder, and the VNA is connected to the ends opposite the short with one strip as the signal and the other strip as the "ground".

I used the micro-focus BLS to measure the SAW on the $LiNbO_3$ just in front of the nickel film as well as and the magnetoelastic wave at different locations across the nickel (shown as red dots in Figure 4.5 starting at the front edge and stopping just before the gold stripline. All SAWs were driven from the left (far) IDT using a CW 1.8 GHz microwave input, while each measurement had a different location and externally applied field ranging from -400 Oe to +400 Oe. The nickel measurement locations are spaced at roughly 30 μm apart over a distance of 130 μm, which allows for study of the signal intensity as a function of distance to determine the decay lengths for the magnetoelastic wave. The different applied fields allow for study of the magnetoelastic wave when the sample is fully or only partially saturated and both on and off of the nickel film's magnetic resonance to help determine coupling efficiency.

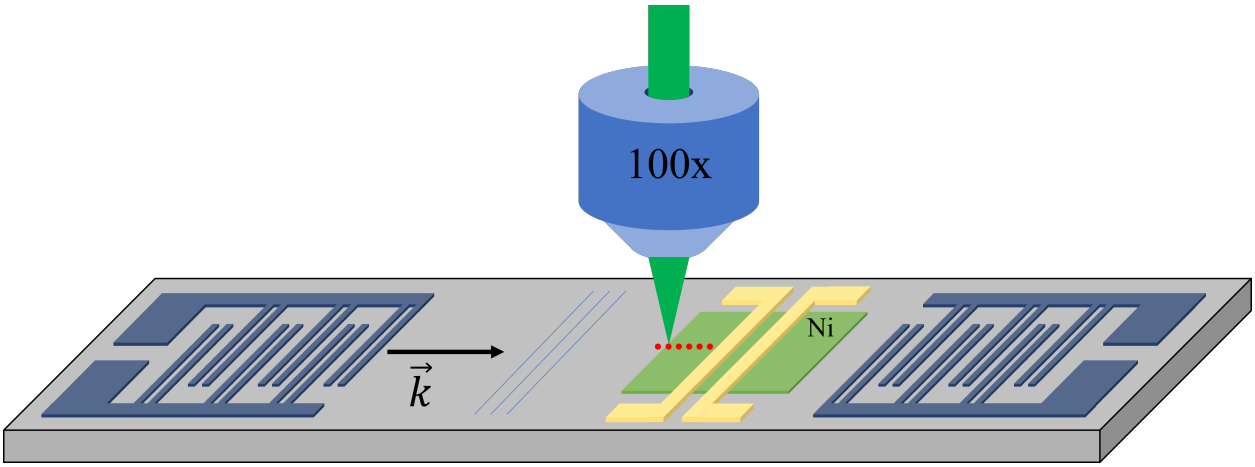

Figure 4.5: A general schematic (not to scale) showing the IDT delay line (navy) with the nickel film (light green) and gold stripline (yellow) on the $LiNbO_3$ substrate (grey). The red dots show the approximate locations where the micro-focus BLS measurements were taken.

4.5 Electrical (VNA) Measurements

Our collaborators performed electrical measurements, made with a vector network analyzer (VNA), to characterize the sample and ensure the device performed as we expected, producing a surface acoustic wave (SAW) that would couple with the nickel film. Electrical measurements to characterize the IDTs were made on a delay line without a nickel film, where the SAW

was launched from the left IDT and received at the right IDT, for a VNA transmission measurement (S_{21}). As shown in Figure 4.6 there is a strong transmission of the fundamental frequency f_0 = 600 MHz as well as the third harmonic of f = 1.8 GHz. This third harmonic is on the lower end of wireless communication (1.7 GHz is a 4G band, 2.45 GHz is for Wi-Fi and Bluetooth) but works as a proof of concept for integrating magnetic signals into commercial products, since the higher frequencies used for 5G, WiFi, and Bluetooth would be achievable with changes to the IDT finger width and spacing between the fingers.

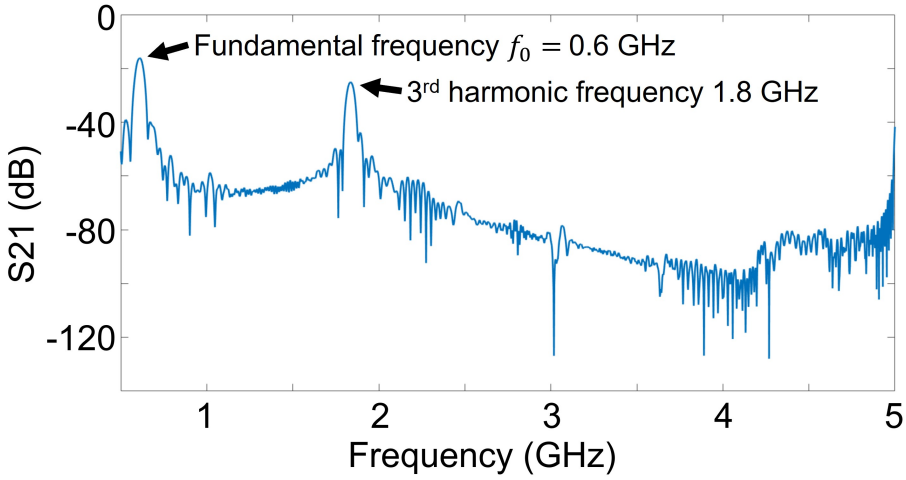

Figure 4.6: A network analyzer measurement showing the transmitted frequencies from one IDT to the other via surface acoustic waves. The strongest transmitted frequencies are the fundamental and the 3rd harmonic at 0.6 GHz and 1.8 GHz respectively.

After understanding the SAW frequencies the delay line can efficiently launch, the next thing to characterize is the nickel film's response to the surface acoustic wave. This was done with a similar set up as the delay line characterization, where the input signal was connected to the left IDT, farthest from the nickel film, which created the SAW. The signal is received by the shorted gold stripline on top of the nickel giving the VNA transmission measurement S_{31} seen in Figure 4.7 to better understand the coupling efficiency between the nickel and SAW . This measurement is done at a fixed frequency of 1.8 GHz to make use of the efficient SAW excitation of the 3rd harmonic, and the field was swept from -400 Oe to +400 Oe. An identical measurement was

performed with the same network analyzer configuration but without a nickel film, where the gold stripline was deposited directly on the $LiNbO_3$ substrate. The data shown in Figure 4.7 was taken at 1.8 GHz, where the VNA measurement of the sample without a nickel film (orange line) has no field dependence, and the VNA measurement of the sample with a nickel film (blue line) does show a field dependence. The two dips in the blue line correspond to the measured magnetic resonance of the nickel film ($\pm$ 60 Oe) at the 1.8 GHz frequency. This is slightly different than the 79 Oe FMR frequency calculated from Equation (2.8) where $\gamma/2\pi$ = 2.8 MHz/Oe, $\omega/2\pi = f$ = 1800 MHz, and $4\pi M_s$ = 5125 Oe. This difference is likely due to the externally applied field or the measurement probe being misaligned, or our sample had a smaller M_s value than what was reported from the SQUID measurements of a similar sample. Additionally, Figure 4.7 shows a small kink at + 15 Oe, which corresponds to the coercivity of the nickel film, as determined by SQUID measurements. This kink shows up where the sample magnetization switches from the initial negative direction to the positive direction as the external applied field is swept from - 400 Oe to + 400 Oe.

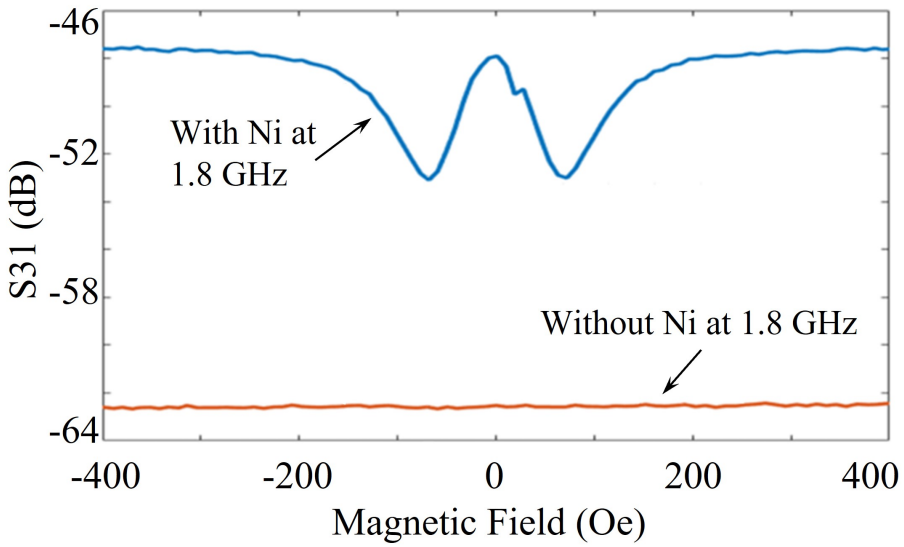

Figure 4.7: Using the shorted gold stripline through the center of the nickel film and the far IDT, a transmission measurement was taken with a network analyzer at 1.8 GHz. The orange line shows a measurement with no field dependence from a sample without nickel. The measurement for a sample with a nickel film under the gold stripline is shown by the blue line, which has two dips around $\pm$ 60 Oe that correspond to the magnetic resonance of the nickel film at this frequency.

The final electrical characterization performed using the VNA was of the nickel film independent of the SAW, to understand where the nickel's natural resonance would be. This characterization consisted of a reflection measurement S_{33}, where the signal source and receiver is the gold stripline above the nickel film. One S_{33} measurement is taken with a fixed frequency and is field swept from - 800 Oe to + 800 Oe. This can then be combined with other fixed frequency measurements with the same field sweep, to show us a field-frequency map of the nickel film energy absorption. This map is shown in Figure 4.8, where the largest nickel absorption is seen as yellow (against the non-absorbed energy in blue), which follows a characteristic Kittel dispersion curve (see Figure 2.2) for the uniform magnetic resonance of our sample. The nickel will absorb more energy when it is on resonance since the energy of the microwave signal can be transferred from the gold stripline into the precession of magnetic moments in the nickel. When off resonance, without the uniform precession, little energy can be absorbed into the nickel, so most of the energy is reflected back into the network analyzer.

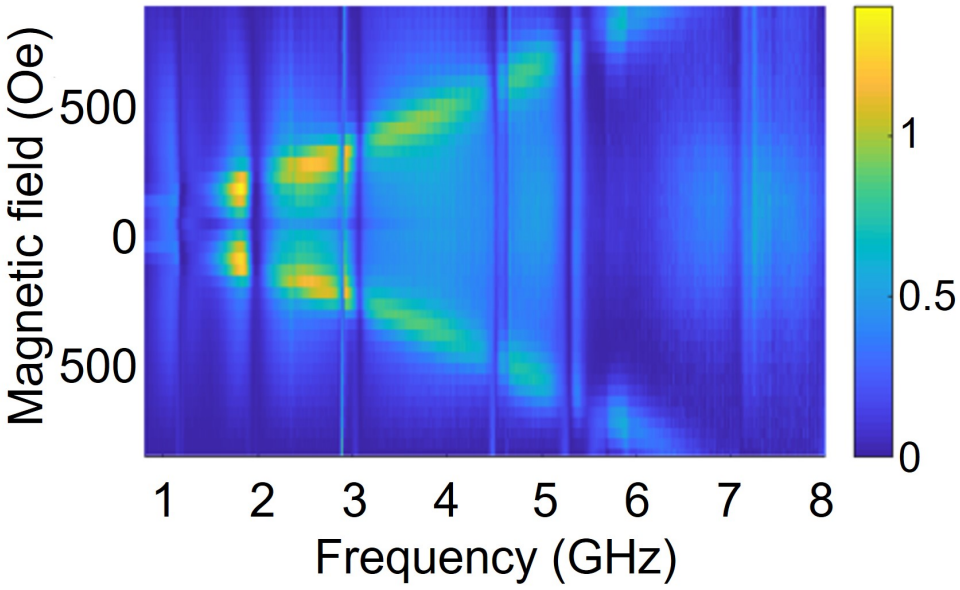

Figure 4.8: Using the shorted gold stripline through the center of the nickel film a reflection measurement was taken with a network analyzer. The high energy absorption of the nickel (yellow) shows a characteristic Kittel dispersion curve for magnetization vs frequency for a thin film.

4.6 BLS Measurements

While a single electrical measurement can be frequency swept (Figure 4.6) or field swept (Figure 4.7), a single BLS measurement looks at a range of frequencies, determined by the etalon mirror spacing, with a fixed microwave excitation frequency (1.8 GHz) sent to the the left (far) IDT and a fixed field. The BLS measurements in this chapter were all taken with a mirror spacing of 20 mm, which corresponds to an FSR of $\pm$ 7.5 GHz, where frequencies in the sample can be detected over a range of $|0.75 - 6.75|$ GHz (due to the double shutter blocking the elastic signal), with a resolution of 37.5 MHz.

Figure 4.9 shows the BLS signal intensity as a function of the magnetic field, similar to the VNA measurements in Figure 4.7. Each BLS data point corresponds to a field between - 400 Oe and + 400 Oe, and is the integrated signal intensity at $|1.8 \pm 0.3375|$ GHz, where - 1.8 GHz and + 1.8 GHz correspond to the Stokes and anti-Stokes data respectively. These BLS spectra were collected using a 1.8 GHz driving frequency sent to the left (far) IDT at 15.0 dBm to produce the SAW and was taken near the front edge of the film where the SAW first passes under/through the nickel (see Figure 4.11(c) for a single measurement) and where the signal is the strongest. While Figure 4.7 was a single field sweep from - 400 Oe to + 400 Oe, the BLS data shown in Figure 4.9 were measured starting from saturation at - 400 Oe and stepping down to 0 Oe and then resaturating the sample at + 400 Oe and again stepping down to 0 Oe. While the step size is different between Figures 4.7 and 4.9, they both show dips at the magnetic resonance of nickel ($\pm$ 60 Oe), even though resonances are normally seen as peaks in BLS measurements. The dips, rather than peaks, in both the BLS and the electrical measurements are because the magnetoelastic coupling is stronger near the magnetic resonance frequency and the process of exciting a magnetoelastic wave takes energy from the SAW, resulting in a loss of excitation amplitude. This loss in SAW amplitude is more pronounced for the electrical measurements because the stripline is roughly 130 μm from the front of the Ni pad, whereas the BLS measurements shown in Figure 4.9 are at roughly 2 μm. Moreover, some of the SAW energy goes into a mode with a different frequency ($2f$), which will be discussed later, resulting in a more pronounced dip. The BLS magnet is powered by a unipolar

power supply and a physical change in electrical connections is needed to change the field direction. The coercive field kink seen in Figure 4.7 at +15 Oe is therefore not expected in the BLS measurements.

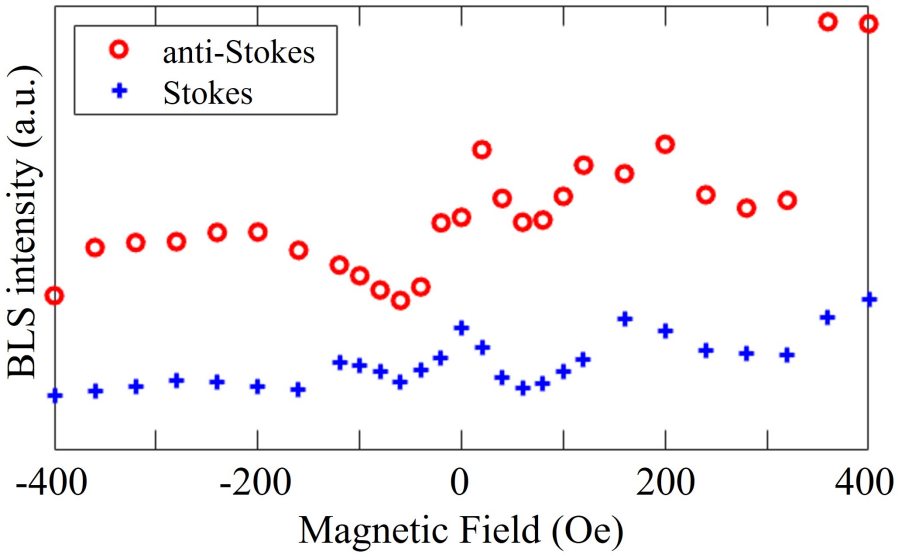

Figure 4.9: The BLS integrated intensities of the |1.8| GHz signal at roughly 2 μm from the front of the nickel film as a function of applied magnetic field separated into Stokes and anti-Stokes (added above the Stokes to be visibly separate) signals. We see results similar to the electrical measurements in Figure 4.7 with dips at the same $\pm$ 60 Oe applied field corresponding to the nickel resonance at the 1.8 GHz driving frequency (15.0 dBm) of the surface acoustic wave.

Figure 4.11 shows raw BLS spectra obtained at the positions denoted by red dots in Figure 4.5. The first point is on the $LiNbO_3$ substrate as a control measurement, then BLS spectra were also obtained at five other positions on the nickel that are evenly spaced roughly 32 μm apart starting 2 μm inside the front edge of the nickel and ending at a point just before the gold stripline. By looking at the signal attenuation as a function of distance, we can gain insight into the decay length of the magnetoelastic wave. Figure 4.10 shows the micro-BLS camera image where the red crosshairs denote the location that the data was taken for the $LiNbO_3$ (a), 2 μm inside the front edge of the nickel (b) and the last point on the nickel just before the gold stripline (c).

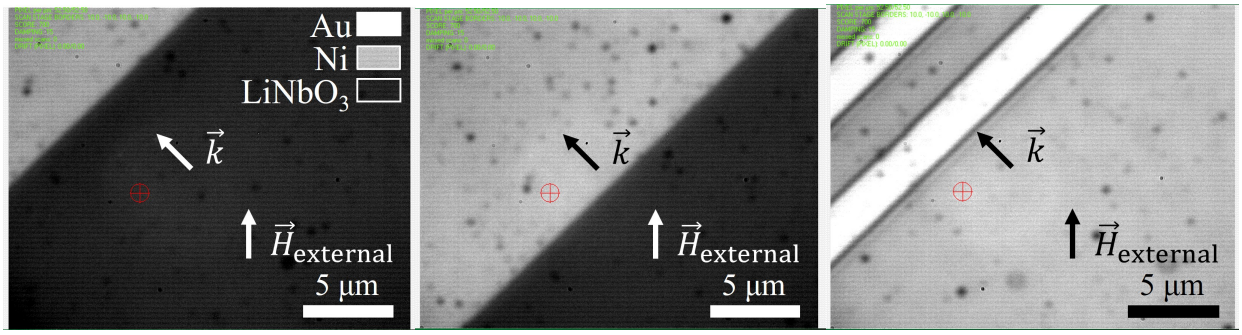

(a) **(b)** **(c)**

Figure 4.10: Measurement positions denoted by the red crosshairs as seen from the micro-BLS camera on (a) the $LiNbO_3$ substrate seen as dark grey material, (b) the front of the nickel film seen as light grey material, and (c) the nickel film (light grey) just before the gold stripline (white stripes). The material labels in shown in (a) also apply to (b) and (c). Each camera image shows a sample view roughly $20 \times 22\,\mu m^2$.

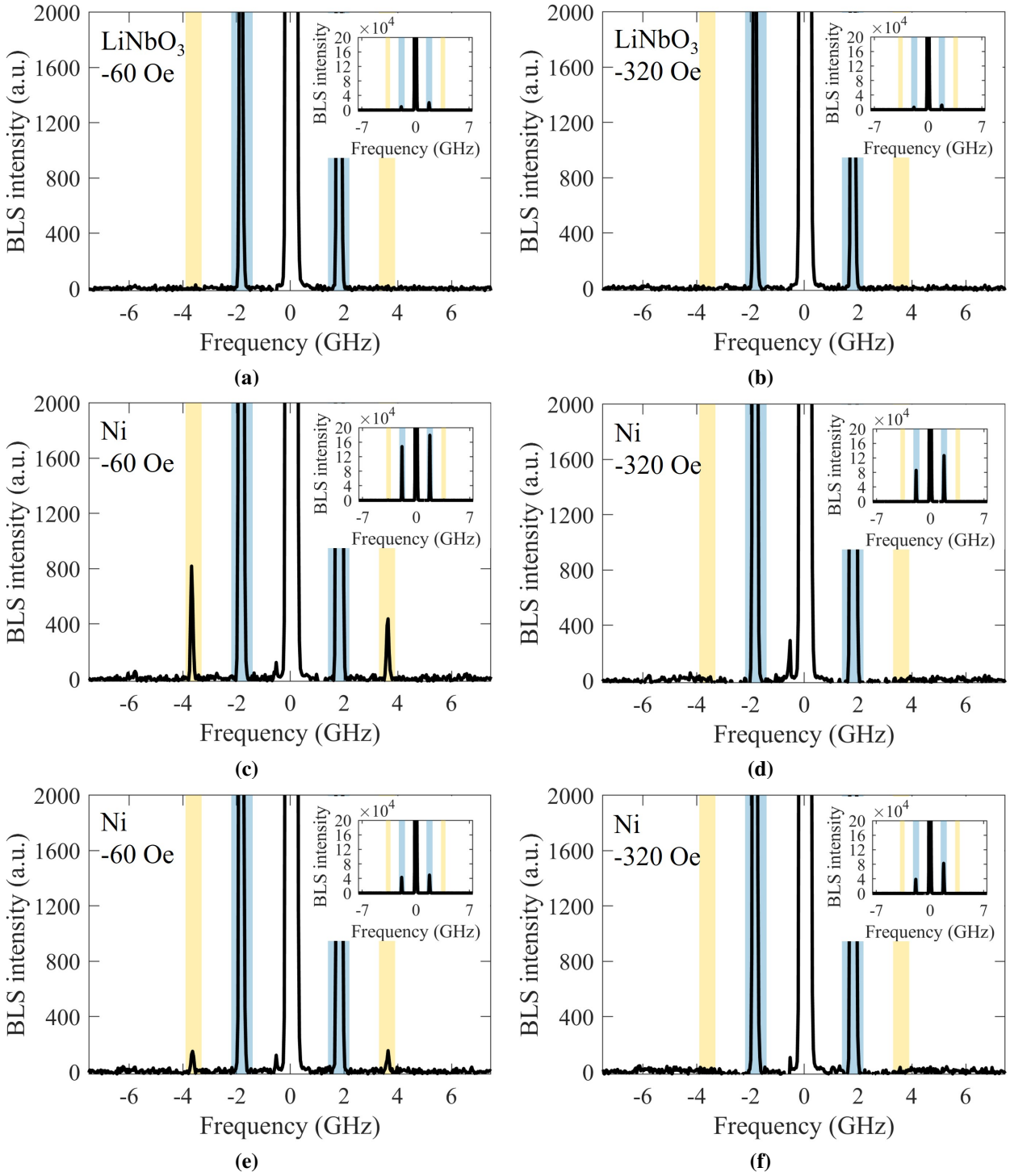

Figure 4.11: These measurements were taken at the following positions: (a) and (b) are on the $LiNbO_3$ in front of the nickel film, (c) and (d) are at the front edge of the nickel film, and (e) and (f) are on the nickel film just before the gold stripline. Measurements (a), (c), and (e) are taken at - 60 Oe, which aligns with the nickel resonance, whereas (b), (d), and (f) are taken at - 320 Oe, which is off-resonance. The blue highlight is the 1.8 GHz peak and the gold highlight is the $2f$ signal at 3.6 GHz in the nickel film data for the on-resonance (- 60 Oe) data. The insets are the same data but with a different y scale to see the full 1.8 GHz peaks.

Figure 4.11 shows measurements on $LiNbO_3$ at - 60 Oe (a) and - 320 Oe (b) and at the first position (c) and (d) and last position (e) and (f) on the nickel film at the same fields as the $LiNbO_3$. All BLS measurements were taken with a laser power of 5.24 mW, measured just before the microscope objective. The sample was saturated with a field of |500| Oe for >10 minutes to ensure the measurements started in the same magnetic configuration and to allow the magnet to equilibrate. The field was then ramped down to |320| Oe where it was again allowed to equilibrate before data was taken at all 6 positions. The field was then ramped down further to |60| Oe and data was again collected at all six positions after sufficient time for the magnet to equilibrate. The BLS signal from the $LiNbO_3$ is due to the elastic components and ripple of the SAW, whereas the signal from the nickel film is partially due to the ripple of the SAW and partially due to the coupled magnetoelastic wave. While a direct comparison between the $LiNbO_3$ and nickel film signal intensities may seem like a straightforward way to separate the signals, the $LiNbO_3$ is transparent to the 532 nm laser light, whereas the nickel is highly reflective such that the optical coupling is different between the two materials. This difference means that with our current setup, there is no way to separate the ripple component of the SAW from the magnetoelastic component in the nickel.

The first thing to note in Figure 4.11, is that all measurements show a pronounced signal at 1.8 GHz highlighted in blue, where the insets to Figure 4.11 show the full intensities of the 1.8 GHz signal. In addition to the 1.8 GHz driving frequency of the SAW, we also see a signal on the nickel film at $2f$ = 3.6 GHz (highlighted in gold, but only seen in Figures 4.11(c) and (e)). This $2f$ signal requires both the driven SAW and the nickel film, but is seen with an a external field of - 60 Oe and not with an external field of - 320 Oe. This field dependence can be explained in part by the dispersion curves for our nickel film seen in Figure 4.12. At lower fields, the backward volume mode (red curve) and Damon-Eshbach mode (blue curve) bound a region (grey) where there are numerous modes available for the 1.8 GHz (green dashed line) to transfer energy. When the external field matches with the nickel resonance at |60| Oe, the magnetic oscillations and their contribution to the magnetoelastic wave is at a maximum making the nonlinear $2f$ signal appreciable as it pulls energy from the 1.8 GHz mode (the dips seen in Figure 4.9). When the external field is at |320| Oe, well

above the nickel resonance, the magnetic oscillations are reduced in the nickel, and this reduction of the magnetic contribution decreases the $2f$ signal below the background noise level of the BLS measurements. Mathematically, the nonlinear $2f$ signal is a higher order term, often neglected because the contribution to the overall signal is so small. The integrated BLS signals between the f and $2f$ differ by over two orders of magnitude, which further underlines how small the $2f$ signal is.

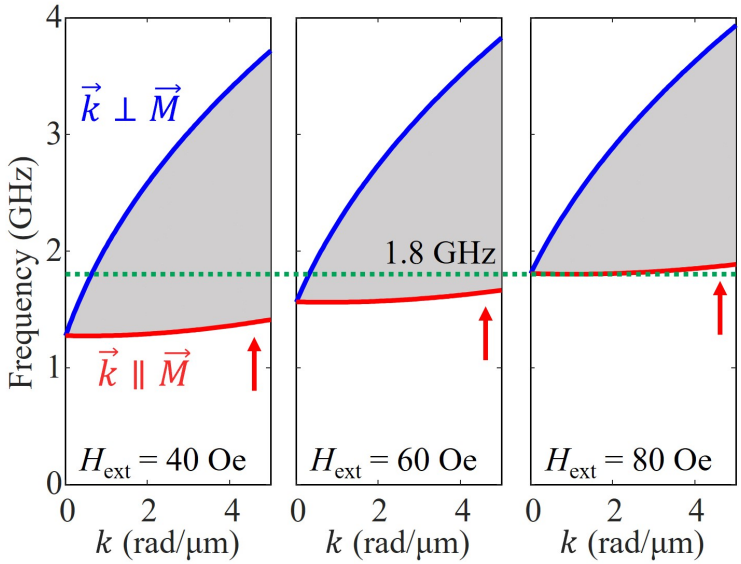

Figure 4.12: Dispersion curves for the nickel film shown for both backward volume (red curve) and Damon-Eshbach surface mode (blue curve) geometries. A 1.8 GHz frequency (green dashed line) would have numerous available modes (shaded grey region) where energy can be transferred.

To examine the decay profile of the wave further, the BLS intensity for each of the peaks observed in Figure 4.11 (1.8 GHz and 3.6 GHz where applicable) were integrated and normalized to the signal of the integrated reference peak to account for laser power fluctuations. The integrated signal intensity vs. position on the nickel film is shown in Figure 4.13 for the anti-Stokes peaks at - 60 Oe (a) and - 320 Oe (b). The black diamonds in Figure 4.13 correspond to the 1.8 GHz peak data, whereas the red circles correspond to the 3.6 GHz peak data, each of which is then fit separately with an exponential decay function,

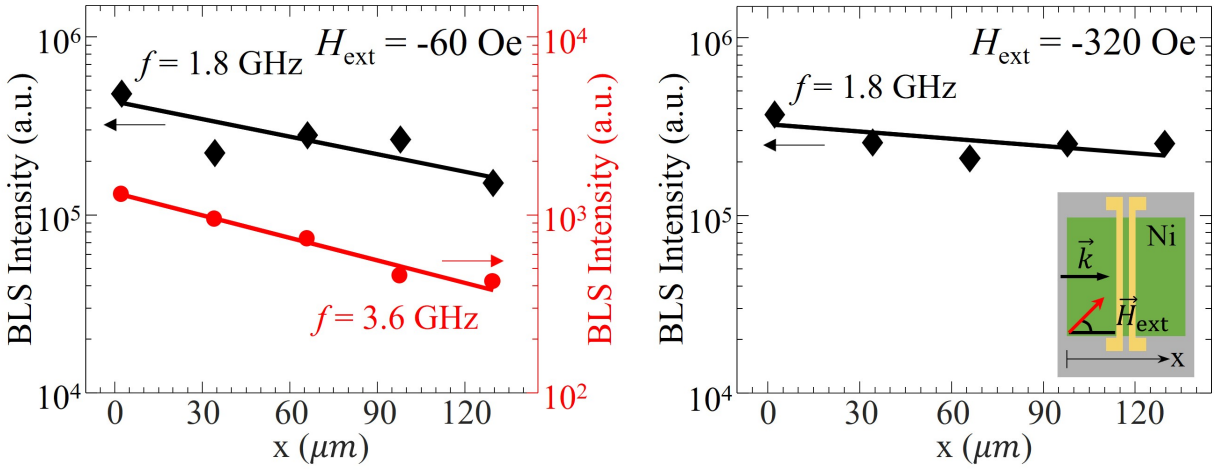

Figure 4.13: Integrated peak intensities for an externally applied field of - 60 Oe (a) and - 320 Oe (b). Each field and frequency data set was fit separately with a exponential decay function to obtain the decay lengths for the magnetoelastic waves at 1.8 GHz and 3.6 GHz. The schematic in (b) also applies to (a).

$$I = I_0\, e^{-x/d}, \tag{4.1}$$

and shown as a line corresponding to the displayed data color. In Equation (4.1), x is the distance of the measurement from the front of the nickel, d is the fitted decay length, I is the intensity at a given x, and I_0 is the initial intensity at x = 0. The anti-Stokes (positive frequency shift of BLS photons) decay lengths for the 1.8 GHz and 3.6 GHz signals with an external field of - 60 Oe are $135 \pm 57\,\mu$m and $109 \pm 23\,\mu$m, respectively, corresponding to the fits in Figure 4.13(a). The decay length for the 1.8 GHz signal with an external field of - 320 Oe, seen in Figure 4.13(b), is $319 \pm 252\,\mu$m, almost a factor of three larger, but also with a significantly larger error.

Similar fits were done for the Stokes peaks (negative frequency shift of BLS photons, decay length plots not shown) with an external field of - 60 Oe, giving decay lengths of $131 \pm 29\,\mu$m and $61 \pm 42\,\mu$m, for 1.8 GHz and 3.6 GHz respectively and $138 \pm 40\,\mu$m, for the 1.8 GHz peak with a field of - 320 Oe. These decay lengths are similar in magnitude to the anti-Stokes decay lengths and are at least an order of magnitude larger than decay lengths expected for pure spin waves in a nickel film with similar physical properties as the film along our surface acoustic wave delay line.

4.7 Summary and Future Directions

The IDT delay line S_{21} measurements by our collaborators showed strong transmission of a 3rd harmonic SAW at 1.8 GHz that we used to excite and directly measure magnetoelastic waves in a nickel sample. Both VNA and BLS measurements as a function of field show a resonance for the nickel film at ± 60 Oe. The BLS data also displayed a nonlinear $2f$ signal at 3.6 GHz. BLS measurements at various locations along a nearly $130\,\mu$m line starting at the front edge of the nickel film and moving to just before the gold stripline using a micro-focus Brillouin light scattering method. These measurements revealed a magnetoelastic decay length almost two orders of magnitude longer than an uncoupled/pure spin wave in nickel, but still an order of magnitude below a uncoupled SAW in $LiNbO_3$. By having a wave with components of both a spin wave and SAW, the decay length magnitude is between the decay length magnitudes of the uncoupled components. Further study of these coupled waves may lead to the ability to tune the decay length based on the wave components.

Future directions of this project would include remaking samples without the "invasive" gold stripline across the nickel and taking more measurements spaced closer together but over a larger distance to calculate decay lengths with a higher precision. The gold stripline is considered invasive based on a large signal loss that can only be attributed to the stripline. BLS measurements taken just before the gold stripline for the integrated 1.8 GHz signal with a field of - 60 Oe average 1.3×10^5 counts between the Stokes and anti-Stokes peaks. Based on the decay length, on the other side of the gold stripline (approximately $12\,\mu$m away) we would expect 1.2×10^5 counts or a signal loss of around 9%. However, integrated BLS measurements on the far side of the gold stripline for the same field and SAW frequency are are roughly 6250 counts, a 95% decrease that can not be explained by the decay length and therefore must be due to the gold stripline.

Additional future directions for this project could involve taking BLS data with incrementally varying RF power to the IDTs to help give us more information about the efficiency and nonlinear coupling of the $2f$ signal. Taking time-resolved measurements of a 2D spatial scan using the micro-

BLS might also be insightful to see how the magnetoelastic wave propagates and how localized defects effect the propagation.

Chapter 5

Vanadium Tetracyanoethylene

5.1 Context

The following chapter discusses my work using Brillouin light scattering measurements of phonons, used in conjunction with phonon simulations, to characterize the materials used for the encapsulation of vanadium tetracyanoethylene films. This work is a part of a collaboration with the Johnston-Halperin group at The Ohio State University who grew the samples, the Flatté group at the University of Iowa who have worked on the theoretical calculations and simulations, and the Tang group at Yale University who worked on low temp measurements and application integration. The work described here is part of a manuscript in progress.

As technology advances, society expects more from their devices. We want them smaller and lighter, we want the battery to last a long time before needing to recharge, but we also want them to handle large amounts of data like pictures, videos, games, or telecommunications from anywhere in the world. Essentially we want devices to be efficient, not only in terms of energy consumption but also in terms of how we utilize them. As the future progresses, the idea of transparent devices or flexible screens emerges, to increase functionality and ease of use. However these futuristic ideas (perhaps seeming more like science fiction than a realistic product) require research to develop and study new materials since our current materials do not have the capabilities required to make these ideas work. Yttrium iron garnet (YIG or $Y_3Fe_5O_{12}$) is a magnetic insulator that has been used for decades in microwave devices due to its incredibly low damping [24, 75, 95, 116–121], though it does have some drawbacks when considered for future devices. The need for YIG to be grown on a latticed matched substrate for high quality films, severely limits the substrate to a crystal called gadolinium gallium garnet (GGG or $Gd_3Ga_5O_{12}$) [95, 117, 118]. Both YIG and GGG are not flexible, nor are they compatible with flexible substrates. Additionally, high quality YIG is deposited by liquid phase epitaxy (LPE), pulsed laser deposition (PLD), or sputtering deposition

each of which utilize high temperatures (>700° C) during deposition or for an annealing step after deposition [122–124].

A newer material with damping similar to YIG is vanadium tetracyanoethylene (VTCNE). This room-temperature magnetic insulator is a polymer-like organic material first developed in 1991 [125], and may eliminate many of the drawbacks associated with YIG while still maintaining high quality magnetic films [126, 127]. VTCNE has a soft polymer-like flexibility, which has no lattice matching requirements, the deposition temperatures are only a little above room temperature (∼60° C), and it is patternable without large changes in the magnetic damping [128] making VTCNE a potential alternative to YIG in some microwave circulator designs [127] and more favorable for future flexible technology.

This project studies phonons and the elastic properties for an encapsulated vanadium tetracyanoethylene (VTCNE) film. This is an organic material that is oxygen sensitive [125, 129–133] and therefore must be sealed in an zero oxygen environment to prevent oxidation and material degradation. Recent evidence points to the material being magnetostrictive so the encapsulation materials must be studied to understand their elastic properties since their stress and strain could impact the VTCNE. I have used Brillouin light scattering (BLS) together with simulations to determine elastic constants of the glass and an encapsulation stack without the VTCNE (glass-epoxy-glass). These can then be compared to theory calculations and used for future encapsulation models and calculations.

5.2 Sample Design

VTCNE is an organic ferrimagnetic insulator [125, 129–136] with coupling between the vanadium ion and the tetracyanoethylene molecule that creates no long range crystal or polymer structure, but does create a long range magnetic order. Our samples are grown by our collaborators at the Ohio State University in a glove box using chemical vapor deposition (CVD) methods [129, 130, 137]. The deposition setup is illustrated in Figure 5.1.

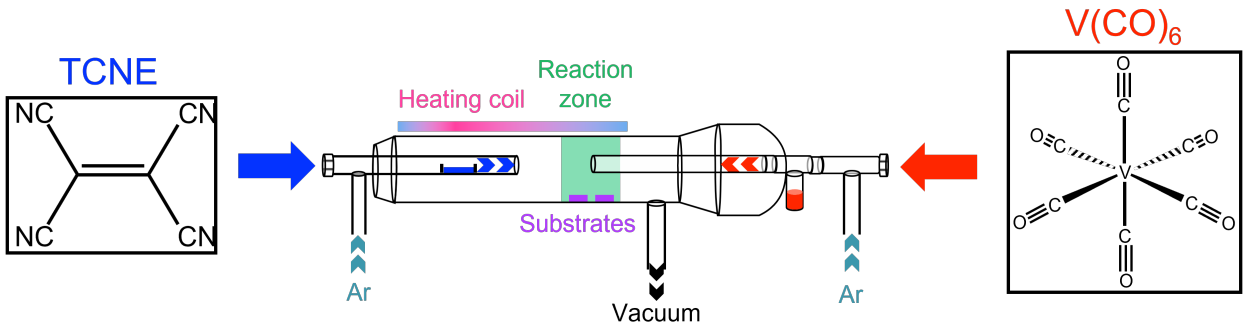

Figure 5.1: A schematic showing the deposition set up at OSU with precursor chemical structures. Diagram reproduced with permission from Ref. [138].

The substrates and two precursors are heated to 50-60° C and then use an inert argon gas to flow to the reaction chamber where they interact and deposit on a substrate [137]. As mentioned previously, this material is softer, more polymer-like, and does not require lattice matching like YIG in order to grow high quality films, so VTCNE can therefore be grown on both rigid and flexible substrates [126,127,130,139,140]. This deposition process enables some conformal deposition (the coating of structure sidewalls and other structure contours, in addition to the horizontal surfaces) [139], which is of particular interest for magnonic crystals [24]. The samples measured by BLS require encapsulation and optical access so the VTCNE is grown on a borosilicate glass. The VTCNE coated glass is then covered in an epoxy designed for OLEDs (organic light emitting diodes) and flipped over onto a slightly larger piece of glass and then cured using ultraviolet light [141]. In order to excite the VTCNE magnetically, the second piece of glass can be substituted with a piece of sapphire that has a gold coplanar waveguide patterned onto it similar to what is seen in Figure 5.2(b).

Tests have shown that this encapsulation does not effect the VTCNE damping. Furthermore, the encapsulation extends the sample lifetime from hours to weeks allowing the samples to be shipped from Ohio to Colorado where we can make BLS measurements and VNA measurements if the sample has an antenna. In addition to oxygen sensitivity, there are other degradation mechanisms under review that reduce and can eventually eliminate the sample magnetization, one of which

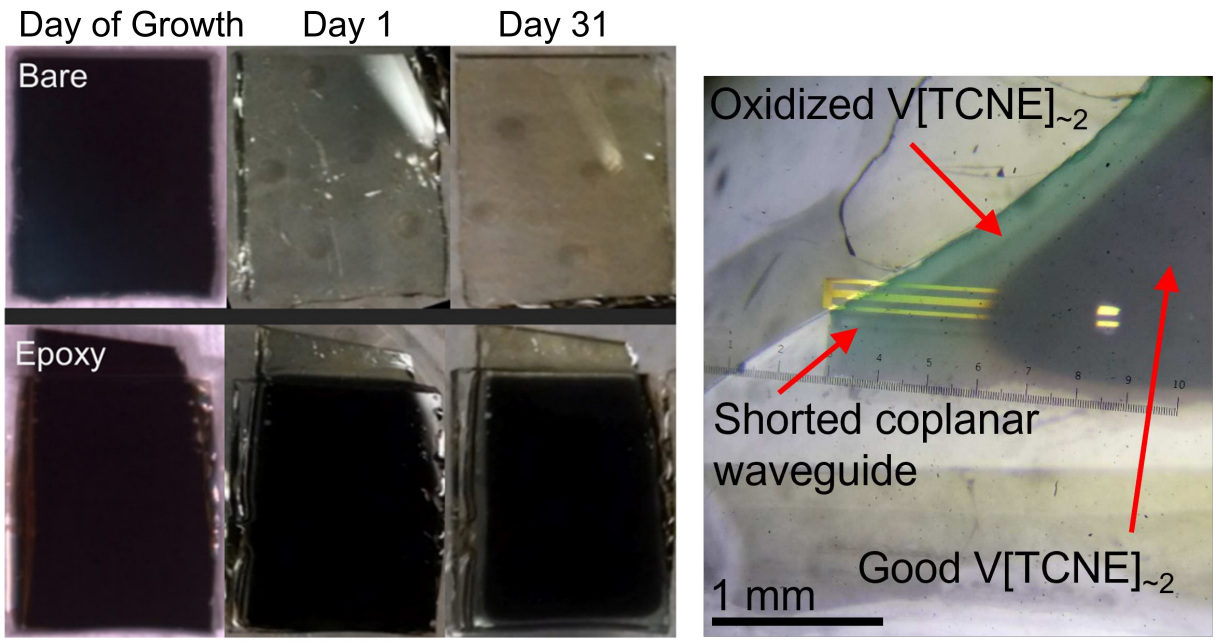

(a) **(b)**

Figure 5.2: (a) Time-lapse photographs of VTCNE samples show the difference between an epoxy encapsulated VTCNE sample vs a bare (unencapsulated) VTCNE sample when exposed to air at various times. When the VTCNE is initially deposited, it is an opaque black film. In less than one day the bare film oxidizes and becomes transparent, whereas after a month, the encapsulated sample is still generally opaque with degradation only at the edges, which are now transparent. Figure reproduced with permission from [141]. (b) Optical microscope image of an encapsulated VTCNE film over a patterned coplanar waveguide. The image shows the edge of an epoxy encapsulated sample where the oxidation of VTCNE has become a transparent blue color compared to the opaque black color of an unoxidized VTCNE film.

includes heat component. To prevent any degradation from excessive heat while in transit, samples were also shipped in dry ice and stored in a freezer upon arrival.

5.3 Experimental Setup

Recent evidence has suggested that VTCNE is magnetostrictive and is highly affected by strains or stresses in its environment [142]. So before VTCNE can be incorporated into devices, we must first characterize the elastic properties of the encapsulation materials, particularly the epoxy after it cures. I performed these characterizations using a conventional 180° back scattering BLS configuration with a laser power of 71.5 mW focused to a spot size of roughly 30 μm. The sample focus was determined by finding the focus on the sample mount and then adjusting for the thickness

of the sample up to the glass/VTCNE interface or the glass/epoxy interface when VTCNE was not present and then minor focus corrections were made based on bulk mode intensities. These were measured with the TFP1 described in Chapter 3. BLS measurements were collected without any polarization dependence allowing both p- and s- polarized light to enter the interferometer. The data were also taken with a polarizer (extinction ratio of 3500:1) placed between the sample and the interferometer to reduce the laser light that did not rotate its polarization upon scattering from the sample. This polarizer helps increase the relative intensity of any signal with rotated polarization.

Additional measurements were attempted using the micro-focus BLS with a laser power of $\sim$2 mW before the microscope objective and an excitation antenna. While the antenna allowed for FMR measurements with the VNA, the focusing of the laser through the top glass slide on the VTCNE did not provide a strong enough signal to measure with the BLS. Instead of a polarizer, the micro-focus BLS used a polarizing beam cube just above the sample, which was later swapped to a non-polarizing beam cube. While trying to focus on the VTCNE through the glass, the correct focus resulted in the immediate burn or destruction of the VTCNE visible on the CCD camera Figure 5.3 and by eye after removing the sample from the sample mount Figure 5.4.

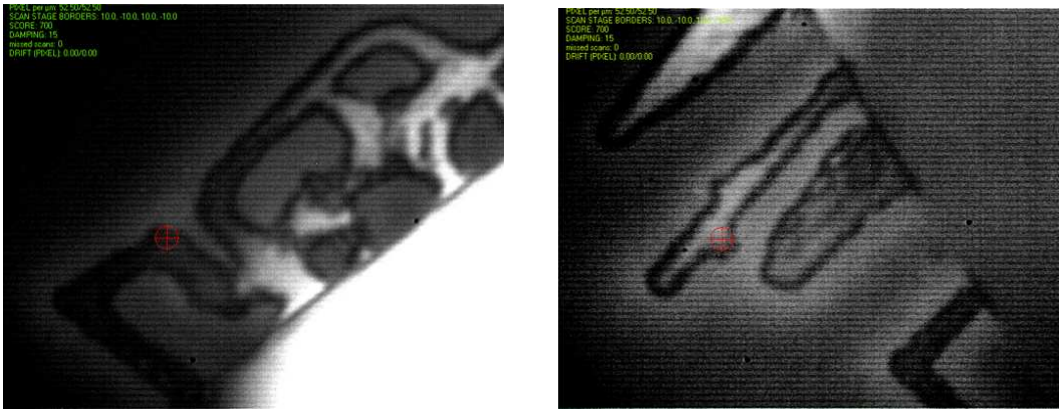

(a) **(b)**

Figure 5.3: As seen by the micro-focus BLS CCD camera, the laser position beneath the red cross-hair damages the VTCNE. (a) is above the highly reflective gold antenna, seen as white in the bottom right corner, so the laser-burned VTCNE becomes transparent and shows as white because we are seeing the gold underneath. (b) shows similar laser damage but only on exposed VTCNE, where there is no damage once the laser passes over the broken edge and onto the cover glass. Each figure is roughly $20\times22\,\mu$m

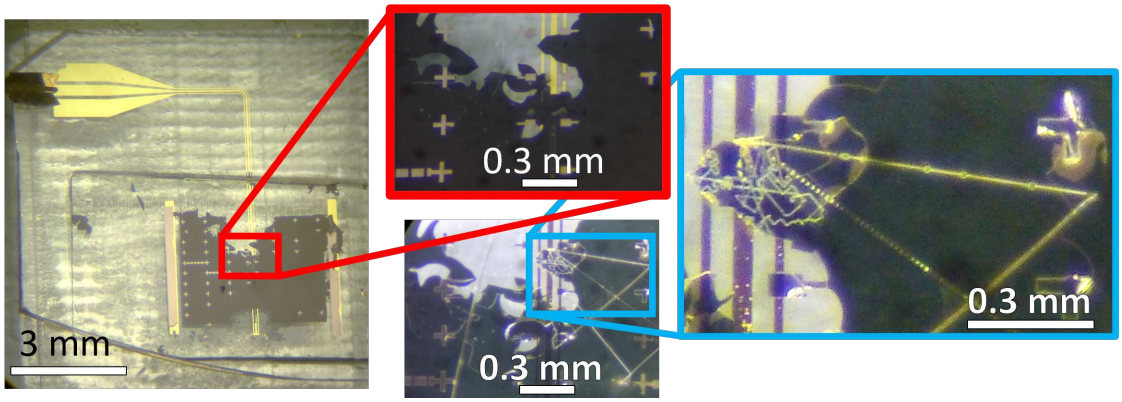

Figure 5.4: On the left is a full sample image with a specified magnified region before laser damage. The center two images show the same area before (top) and after (bottom) laser damage. A magnified image of the laser damage is shown on the right, where laser damage is seen as transparent spots and lines depending on the length of time the laser was at that location.

This degradation of the VTCNE was permanent and visible as transparent lines through the otherwise black VTCNE. The damage was quite localized to the laser; however, any pause where the laser was at the same position for even a brief moment resulted in a transparent spot larger than the thickness of the line while the sample was in motion. This degradation was likely from too high a laser power density, which resulted in a local VTCNE temperature capable of breaking the VTCNE chemical bonds and localized sample death [143]. Due to the high laser power density of the micro-BLS, the antenna driven VTCNE samples were no longer a viable sample option. I shifted back to measurements with the conventional 180° back scattering BLS configuration, because the larger spot size corresponds to a lower laser power density, discussed in the following section.

5.4 Experimental Results

Brillouin light scattering measurements were taken with a single piece of encapsulation glass with a thickness of approximately 100 μm where the laser focus was tens of microns inside the glass as measured from the top surface. The incident laser angle (θ), measured from the surface normal of the sample (Figure 5.5(b)), was used to help distinguish surface waves from bulk waves. BLS measurements taken at θ = 30°, 45°, 60°, and 70° are shown in Figure 5.5(a) both with and

without a polarizer to block the portion of the sample beam with the same polarization as the incoming laser beam.

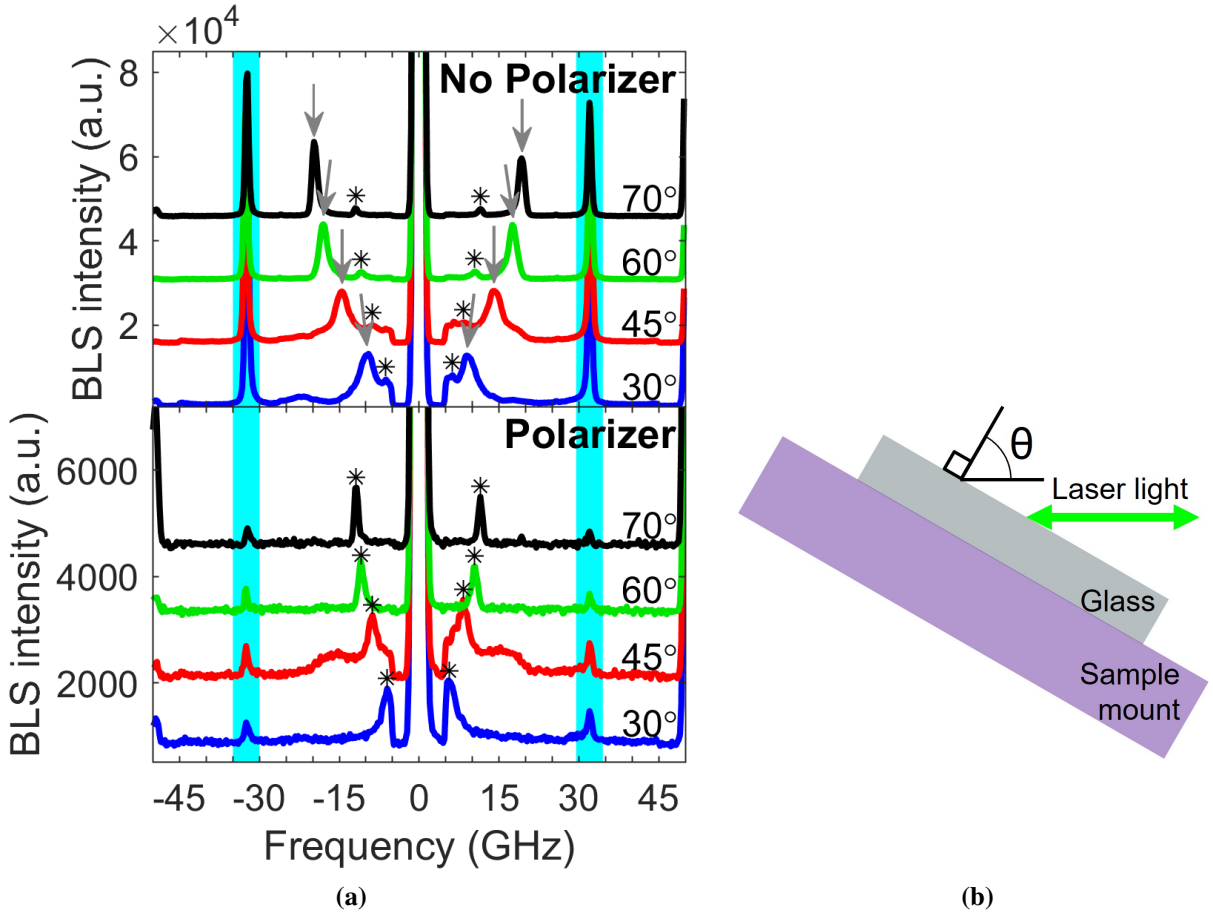

(a) **(b)**

Figure 5.5: (a) BLS scans for a single piece of glass are shown for θ = 30°, 45°, 60°, and 70° with no polarization dependence (top) and with a polarizer (bottom). The polarizer is set to block most of the sample signal with the same polarization (vertical) as the laser incident on the sample, i.e., all rotated laser light back-reflected from the sample will have a higher relative intensity in the BLS scans. The cyan stripes highlight peaks identified as the bulk longitudinal mode in glass. The peaks marked with an arrow $\downarrow$ or asterisk $*$ are the surface longitudinal mode and the surface shear horizontal mode respectively. Each data set has been individually normalized with offsets for visual clarity. (b) A side view sample schematic (not to scale) that shows the angle θ between the sample normal and incident laser direction.

In Figure 5.5(a) the cyan stripes denote peaks that do not change frequency as θ changes, which is indicative of a bulk mode. Based on our set up geometry this is the longitudinal bulk mode of the glass around $f \approx 32$ GHz. There are two modes that do change frequency as θ changes, which is indicative of a surface modes. In the data taken with a polarizer in place, peaks noted with an

asterisk $*$ have a higher intensity compared to the bulk mode measured at the same θ. Conversely, in the data taken without a polarizer the $*$ peaks (at the same frequency as the $*$ peaks in the data taken with a polarizer) are at much lower intensities than the glass bulk peaks. The relative intensity difference is evidence that the laser light of this signal was rotated in the scattering process. This polarization rotation, along with the frequency shift for the different θ measurements, indicate that this is the surface transverse mode known as the shear horizontal mode (SHM). Finally, the peaks denoted with arrows $\downarrow$ consistently have higher frequencies than the shear horizontal surface mode peaks and are also not visible in the data taken with the polarizer in place, which identifies these peaks as longitudinal surface modes.

After the glass modes have been identified, we can move to an epoxy sample where two pieces of glass are sandwiched together with the OLED epoxy. This is similar to the conditions that the VTCNE will be encapsulated in giving us the most practical characterization of the encapsulation materials. The epoxy thickness is a couple micrometers thick and the laser is focused at the top-most epoxy-glass interface. Once again measurements with θ = 30°, 45°, 60°, and 70° were used to help distinguish surface waves from bulk waves.

The measurements in Figure 5.6(a) are similar to the measurements found in Figure 5.5(a), so the mode identification will also be similar. The peak frequency that does not shift with θ at roughly 32 GHz is the glass longitudinal bulk mode (cyan highlight) and an additional bulk mode (no θ dependence) at $f \approx 16$ GHz (salmon highlight) is therefore the longitudinal bulk mode of the epoxy. The surface longitudinal mode in this glass-epoxy-glass sample (marked with arrows $\downarrow$) is identified the same way as was done in the glass only sample. Its peaks are at higher frequencies than the transverse surface mode(s), the frequencies depend on θ, and the peaks only appear in the data taken without the polarizer. Additionally, the peak frequencies for the glass-epoxy-glass sample have the same frequencies as those in the glass only measurements for each respective θ. The shear horizontal mode (denoted with an asterisk $*$) can still be identified by having a larger relative intensity (compared to the longitudinal bulk peaks) in the data taken with the polarizer, its θ dependent frequency shift, and by matching the frequencies of the peaks to those

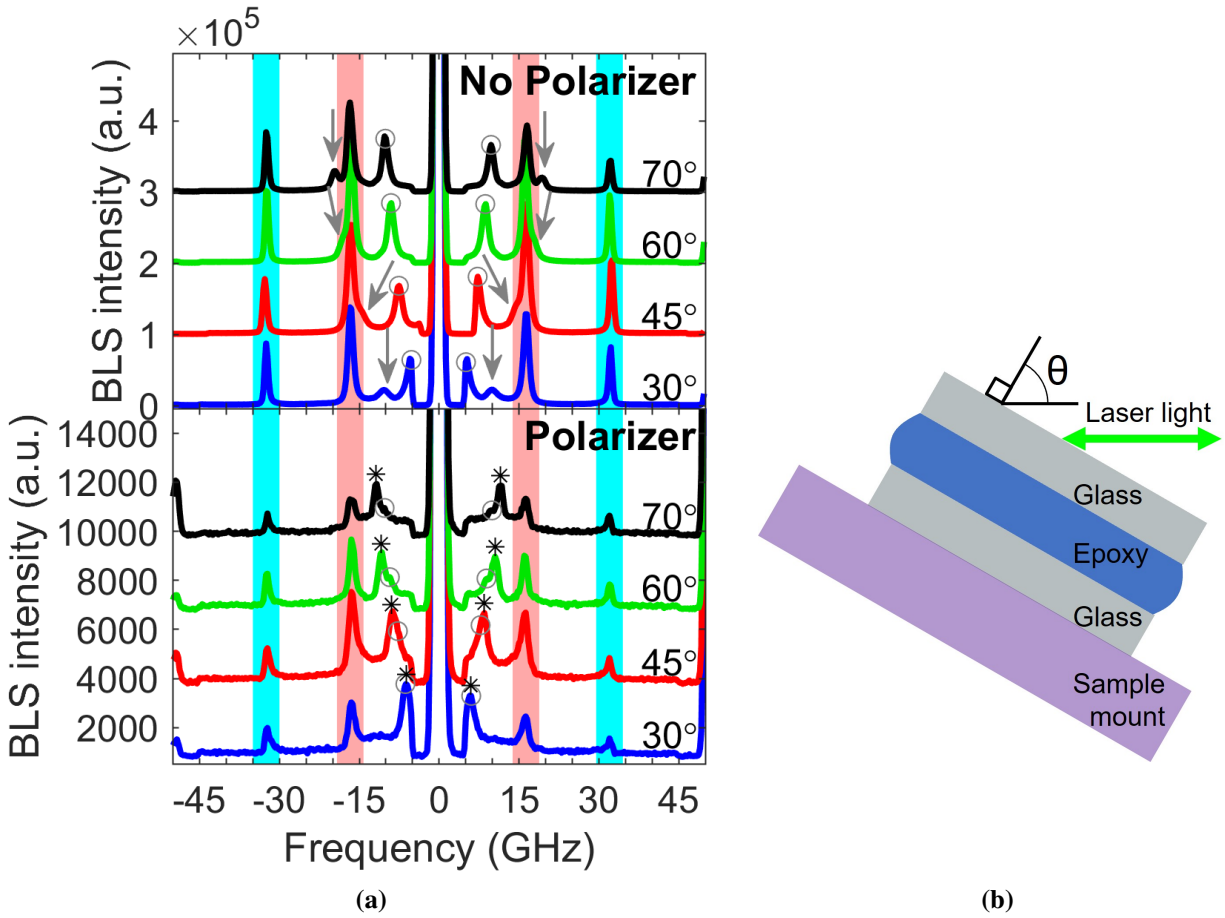

Figure 5.6: (a) BLS scans for a thin epoxy layer sandwiched between two pieces of glass are shown for $\theta = 30°$, 45°, 60°, and 70° with no polarization dependence (top) and with a polarizer (bottom). The polarizer is set to block most of the sample signal with the same polarization (vertical) as the laser incident on the sample, i.e. all rotated laser light back reflected from the sample will have a higher relative intensity in the BLS scans. The cyan colored stripes highlight peaks identified as the bulk longitudinal mode in glass, whereas the salmon colored stripes highlight peaks identified as the bulk longitudinal mode in epoxy. The peaks marked with an arrow ↓, circle ◯, or asterisk ∗ are the surface longitudinal mode, the Rayleigh mode, and the surface shear horizontal mode respectively. Again, each data set has been individually normalized with offsets for visual clarity. (b) A side view sample schematic (not to scale) that shows the angle θ between the sample normal and incident laser direction.

found for the SHM peaks in the glass only data. The measurements without a polarizer in the top of Figure 5.6(a) have intense peaks in a similar location to the SHM peak, but upon close inspection of the data taken with the polarizer, we notice this peak frequency (denoted with a circle ◯) corresponds to the frequency of a "shoulder", or overlapping peak, with the shear horizontal surface mode. This shoulder is always at a slightly lower absolute frequency and separates from the SHM peak as θ increases. This peak is identified as the Rayleigh mode, believed to exist at the glass-

epoxy interface. The frequencies used for comparison were determined by fitting the data with the Lorentzian line shapes

$$\mathscr{L}_{\text{single}}(f) = A_1 e^{-(f-c_1)^2/(2w_1^2)} + B, \tag{5.1}$$

for a single peak that did not overlap any other peaks and

$$\mathscr{L}_{\text{double}}(f) = A_1 e^{-(f-c_1)^2/(2w_1^2)} + A_2 e^{-(f-c_2)^2/(2w_2^2)} + B, \tag{5.2}$$

for when two peaks overlapped. Here, f is the frequency along with the following fit parameters: A is the amplitude, c is the central frequency of the peak, w determines the width of the peak, and B helps compensate for the background signal with the vertical offset. The subscripts of 1 or 2 simply denote for which peak the fitting parameter is for. These fits allow for careful frequency comparisons of the BLS peaks even when the SHM and Rayleigh modes overlap, or when the surface longitudinal mode passes through the bulk longitudinal mode of the epoxy θ changes.

The central frequencies determined from the Lorentzian fits can also be plotted as a function of θ (Figure 5.7) to confirm bulk peaks do not shift frequency as θ changes and to fit the identified modes to extract a phonon speed. By combining the definition of the wave velocity (Equation (3.4)) and the wavevector definitions (Equations (3.2) and (3.3)) from section Section 3.1.1, the frequency for surface wave modes are

$$f_{\text{surface}}(v, \theta) = \left(\frac{v}{2\pi}\right) 2\sin(\theta) \left(\frac{2\pi}{\lambda_{\text{laser}}}\right), \tag{5.3}$$

along with the frequency for the bulk modes

$$f_{\text{bulk}}(v, n) = \left(\frac{v}{2\pi}\right) 2n \left(\frac{2\pi}{\lambda_{\text{laser}}}\right). \tag{5.4}$$

Wavevectors for bulk modes rely on the index of refraction n, along with the laser wavelength λ_{laser} and phonon speed v to determine the frequencies f. The surface modes do not use the index of refraction, and instead have the θ dependence with the form $\sin(\theta)$.

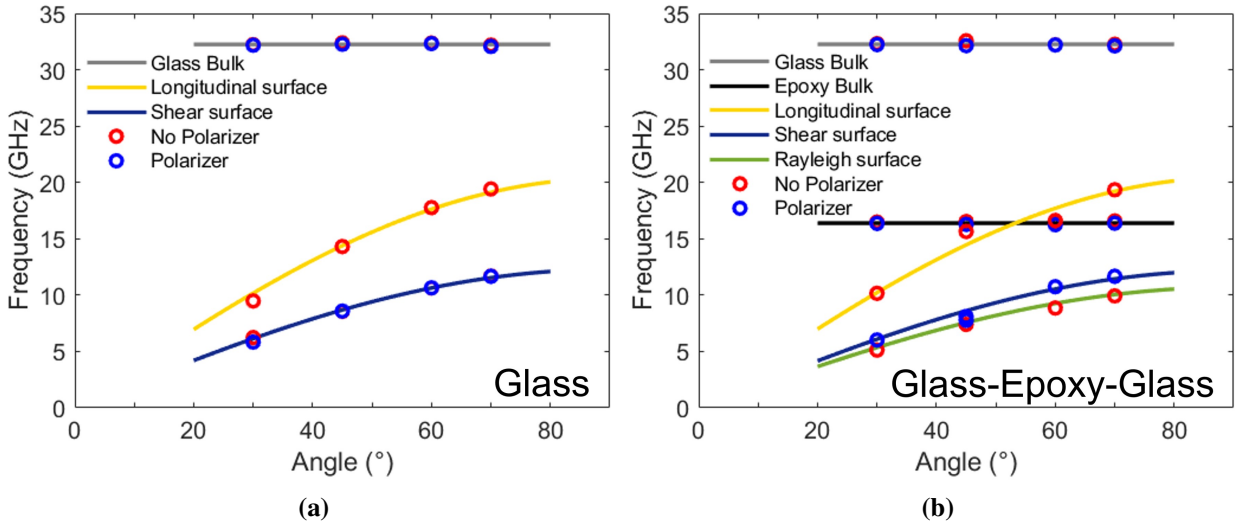

Figure 5.7: After peak frequencies were extracted from individual data sets, they were plotted as a function of θ, where (a) is for the glass only sample (frequencies extracted from data in Figure 5.5(a)) and (b) is for the glass-epoxy-glass sample (frequencies extracted from data in Figure 5.6(a)). Circles are data and lines are the fits from which the wave speeds were extracted. Horizontal lines (no change in frequency) are from the bulk modes. Surface waves change frequency with θ as seen by data fit with Equation (5.3) displayed as the the curved lines.

Each identified phonon mode was fit separately and the best fits for each are shown in as lines (bulk modes) or curves (surface modes) in Figure 5.7 allowing for the determination of v. The glass bulk longitudinal speed was calculated from the data using Equation (5.4) to be 5623 m/s and 5625 m/s based on the glass and glass-epoxy-glass data, respectively, where the index of refraction given by the manufacturer to be n = 1.5255. The epoxy bulk longitudinal mode was similarly calculated from the glass-epoxy-glass data to be 2915 m/s, using the manufacturer listed index of refraction of n = 1.4957. For the glass and glass-epoxy-glass samples, the surface longitudinal mode, calculated from Equation (5.3), was 5414 m/s and 5439 m/s, respectively, and the surface shear horizontal mode was 3268 m/s and 3239 m/s, respectively. The Rayleigh mode wave speed

was calculated to be 2846 m/s, which was similar though slightly slower than surface shear horizontal mode speed as expected.

Because glass is a common and inexpensive sample substrate there are numerous measurements of the bulk longitudinal wave speed consistent with the 5623 m/s we measured. As a result of the back scattering geometry we are unable to measure the bulk transverse wave speed, though both longitudinal and transverse bulk wave speeds are needed to determine elastic constants like Young's modulus, bulk modulus, the 1st and 2nd Lamé parameters, or Poisson's ratio. To find the transverse bulk speed we can start by looking at the wave speeds in the glass only sample. The surface longitudinal speed is roughly 96% of the bulk longitudinal mode and we expect the surface shear horizontal mode to be similarly lower than bulk transverse wave speeds reported in literature. While glass is a well-known and well-studied material where bulk wave speeds are in numerous publications, the organic LED epoxy has proprietary information withheld and does not have published wave speeds for comparison. In order to calculate the epoxy elastic constants, we need the bulk transverse wave speed in addition to the bulk longitudinal wave speed that was calculated from BLS measurements. Simulations of our glass-epoxy-glass system can help with calculating the bulk transverse wave speeds. Before looking at simulations of the more complex glass-epoxy-glass system, we can start with simulations of the glass only sample to check our model by comparing the calculated bulk transverse wave speed from the simulations to values published in literature.

5.5 Phonon Simulations

Simulations are a mathematical model that offer us incites into wave behavior on both the macro and micro-scale. Vibrational waves are seen on a macro-scale in earthquakes and on a micro-scale as phonons, so long as the wavevector is sufficiently small to be in the elastic regime, the same elastic theories apply. Most BLS work done at the micro- or nano-scale has been undertaken on thin films on a substrate that is orders of magnitude thicker than the sample film, and the substrate can be considered an infinite solid, which helps to simplify calculations. Our sample however, has

a thick piece of glass above the VTCNE in addition to the thick piece of glass below our layer of interest, which makes simulations and calculation much more difficult. The phonon dispersion relation simulations we use have origins in seismology [144–146] where early algorithms often ran into numerical precision problems that quickly overwhelmed computer memories at the time. Since then, implementation methods have varied for different scenarios. Much of the code we use is based on a delta-matrix method by Meehan [147], which includes attenuation adjustments for high frequencies similar to what the BLS measures.

Our simulations assume horizontal layers of uniform thickness where the input parameters are the bulk longitudinal wave speed (α), the bulk transverse wave speed (β), the layer thickness (t), and the material density (ρ) for each layer. Our first simulation is a single layer of glass, however, the code was not designed to work for a single layer. To continue using a single piece of glass to check the model, the glass simulations use three layers of glass where the parameters are identical for each layer except that the bulk longitudinal wave speed is increased by 1 m/s sequentially for each of the buried layers. Starting with just the glass only BLS data (Figure 5.7(a)), we can input the measured bulk longitudinal speed as well as the density of the material given by the manufacturer. By varying the thickness and bulk transverse wave speed input values, we can match the simulated surface shear horizontal wave speed with the wave speed extracted from the BLS data for a given wavevector.

The simulations in Figure 5.8 show the sign of the delta-matrix method for each velocity and wavevector combination where black is negative and white is positive, such that the roots, corresponding to a wave solution, are where the color switches from black to white or vice versa. The first (lowest) four mode solutions are highlighted with the colors blue, gold, green, and purple. The wave speeds calculated from BLS measurements are shown as horizontal lines where lime green is the bulk longitudinal wave speed, and the red lines are the surface longitudinal and surface shear horizontal wave speeds previously discussed. Figure 5.8(a) is the Rayleigh mode dispersion simulations that are also sensitive to the bulk longitudinal wave speed, as seen by the line denoting the bulk longitudinal wave speed calculated from the BLS data (lime green horizontal line) that lines

up with a slight wiggle in the simulation dispersion curves. Since we do not measure any Rayleigh waves in the glass only sample, we do not expect any other matching between the BLS measured waves and the phonon wave simulation in Figure 5.8(a). Figure 5.8(b) is the surface shear horizontal mode dispersion simulations, where we vary the input value for the bulk transverse wave speed (β) to try and match the blue labeled mode (the lowest order mode, which BLS measurements are most sensitive to) with the lower red line (the SHM wave speed calculated from the BLS data). The yellowed region of Figure 5.8 highlights wavevectors corresponding to θ angles of 15° to just below 45°. Inside the yellowed region, the blue line is quite flat, and continues to be flat past the right edge of the plots, indicating the wave speeds change very little over the range of θ that we measured. While changes to β altered the lowest order wave speeds, adjusting the thickness input t for these simulations does not alter the speed and only changes the number of modes. Additionally, the density does not have any impact for these simulations since the densities for the three glass layers are identical. The simulation dispersion results with the closest fit to the BLS data for the glass are shown in Figure 5.8 with the simulation input parameters displayed in Table 5.1.

In the phonon simulations of the glass only sample, a bulk transverse wave speed of 3240 m/s gave the closest match between the lowest simulated SHM wave speed and the SHM wave speed calculated from the BLS data using Equation (5.3). The bulk longitudinal wave speed for the glass only sample was previously calculated to be 5624 m/s, by fitting the BLS data with Equation (5.4). Both of these bulk phonon speeds in glass are consistent with other measurements in glass [148, 149], which supports the simulations model accurately representing the glass only system. Since glass is an isotropic material (the X, Y, and Z directions are identical), the wave speeds and the density from Table 5.1 can be used with Equations (2.2) and (2.4) to find the Young's modulus (C_{11}) and Shear modulus (C_{44}) for the glass in our samples.

Table 5.1: A table of the input values used for phonon simulations of the glass only sample. The bulk longitudinal wave speed (α) and bulk transverse wave speed (β) have units of meters per second. The thickness (t) has units of meters and the density (ρ) has units of grams per cubic centimeter.

layer	α (m/s)	β (m/s)	t (m)	ρ (g/cm^3)
glass1	5623	3240	1×10^{-6}	2.51
glass2	5624	3240	1×10^{-6}	2.51
glass3	5625	3240	Infinite (Inf)	2.51

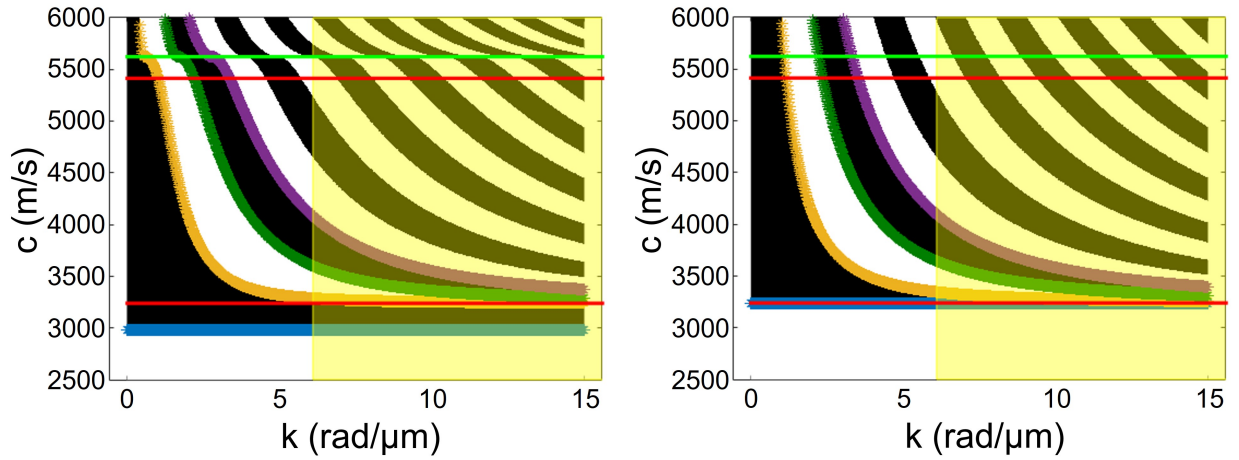

Figure 5.8: The simulations for the Rayleigh wave dispersion curves for glass are shown in (a), whereas (b) shows the surface shear horizontal mode dispersion curves for glass. The lime green horizontal line near the top is the glass bulk longitudinal speed calculated from the BLS data. This matches a slight wiggle in (a) where the "wiggle" shifts up or down with an increase or decrease to the input bulk longitudinal speed respectively. We do not expect any other matches between the BLS measurement data and the simulations in (a) since no Rayleigh wave modes were in the BLS measurements of the glass only sample. We use the lowest mode (denoted by the blue curve) in (b) or first root where the matrix values change from negative (black) to positive (white), to compare wave speeds with the SHM wave speed calculated from the BLS data (lower red line) and try to get them to match by varying the input parameters. The yellowed section is the region of k-vectors, corresponding to a sample angle of θ = 15° to just below 45°. The smallest θ used for BLS measurements in Figures 5.5 and 5.6 is 30°, which lies in the middle of the yellowed region where the simulated wave speeds change very little as the k-vector increases.

As we move on to the simulations for the glass-epoxy-glass sample, we can plug in the values from Table 5.1 for the glass layers and find the bulk transverse wave speed for epoxy using a similar method as the glass only simulations. The input parameters for the epoxy layer use the bulk longitudinal speed for epoxy, calculated from BLS measurements using Equation (5.4), the epoxy

density provided from the manufacturer, an approximate thickness based on microscope images, and an approximate bulk transverse wave speed. Analogous to the glass simulations, the input bulk transverse wave speed starts close to the (surface) SHM wave speed calculated from BLS measurements (Figure 5.7(b)) and is then varied to match the simulation Rayleigh wave speed (blue highlighted lowest order mode inFigure 5.9(a)) to the RW speed calculated from the BLS measurements (lower red horizontal line). In the glass-epoxy-glass simulations, the glass layers are both considered infinite thickness relative to the epoxy thickness. Having an infinitely thick layer as the top layer is computationally difficult, so wave speeds above the SHM wave speed are not calculated and shown as a black box. The Rayleigh wave and surface shear horizontal wave dispersion results for the glass-epoxy-glass sample are shown in Figure 5.9(a) and (b), respectively, with the simulation input parameters displayed in Table 5.2.

Table 5.2: A table of the input values used for phonon simulations of the glass-epoxy-glass sample. The bulk longitudinal wave speed (α) and bulk transverse wave speed (β) have units of meters per second. The thickness (t) has units of meters and the density (ρ) has units of grams per cubic centimeter.

layer	α (m/s)	β (m/s)	t (m)	ρ (g/cm^3)
glass	5624	3240	Infinite (Inf)	2.51
epoxy	2915	2763	5×10^{-6}	1.17
glass	5624	3240	Infinite (Inf)	2.51

In the phonon simulations of the glass-epoxy-glass sample, an epoxy bulk transverse wave speed of 2763 m/s gave the closest match between the lowest simulated RW wave speed and the RW wave speed calculated from the BLS data using Equation (5.3). The bulk longitudinal wave speed for epoxy was previously calculated to be 2915 m/s, by fitting the BLS data of the glass-epoxy-glass sample with Equation (5.4). These bulk wave speeds for epoxy are quite close together, which is highly irregular. Literature values for similar epoxies suggest both speeds fall within the longitudinal bulk speed range, but the transverse bulk speeds tend to be much lower averaging 1000 m/s [150, 151]. The difference between our bulk transverse speed and those from

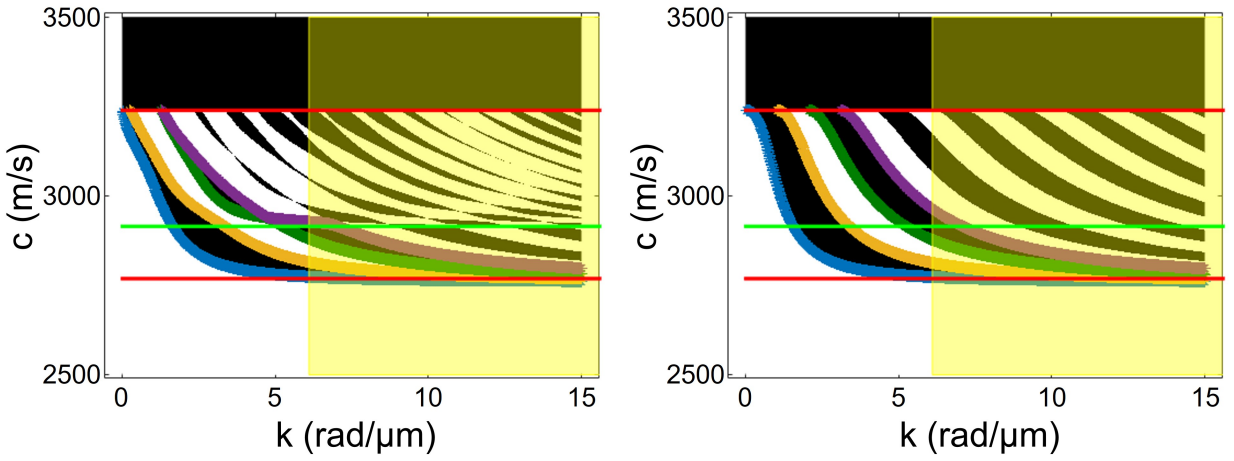

Figure 5.9: The simulations for the Rayleigh wave dispersion curves shown in (a) are for the glass-epoxy-glass sample, whereas (b) shows the surface shear horizontal dispersion curves for the glass-epoxy-glass sample. The lime green horizontal line representing the epoxy bulk longitudinal wave speed, calculated from BLS data of the glass-epoxy-glass, lines up with mode crossings in (a) where there is a change in sign (black to white and vice versa) corresponding to the epoxy bulk longitudinal wave speeds in the simulations. In (a) we use the lowest mode (first root where the matrix values change from negative (black) to positive (white)), denoted by the blue curve, to compare simulation wave speeds with the Rayleigh wave speed calculated from the BLS data (lower red line) and try to get them to match by varying the input parameters. The yellowed section is the region of k-vectors, corresponding to a sample angle of θ = 15° to just below 45°. The smallest θ used for BLS measurements in Figures 5.5 and 5.6 is 30°, which lies in the middle of the yellowed region where the simulated wave speeds change very little as the k-vector increases beyond what is shown here. To limit numerical instability and non-functioning code, for this more complex system the black space at the top is ill-defined starting at the top red line corresponding to the SHM speed calculated from the BLS data.

literature is likely due to the Rayleigh wave speed we are trying to match is not sensitive to the epoxy. While the RW is an interface wave, it is possible that the glass dominates the wave propagation and is not sensitive to the material that comprises the other half of the interface. Alternate reasons for the difference in bulk transverse speeds may be due to the resin and harder chemical compositions or an error in our simulations, though this is unlikely since the glass bulk transverse wave speed was accurately determined and we can check the sensitivity to the less well known parameters like thickness and density. A 50% change in the epoxy thickness results in a 0.5% change to the wave speeds. Additionally, the epoxy density in the simulations was also varied because the epoxy mix may be different from sample to sample, with the result that a even a non-realistic den-

sity change of 50%, would only result in a 0.005% change to the phonon wave speeds. Effectively the epoxy density and thickness have little impact on the phonon speeds of the simulations.

5.6 Ongoing Work and Future Directions

The above work has used Brillouin light scattering measurements and phonon simulations to determine the bulk wave speeds for the encapsulation materials (glass and epoxy), which can then be used to calculate elastic constants or the elastic moduli for the materials as outlined in Section 2.1. In addition to the encapsulation materials elastic constants it is also critical to have accurate elastic constants for the VTCNE film. Using density functional theory (DFT) calculations, our collaborators at the University of Iowa produced the elastic constants for the VTCNE in Table 5.3. The VTCNE film structure has all four of the equitorial (XY plane) nitrogen atoms

Table 5.3: A table of VTCNE elastic moduli calculated by density-functional theory (DFT) for a in-plane isotropic sample where the out-of-plane direction (z) had a different structure compared to in-plane. Values have units of kBar.

Direction	XX	YY	ZZ	XY	YZ	ZX
XX	664.37	378.56	79.59	13.82	-2.01	5.27
YY	378.36	546.82	37.90	0.87	-15.48	-3.67
ZZ	79.59	37.90	586.44	-6.94	7.58	3.13
XY	13.82	0.87	-6.94	351.65	2.51	-9.51
YZ	-2.01	-15.48	7.58	2.51	66.53	-1.73
ZX	5.27	-3.67	3.13	-9.51	-1.73	99.36

of the TCNE molecule bonded to vanadium atoms, however there are two nitrogen atoms of the TCNE molecule along the Z axis that are not bonded to vanadium atoms. This molecular bonding structure indicates the VTCNE film is a transverse isotropic material, so Table 5.3 can be compared to the transverse isotropic elastic tensor from Section 2.1. By taking the average of the C_{11} values from Table 5.3 and the value for the VTCNE density from Table 5.4, converting them to units of N/m^2 and kg/m^3, respectively, and plugging them into Equation (2.2), we calculate a bulk

longitudinal phonon speed for VTCNE of 7624 m/s. Following a similar procedure, we can use the density again from Table 5.3 and C_{66} (XY) value, and plug them into Equation (2.3) to calculate a bulk transverse phonon speed for VTCNE of 5809 m/s. These wave speeds calculated for VTCNE are higher than glass and would suggest that VTCNE more rigid than glass, though the ability to grow VTCNE on flexible substrates [130] would indicate this is actually a soft and flexible substance like rubber or chewing gum. Another possibility for the high wave speeds besides the elastic moduli is the density 1.04 g/cm^3. This density value was obtained by the Flatté group using DFT calculations, and is similar to the lower end of density values (1.0-1.5 g/cm^3) found literature [152], suggesting the density is not the likely reason for calculation such high wave speeds for VTCNE. BLS measurements show no θ independent signals that would correspond to VTCNE bulk longitudinal modes between |5| GHz and |45| GHz. With the bulk longitudinal speed of VTCNE calculated to be 7624 m/s, we might expect to see a signal in the BLS spectra for an index of refraction between n = 0.2 and 1.7, though VTCNE is an opaque material, which complicates the index of refraction value and may not allow us to directly measure bulk phonons. However, we would still expect to see surface(interface) wave signals. Since surface waves should be observable, we can add a VTCNE layer to the previous simulations, plug in the VTCNE bulk phonon speeds determined from the DFT calculations, and use the simulations to approximate the frequencies we would expect for VTCNE surface waves. The input values used for the simulations with the VTCNE layer are in Table 5.4 with the corresponding dispersion curves in Figure 5.10.

Table 5.4: A table of the input values used for phonon simulations of the glass- VTCNE-epoxy-glass sample. The bulk longitudinal wave speed (α) and bulk transverse wave speed (β) have units of meters per second. The thickness (t) has units of meters and the density (ρ) has units of grams per cubic centimeter.

layer	α (m/s)	β (m/s)	t (m)	ρ (g/cm^3)
glass	5624	3240	Infinite (Inf)	2.51
VTCNE	7624	5809	2×10^{-6}	1.04
epoxy	2915	2763	5×10^{-6}	1.17
glass	5624	3240	Infinite (Inf)	2.51

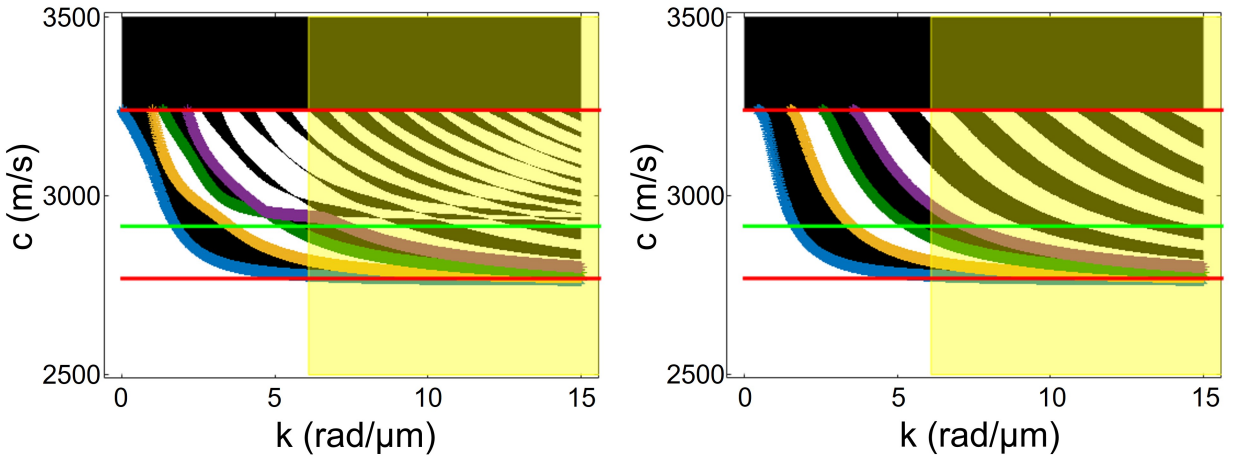

Figure 5.10: (a) shows the Rayleigh and surface longitudinal dispersion curves for glass-VTCNE-epoxy-glass, whereas (b) shows the surface shear dispersion curves for glass-VTCNE-epoxy-glass. Very similar to glass-epoxy-glass in Figure 5.9. The yellowed section is the region of k-vectors corresponding to a sample angle of θ = 15° to just below 45°.

Adding the VTCNE layer to the simulation, shown in Figure 5.10, changes the wave speed of the lowest order mode, for both the Rayleigh and shear horizontal modes by 3 m/s for a sample at an angle θ = 30°, with visible but minor changes to the higher order modes of the dispersion curves. This indicates that to be sensitive to the VTCNE we will need a new sample design.

To be more sensitive to the VTCNE elastic parameters via phonon measurements using Brillouin light scattering, we have designed new samples with a thin film of VTCNE (∼100 nm) on top of a Si_3N_4 membrane. This design should help increase the relative VTCNE signal by reducing the "window" thickness from 100 μm of glass to 100 nm of Si_3N_4. This will require a characterization of the phonon speeds in Si_3N_4, but should also allow for measurements of modes that are quantized across the thickness of the sample, shifting the VTCNE phonon modes to higher frequencies as the Si_3N_4 window decreases in thickness. A similar sample design using soft polymethyl methacrylate (PMMA) thin films on Si_3N_4 membranes has been successfully used to probe modes using BLS [153]. Additionally, this design should help better identify what modes correspond to which material or interface.

Additional calculations by the Flatté group at the University of Iowa show that the magneto-optical signal of VTCNE is weak, making thermal magnons difficult to detect using BLS methods. To address this, another sample design using an indicator material with a strong magneto-optical signal is also in progress where the indicator material can couple to the VTCNE magnons and still allow for BLS thermal magnon measurements.

5.7 Summary

Since initial reports show that VTCNE is magnetostrictive and therefore sensitive to strain in its environment, characterization of the elastic properties of the encapsulation materials is critical for VTCNE devices used in materials research and commercial applications. This work has realized the characterization of the glass-epoxy-glass environment using Brillouin light scattering to identify the phonon modes and extract their speeds. Using simulations of surface wave dispersion relations from seismology, adapted to our sample, we were also able to extract the bulk transverse wave speed, which together with the bulk longitudinal wave speed allows for the calculation of the elastic constants. Further measurements are in progress on samples that have been re-designed to obtain better sensitivity to both VTCNE phonons and thermal magnons.

Chapter 6

Spin wave up conversion of K-vectors in Y structures

6.1 Context

This chapter consists of the paper *Spin wave wavevector up-conversion in Y-shaped Permalloy structures*, which was published in Applied Physics Letters in 2021.[1] Supplemental materials for this paper can be found in Appendix A.

Contributions

The samples were designed by Jason Liu, Aron Guerrero, and Kristen Buchanan. Aron Guerrero implemented the photolithography while Mitchell Swyt carried out the sputter deposition. Jason Liu and I collected the micro-BLS measurements. Simulations and animations were performed by Kristen Buchanan. All authors contributed to and reviewed the manuscript. Justin Dickovick helped with fabricating sample holders. The authors also recognize support for A. G. provided by the McNair Scholars Program at Georgia Southern University.

6.2 Paper Overview

Spin waves in micrometer-sized, patterned Y-shaped Permalloy structures were studied using micro-focus Brillouin light scattering (BLS) with a magnetic field applied in-plane. For in-plane magnetized thin films and microstrips, the dispersion relations depend on the angle of the magnetization with respect to the microstrip axis. BLS measurements show that spin waves generated in the two arms that form the top of the Y structure can be channeled into a longer magnetic microstrip that forms the base when the applied field is oriented perpendicular to the long axis of the base. In this configuration, the base supports surface spin waves. A comparison of the BLS data

[1]Reproduced here with the permission of AIP Publishing. H. J. Jason Liu, Aron Guerrero, Katherine E. Nygren, Mitchell Swyt, and Kristen S. Buchanan. *Appl. Phys. Lett.* **119**, 172403 (2021).

with micromagnetic simulations reveals that low-k spin waves generated by a microstrip antenna in the arms are converted to higher-k spin waves in the base, which may be useful for nanomagnonic applications.

6.3 Research Article

Spin waves, also known as magnons, are propagating magnetic excitations that can be used to transmit information and carry out logic operations [154, 155]. The past decade has seen an increase in research on magnonic devices [156,157]. These devices are ideal for microwave circuits and device miniaturization because spin waves span the gigahertz regime with wavelengths on the order of micrometers. A variety of devices have been proposed including spin wave-based logic devices that leverage interference effects [158–166]. For any such devices, understanding how spin waves come together at a junction is important, and strategies for efficiently generating spin waves, especially short-wavelength/high-wavevector k spin waves, are needed to move devices into the nanoscale regime.

Oersted fields from microstrip antennas are commonly used to create spin waves. Antennas do not, however, scale favorably. The largest k that can be practically generated by an antenna is $k_{\text{max}} \sim \pi/w_{\text{an}}$, where w_{an} the antenna width, and since the antenna resistance is also proportional to $1/w_{\text{an}}$, heating becomes a significant issue for nanoscale antennas [167]. Magnetic gratings [168] and parametric pumping [169] have been employed to obtain large-k spin waves; however, the former method relies on the use of a second material that must be carefully chosen to obtain a grating resonance frequency that matches the frequency of the desired k in the device, and the latter requires high microwave powers. Another approach to obtain high-k spin waves that avoids these complications is to exploit the characteristics of the dispersion relations for magnetic microstrips. For example, the dispersion relations of a magnetic microstrip are sensitive to geometric confinement [170], and studies done on tapered waveguides show that the k of a traveling spin wave will increase as the waveguide width is reduced [171]. The dispersion relations for in-plane magnetized thin films and microstrips also differ depending on the angle between the static magnetization $\overrightarrow{M}_0$

and $\overrightarrow{k}$ due to the internal demagnetization fields [25], and, as will be shown, this also provides opportunities to manipulate k.

In this work, Brillouin light scattering (BLS) measurements done on a Y-shaped magnetic structure shows that channeling spin waves through a transition in the spin wave dispersion environment provides a means to obtain higher-k spin waves. Spin wave propagation studies are often done in the magnetostatic surface wave or Damon Eshbach (DE) configuration with $\overrightarrow{M}_0 \perp \overrightarrow{k}$. In fact, a method to maintain this configuration through curved waveguides to allow surface spin waves to travel around bends has been demonstrated [172, 173], and the changing dispersion environment can be used to selectively permit or block the passage of spin waves through branches of a Y-shaped structure [173]. Here, measurements and simulations are conducted that demonstrate that Y structures also offer opportunities to increase k, since low-k spin waves generated in the arms of the Y will convert to higher-k surface spin waves in the DE-magnetized base.

Spin wave propagation was studied in a 40-nm thick $Ni_{80}Fe_{20}$ (Permalloy) Y-shaped structure made up of microstrips with widths of w = 2.7 μm, illustrated in Figure 6.1(a). Throughout the work presented here, the Y structure is rotated by 90° counterclockwise, and the two arms that form the top of the letter "Y" are referred to as the top and bottom arms based on their locations after rotation. The top and bottom arms are at angles of -45° and +45° with respect to the x-direction, respectively, and the arms merge into the base of the Y that extends along the x-direction at a distance of x_0 =1.75 μm. All distances x are measured from the edge of the antenna. A 300-nm thick, 10- μm wide gold microstrip antenna, separated from the Permalloy structure by a 100-nm thick SiO_2 insulating layer, was used to excite spin waves. An external magnetic field of $\mu_0 H$ = 60 mT was applied in the +y-direction, and spin waves were detected with micro-focus BLS [76, 85, 174]. An objective (magnification = 100 $\times$ and numerical aperture = 0.75) is used to focus a laser (wavelength of 532 nm) on the structure with a spatial resolution of approximately 300 nm, and the BLS signal is obtained by analyzing the 180° backscattered light using a six-pass tandem Fabry–Pérot interferometer. The BLS signal was monitored as a function of the microwave frequency f supplied to the antenna to excite spin waves in the top and bottom arms, and the sample

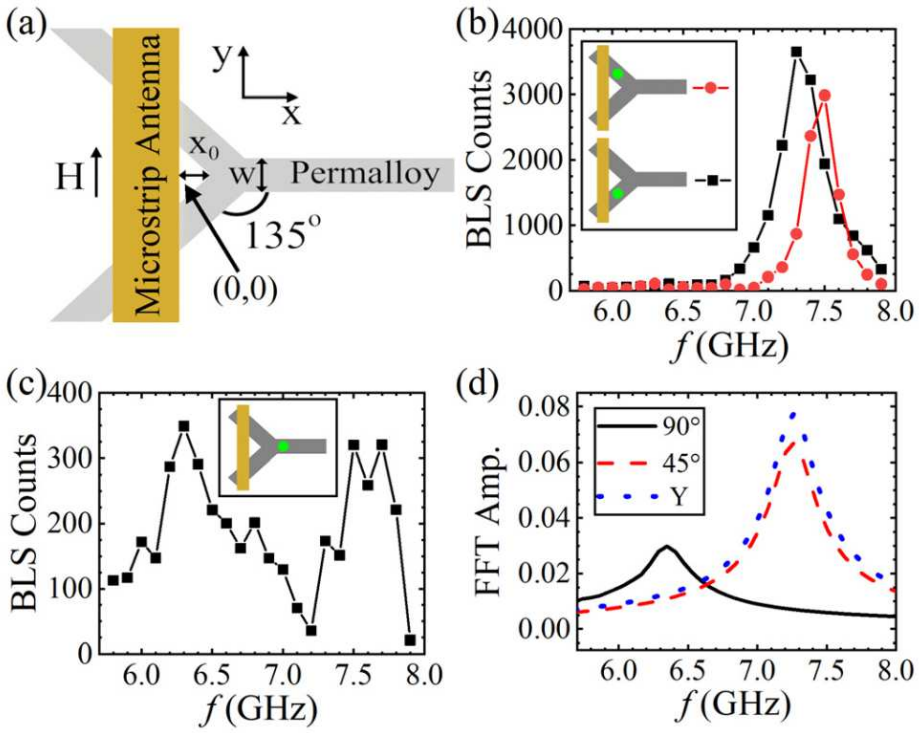

Figure 6.1: (a) Illustration of the sample and measurement setup. The Oersted field generated by the gold microstrip antenna was used to excite spin waves in the Permalloy Y-shaped structure, and the dynamic response of the structure was probed by BLS using a focused laser spot. (b) Normalized BLS counts as a function of f measured at a distance of x = 1 μm from the edge of the antenna in the top and bottom arms of the Y structure, and (c) at the vertical center of the base of the Y at x = 5 μm, just to the right of where the base begins. The lines connecting the data points are provided to guide the eye. (d) Simulations of the amplitude vs frequency response for a straight microstrip with H at 90° and 45° (90° and 45° cases), and for the Y structure (Y case).

position was scanned with respect to the BLS probe laser to obtain two-dimensional spatial maps of the spin wave intensities.

Micromagnetic simulations were conducted using MuMax3 [175] and compared to the experimental results. Simulations were done with a static magnetic field of $\mu_0 H$ = 60 mT for three cases: a long, straight 40-nm thick and 2.7- μm wide Permalloy microstrip with H applied in-plane and at 90° and 45° to the long axis of the microstrip, and a Y-shaped structure with the same dimensions as the sample. These geometries will be referred to as the 90°, 45°, and Y cases, respectively. Material parameters appropriate for Permalloy were used: saturation magnetization $M_s = 8 \times 10^5$ A/m, exchange $A_{\text{ex}} = 1.3 \times 10^{-11}$ J/m, a damping parameter of α = 0.01, and anisotropy was neglected. Dynamic magnetic fields were applied in-plane and perpendicular to the antenna axis within a

2- μm wide region; the antenna width was reduced to 100 nm to obtain spin wave dispersion relations. For the straight microstrip (90° and 45° cases), the antenna axis is set parallel to H, while for the Y-structure, the antenna is oriented as shown in Figure 6.1(a), and simulations were performed with H along y and misaligned by an angle of -3° [i.e., $H_x = -H\sin(3°)$]. Cells of $21 \times 21 \times 40$ nm^3 were used. This is small compared to the wavelengths of interest, and selected simulations repeated with half-sized cells yield the same results. A broadband sinc pulse was used to obtain the amplitude response as a function of frequency and spin wave dispersion relations. To understand the spin wave excitation patterns, simulations using a sinusoidal excitation field at the frequency of the peak response amplitude were also done, and spin wave mode maps were obtained by analyzing the magnetization over one period after a steady state response was reached (after 50 periods).

Figure 6.1(b) shows BLS measurements as a function of f obtained at x = 1 μm on each arm of the Y structure, and Figure 6.1(c) shows the corresponding data set obtained in the base of the Y at x = 5 μm at the midpoint of the microstrip (y = 0). The BLS counts in Figures 6.1(b) and (c) are integrated counts over frequencies near f minus the corresponding integrated background counts obtained with the driving frequency turned off, also normalized by a reference signal. A single peak is observed for each of the top and bottom arms [Figure 6.1(b)] at 7.47 ± 0.05 and 7.34 ± 0.05 GHz, respectively. The signal in the base of the Y, in contrast, shows two broad peaks: a lower frequency peak that is centered at 6.37 ± 0.05 GHz and a higher frequency peak that extends from 7.3 to 7.8 GHz and overlaps with the signals observed in the arms.

Figure 6.1(d) shows micromagnetic simulations for the considered cases (90°, 45°, and Y) where the amplitudes of the Fourier transform of the z-component of the magnetic responses are shown as a function of f. Single peaks are observed for each case. The peaks for the 45° and Y cases are both at f = 7.25 GHz, which is close to the peaks observed in the arms [Figure 6.1(b)] and the higher frequency peak observed in the base [Figure 6.1(c)]. The peak for the 90° case is at 6.35 GHz, which overlaps with the lower frequency peak observed in Figure 6.1(c). This suggests that the lower frequency peak in Figure 6.1(c) is due to spin waves that are excited in the base

of the Y by the long-range Oersted fields of the antenna. Notably, the higher frequency peak in Figure 6.1(c) (7.3–7.8 GHz) is absent for the 90° case but present for the Y case; hence, the high frequency peak in Figure 6.1(c) is due to spin waves that have traveled into the base from the arms.

The peak frequencies observed for the top and bottom arms [Figure 6.1(b)] are slightly different. Additional simulations show that a 200 nm variation in w, the experimental uncertainty in w, leads to a 0.03 GHz frequency difference, while a misalignment of H by $\pm 3°$, the experimental uncertainty, leads to a shift of 0.09 GHz as well as a change in the amplitude that is comparable to what is observed experimentally. Therefore, a misalignment of H by $\sim 3°$ is likely the cause of the differences in the signals between the two arms.

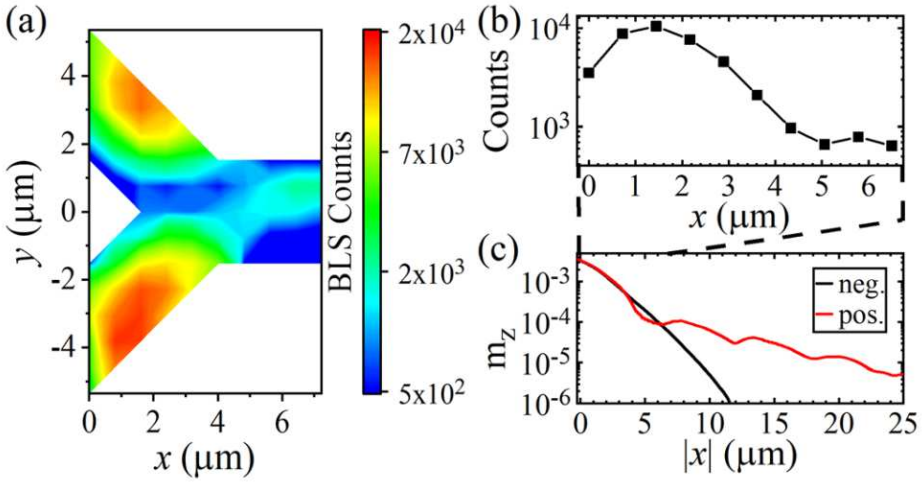

Figure 6.2: (a) Two-dimensional spatial BLS scan showing spin wave propagation in the Y structure for $f = 7.40$ GHz. (b) BLS counts from (a) integrated over y and shown as a function of x. The lines connecting the data points are provided to guide the eye. (c) The amplitude response integrated over y for simulations of the mode at $f = 7.25$ GHz, the peak frequency in Figure 6.1(d). The responses are shown for the positive direction (pos.) that matches the experiment and for the negative direction (neg.) that corresponds to a continuation of the arms [see Figure 6.1(a)].

Figure 6.2(a) shows a two-dimensional spatial BLS scan of the Y-structure taken at $f = 7.40$ GHz, a frequency between the peaks of the two arms [Figure 6.1(b)]. Strong spin wave signals are observed in the arms that proceed past the junction, confirming that the signals generated in the arms propagate into the base. Although the spin wave intensities decrease with increasing x [Figure 6.2(b)], the signal is above background out to the farthest measured distance ($x = 7\,\mu$m). Simu-

lations of the spin wave amplitudes [Figure 6.2(c)] show that the spin waves propagate considerably farther to the right, the direction that includes the junction and base (positive x), as compared to the left, where the microstrips continue at 45° with respect to H (negative x). The signal vs +x shows periodic decreases in intensity in the base at intervals of approximately 6 μm due to interference of width-quantized spin wave modes [176], and a dip in the experimental signal is observed at a similar distance as compared to the first dip in the simulations (x = 5 μm).

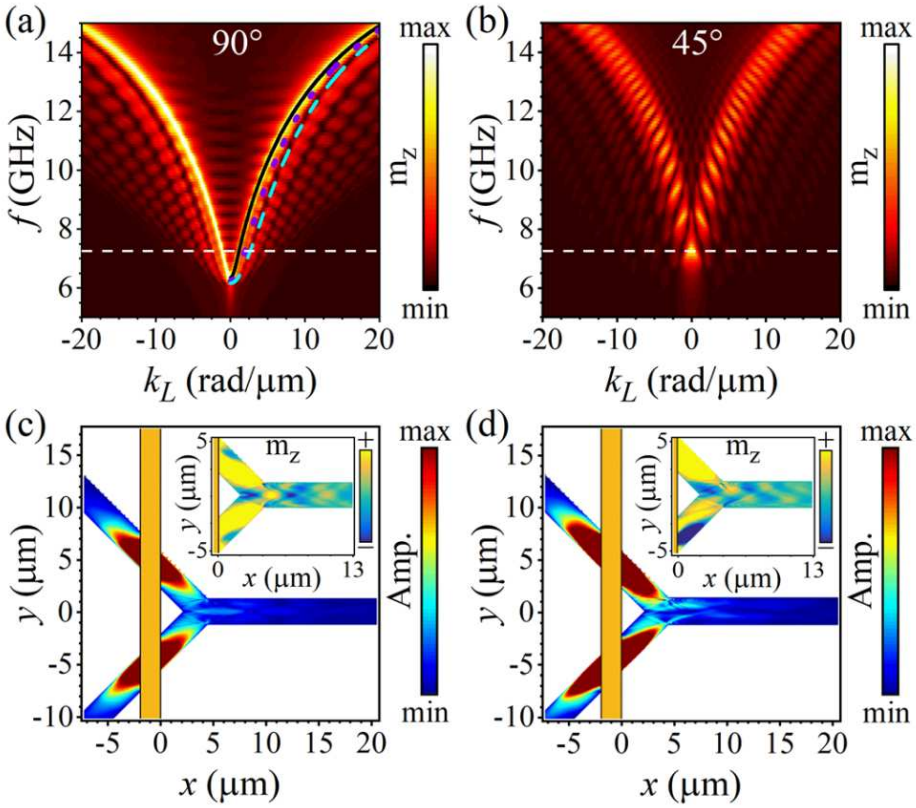

Figure 6.3: Spin wave dispersion curves obtained using micromagnetic simulations are shown for the (a) 90°and (b) 45° cases. Analytical calculations of the spin wave dispersion relations for the three lowest-order, odd, width-quantized modes are superimposed in (a) for $k_L > 0$ (black straight, purple dotted, and blue dashed are for modes n = 1, 3, and 5, respectively), and horizontal dashed lines at f = 7.25 GHz are shown in (a) and (b). Spin wave amplitude maps at f = 7.25 GHz for the Y case are shown in (c) and (d) with H applied along the antenna and at an angle of -3° with respect to the antenna, respectively. The insets show corresponding snapshots of m_z at an instant in time.

Spin wave dispersion relations were calculated using micromagnetic simulations for the 90° and 45° cases [Figures 6.3(a) and 6.3(b), respectively]. The width of the antenna region was re-

duced to 100 nm to obtain a broader range of excited k_L, where k_L is the wavevector parallel to the microstrip axis, and dispersion relations were obtained by taking two-dimensional Fourier transforms of the out-of-plane component of the magnetization m_z vs k and time. The spin wave dispersion relations in Figure 6.3 show the available states at a given frequency as well as the relative excitation amplitudes of the allowed modes. The strongest responses in Figures 6.3(a) and 6.3(b) are the lowest-order width-quantized modes, and the weaker responses are higher-order (odd only) width-quantized modes. For the 90° case [Figure 6.3(a), the DE geometry], continuous dispersion relations are obtained, which agree with analytical calculations that assume quantization of the wavevectors along w [25, 176]. The analytical theories that have been developed for microstrips are for high symmetry field directions, so Figure 6.3(b) only includes micromagnetic simulations.

Unlike the 90° case, the dispersion relations for the 45° case [Figure 6.3(b)] are made up of sets of disconnected sections, which suggests that there are additional quantization effects. As shown in Figure A.1 (Multimedia view) in the supplementary material, the spin wave modes have backward volume characteristics, which is consistent with the slopes (negative for $k_L > 0$ and positive for $k_L < 0$) of the bright sections that makeup the lowest-order dispersion relation. The frequency of the strongest peaks in Figure 6.1(d) [f = 7.25 GHz, white dashed lines in Figures 6.3(a) and 6.3(b)] corresponds to $k_L \sim 0$ for the 45° case and $k_L = 1.1$ rad/ μm for the 90° case; hence, spin waves excited at the peak frequency of the 45°-oriented arms must shift to higher k_L in order to propagate past the junction of the Y. The dispersion curves in Figure 6.3 suggest that increasing f will lead to similar upconversion in k_L and consequently a larger k_L in the base. Analytical calculations presented in the supplementary material show that upconversion magnitudes of >70 rad/ μm are expected for smaller w.

Simulations of the spin wave modes at f = 7.25 GHz were done to further understand the mode conversion process in the Y structures. Figures 6.3(c) and 6.3(d) show amplitude maps of the modes and corresponding snapshots of m_z at a fixed time for H along the antenna and misaligned by -3°, respectively. The dark/bright/dark contrast across the microstrip width in the inset of Fig-

ure 6.3(c), e.g., at x = 5 μm, and the bumps observed in Figure 6.2(c) are due to interference of two odd width-quantized modes (n = 1 and 3) beyond the junction. The central bright area has a larger magnitude than the dark areas at x =5 μm due to constructive interference in the center of the microstrip [also seen in Figures A.2 and A.3 (Multimedia view) in the supplementary material]. The approximate k_L obtained from analysis of the inset to Figure 6.3(c) is 2.1 rad/ μm, which matches the k_L for the n = 3 mode in the dispersion relation [Figure 6.3(a)].

The amplitude vs frequency response suggests that experimentally H is slightly misaligned by -3°, and Figure 6.3(d) shows that the misalignment of H leads to a slight difference in excitation amplitudes in the two arms, which is consistent with experimental results [Figure 6.2(a)]. The experimental data in Figure 6.2(a) demonstrate that the generated spin waves continue into the base, which is consistent with the simulations; however, it is difficult to compare the excitation patterns directly in this region due to the limited scan range in the experiment. Interestingly, Figure 6.3(d) [and Figure A.3 (Multimedia view) in the supplementary material] shows an even n = 2 width-quantized excitation, a mode that is not directly excited by an antenna, which suggests that the field angle can provide a means to control the dominant mode.

The Y structures may offer excitation efficiency advantages over direct excitation by an antenna. In Figure 6.1(d), the peak amplitudes for the 45° case are more than a factor of two higher as compared to the 90° case. These simulations have the same excitation field and microstrip length, so this amplitude difference reflects a difference in the excitation efficiencies. (The Y structure simulations cover a larger area, so the amplitude cannot be directly compared to the other cases.) The excitation efficiency for spin waves is lower in the magnetostatic backward volume wave configuration (H at 0°) as compared to the DE configuration (H at 90°) [58, 177] in the absence of a change in the antenna orientation. Here, the torque is larger for the 45° case because the antenna is tilted, but the excitation area is increased by less than a factor of two over the 90° case; hence, additional quantization effects may also contribute to the increased amplitude for the 45° case, as suggested by the dispersion relation [Figure 6.3(b)].

In summary, micro-focus BLS measurements and micromagnetic simulations show that spin waves excited in the arms of a Y-shaped Permalloy structure will converge and continue past the junction, where measurable signals were detected out to x = 7 μm. The spin waves can propagate past the junction because states are available at the excitation frequency in both the arms and the base of the Y, and furthermore, since the states in the base have a larger k as compared to the antenna-excited spin waves in the arms, the spin waves undergo up-conversion of k. The results further suggest that the antenna-based excitation efficiency for spin waves in the arms of the Y structure is larger than for the DE geometry, likely due to confinement effects, and mode selection is also possible through small changes to the angle of H. Spin wave dispersion calculations suggest that it should be possible to reach wavevectors of greater than 70 rad/ μm; hence, these results have important implications for the development of nanomagnonic devices.

6.4 Summary and Future Directions

This work has used micro-focused BLS measurements and micromagnetic simulations to demonstrate the use of an in plane magnetic field and a Y-shaped Permalloy structure to convert low-k spin waves excited in the arms of a Y-shaped structure, to a higher-k as the spin waves propagate into the base of the Y-structure.

Future directions for this project could include further investigation into the excitation efficiency between the excitation of spin waves in a microstrip directly in the Damon-Eshbach geometry or indirectly by channeling the spin waves excited in the arms of the Y-structure into the DE geometry in base of the Y.

Chapter 7

Other Projects

7.1 Yttrium Iron Garnet Confinement and Traveling Waves

As discussed in Chapter 6, the confinement of spin waves through a structure's geometry leads to quantization and altered dispersion curves. A thin film will develop quantized thickness modes and a microstrip will develop quantization across its narrowest dimension(s), when the confined directions are on the order of the spin wave wavelength.

While there are many studies of spin waves in magnetic microstrips of uniform thickness [58, 59, 75, 83, 178], we used a raised 5 μm strip of YIG on top of a much wider (500, 200, 100, or 50 μm) bar of YIG. This raised rib structure creates a confinement for not only spin wave modes but also photonic modes, in the entire thickness of YIG below the rib, but still laterally confined to the 5 μm width of the rib. Our contribution to this project was to study and map the spin wave modes in the confined strip with the micro-BLS, which could then be compared with spin wave simulations and simulations with magnon-photon coupling in the raised rib. This project was carried out in collaboration with Hong Tang's group at Yale University who designed and fabricated the sample and excitation resonator and performed the simulations.

Here, the YIG bar (on a GGG substrate with an SiO_2 capping layer) sits on a half-lambda resonator above a stack of magnets producing an out of plane field in the YIG. The half-lambda resonator has a short microstrip adjacent to the microwave signal line, such that the length of the short strip is equal to half the wavelength (or half wavelength multiple) that efficiently couples across the gap between the two lines. The magnetic resonance frequency in the YIG needs to match the resonant frequency of the half lambda resonator for the most efficient spin wave excitation. The first part of this alignment was done visually with an optical microscope, as seen in Figure 7.1, where the width of the 500 μm YIG strip is placed directly above the copper resonator for the full length of the strip.

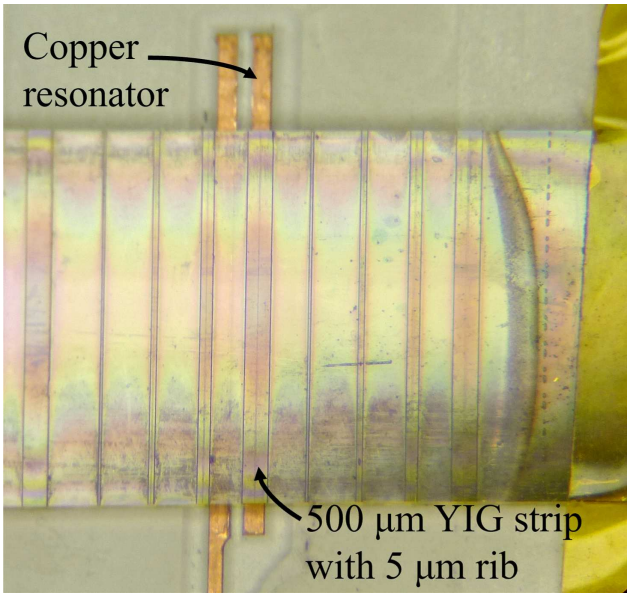

Figure 7.1: Diagram showing the 500 μm YIG strip aligned with the copper resonator. The YIG strip is roughly 5 mm long (from one edge of the sample to the other) with the 5 μm rib seen as a faint line in the center of the YIG strips. There are other YIG strips to the left of the resonator with the same confinement rib but with widths of 200, 100 and 50 μm (right to left).

Once visually aligned, the half lambda antenna was connected to one port of a calibrated vector network analyzer (VNA) to look at the energy absorbed by the antenna and the YIG. As seen in Figure 7.2(a) the wide excitation from the half lambda resonator lies around 7.16 GHz, with the narrow resonance of the YIG at a slightly higher frequency of 7.23 GHz. The YIG resonance frequency can be adjusted to match the frequency of the half lambda resonator by changing the vertical position of the permanent magnets below the sample. Decreasing the vertical position of the magnets will reduce the magnitude of the magnetic field at the sample such that the resonance frequencies match at 7.16 GHz, as seen in Figure 7.2(b). To achieve a YIG resonance at 7.16 GHz, the sample needs to be in an out-of-plane magnetic field of approximately 3011 Oe.

After the resonances are aligned, the sample holder was placed on the micro-BLS stages and the antenna was connected to the RF generator. While raising the sample stages to the laser and camera focus for the micro-BLS, the stages continually crashed and lost their positioning ability. The stages disengaged because the forces between the magnets in the sample holder and the pole pieces of our in-plane magnet were larger than the lateral forces the stages could take. Since the in-

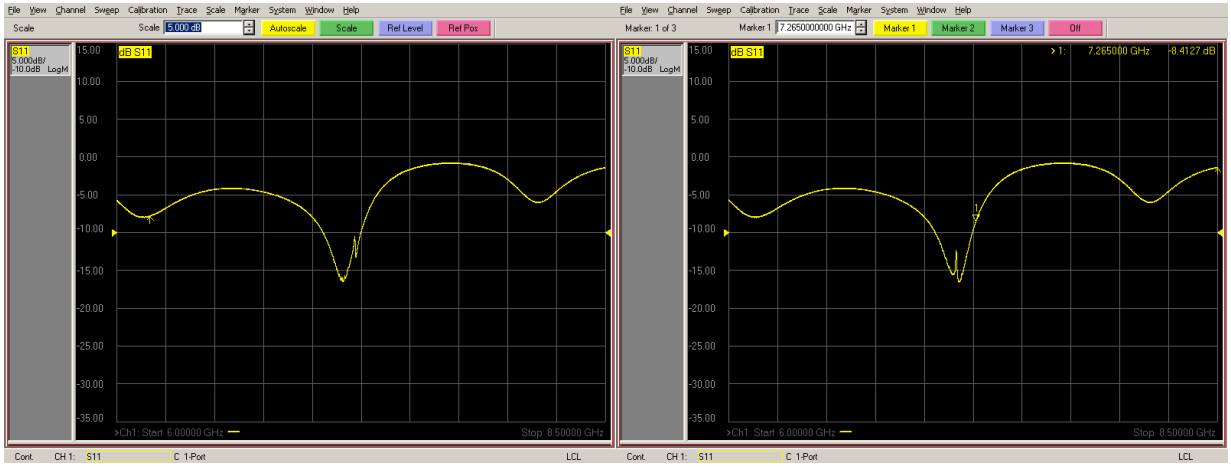

(a) VNA Unaligned Resonances in YIG **(b)** VNA Aligned Resonances in YIG.

Figure 7.2: (a) shows a broad resonance, around 7.16 GHz, of the half lambda resonator with a narrower resonance of the YIG at a slightly higher frequency of 7.23 GHz. (b) shows the two resonances lined up at the same central frequency of 7.16 GHz.

plane magnet was not needed for these measurements, the magnet was removed from the vicinity of the sample stages to prevent further crashing. While looking with the micro-BLS camera after raising the stages to the focus, we were able to identify the edges of the 500 μm YIG strip however the sample surface was not pristine and I could not locate the 5 μm rib near the center. The edges of the 500 μm YIG strip edges were visible on the camera, but even using the stage position to find the exact center where the 5 μm rib should be did not reveal clear rib edges. BLS scans across where we expected the rib to be revealed no signal at the expected frequency where the resonances overlapped despite a strong signal with the VNA. An increase in RF made no change to the lack of micro-BLS signal. To obtain a micro-BLS signal the sample will likely need to remade with the following material considerations. YIG has a low optical scattering cross-section at 532 nm so a different magnetic material (either as a thin film over the whole sample or patterned squares directly over the rib) that is highly reflective may help in obtaining a micro-BLS signal instead of using YIG [179]. Alternatively, but more difficult to implement, the 532 nm BLS laser could be swapped out for a lower wavelength where YIG has a higher BLS signal [180, 181]. Another option would be a thin non-oxidizing metallic layer with a large skin depth instead of the SiO_2 where the spin wave in YIG could be seen through the capping layer. Forward scattering is not

an option due to spatial resolution limits of the laser spot (30 μm) and the width of the rib (5 μm). The height of the rib above the rest of the bar is less than 1 μm and the edges are slightly tapered, which may result in no clear edge through the micro-BLS camera so a sharp sidewall profile or a greater aspect ratio may be visible on camera.

7.2 Vanadium Oxide Spin Waves

Metals and insulators are separate material classes and are therefore generally thought of as two completely separate materials. However vanadium oxide (VO_2), has a metal-insulator transition (MIT) a little higher than room temperature, around 340 K [182–184]. Above the transition temperature, VO_2 is metallic in a rutile (tetragonal) phase, but below the transition temperature in the insulating phase, it exhibits a monoclinic structural phase [182, 185]. As discussed in Chapter 4, nickel is magnetostrictive and therefore sensitive to any strain or stress caused by the changing lattice parameter of the different structural phases of VO_2. These strains will then change the anisotropy of the nickel film, which raises the question of how the spin wave dispersion relations behave around this structural transition. This project aimed to study a 10 nm nickel/ 100 nm VO_2 bilayer capped with 3 nm aluminum, as the VO_2 goes through the MIT by using BLS to measure thermal magnons in the nickel. The BLS measurements would give us insight into changes in the dispersion relations as well as any anisotropy variations for the nickel. The bilayer samples were fabricated by Ivan Shuller's group at the University of California, San Diego.

Figure 7.3: Antennas made for VO_2 sample excitation. Iterations 1, 2, and 3 (left to right).

BLS measurements were made with both the conventional 180° back scattering and micro-focus set-ups but no thermal magnons were seen. At this point, we started looking at whether a waveguide could excite the sample with a strong enough signal, a wide range of k-vectors, and a large area excitation to help ensure the BLS laser is above the waveguide when measurements are taken. Shorted coplanar waveguide antennas were fabricated using an optical photolithography technique in Stuart Field's lab here at CSU, and went through three iterations (seen in Figure 7.3) to optimize the antenna width and also for an impedance match to the microwave generator. The final iteration of antenna resulted in a small signal on the VNA, however this would not be enough to be seen above noise with the BLS. Another option that was considered was a cavity with an optical hole for the BLS, but this severely limited the wavevectors that could be measured with BLS, so this was not tried. We concluded that the aluminum capping layer was likely causing the lack of BLS signal and that for future measurements we would need a new sample, either with a tantalum capping layer instead of aluminum or an antenna patterned on top of the capping layer to be within closer proximity to the magnetic bi-layer for a more efficient excitation.

7.3 Dzyaloshinskii-Moriya Interaction Measurements

Skyrmions have recently been studied for possible computer memory applications, with an interest in "race track" memory and magnonic logic circuits [186–189]. These applications require stable skyrmions that can also travel along a wire. Skyrmions are topologically protected structures, and their formation and stabilization are largely dependent on the Dzyaloshinskii-Moriya interaction (sometimes DM interaction or DMI) of the sample. The Dzyaloshinskii-Moriya interaction can also lead to nonreciprocal spin waves in saturated films, where there is a preferred direction to the spin wave propagation. The DMI for a sample is fairly complex with contributions from both the bulk of the materials the interfaces between layers [190–193]. While domain wall expansion measurements with MOKE can give an idea for the interfacial DMI value, BLS is a far more direct method to do the same [79, 80, 194–196]. By understanding the conditions that give

stable skyrmions and measuring the interfacial DMI, we can better understand skyrmions and their motion for use in future applications.

This was the lab's first attempt at using BLS to measure and extract the interfacial Dzyaloshinskii-Moriya interaction (DMI) value, in gadolinium cobalt (GdCo) alloyed samples sandwiched between iridium and platinum, where the heavy metal-ferrimagnet-heavy metal trilayer was then repeated between 8 and 20 times. This used a conventional BLS 180° back scattering set up with an angle mount for k-vector selectivity. The nonreciprocity of spin waves is often shown by a shift in the dispersion curves along k corresponding to the external magnetic field direction. For the same field magnitude (but opposite directions), and for the same magnitude k-vectors (again, opposite directions but on the same surface), there will be a difference in frequencies of the surface spin waves due to interfacial DMI, whereas a sample with no interfacial DMI would not see any frequency shift. Since the interfacial DMI value can be positive or negative, the directions of the field and waves may be different with respect to each other for different samples. Exploiting the frequency difference for opposite fields, would allow for a calculation of the magnitude of the interfacial DMI value, and by measuring at different angles (different k-vectors), we could also map out the shifted dispersion curves.

The GdCo alloy material has a large perpendicular anisotropy, which requires a large external magnetic field to align spins in the plane. This high field pushed the limit of our magnet to the point where our cooling lines could not dissipate enough heat to sustain such a large field without risking potential damage to the magnet and power supply. Being so close to this damage threshold meant the field was not particularly stable and would fluctuate on the order of 100 Oe. This meant that the peaks measured by BLS would be broad and hide the small frequency shifts due to the interfacial DMI.

Additionally, each measurement seen in Figure 7.4 took roughly 48 hours to acquire. During that time, the temperature in the lab room would fluctuate anywhere from 3-10 degrees Fahrenheit, which would cause our laser to be unstable and our interferometer alignment to become skewed introducing further noise and signal broadening.

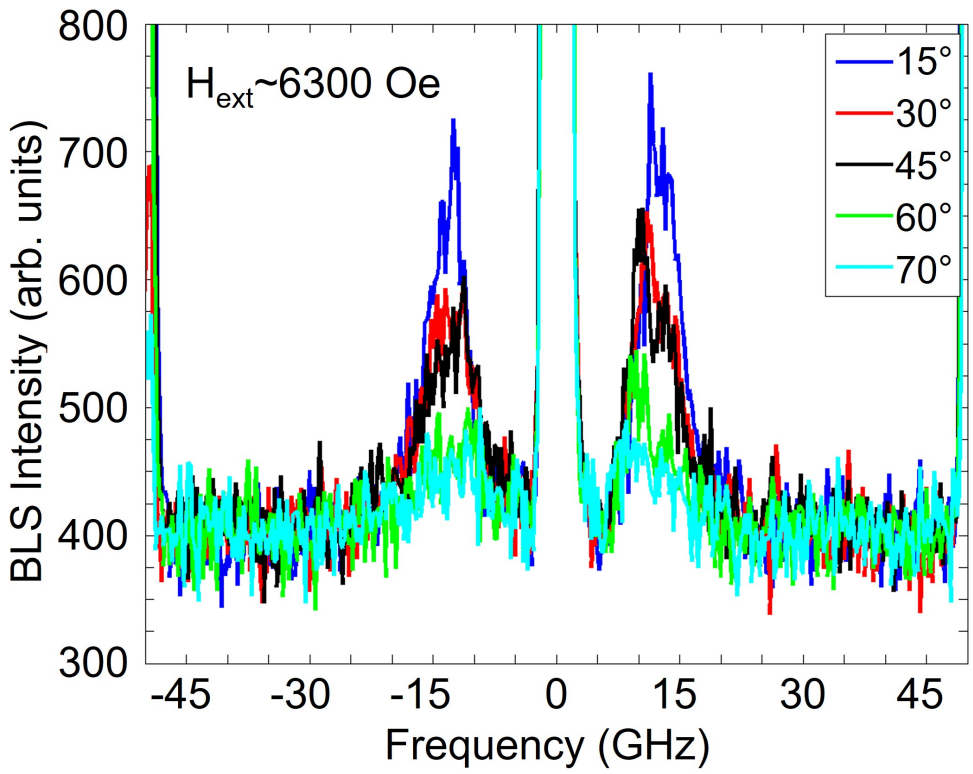

Figure 7.4: BLS data of surface spin waves corresponding to five different angles of a GdCo sample in the conventional BLS 180° back scattering configuration. These measurements have too much noise to determine small frequency differences between the Stokes and anti-Stokes peaks or between peaks for opposite field directions (only one field direction shown).

A third thing that we learned with these samples, was that a multilayer stack repeated >8 times was more difficult to measure than a stack with a non-repeated (single) trilayer. The repeated stacks had a poor signal to noise ratio, which resulted in longer data collection times to find any signal.

While these measurements did not allow for the calculation of the interfacial Dzyaloshinskii-Moriya interaction value, they were critical to understanding the limitations of our system. These measurements identified the need for better temperature control in the lab, a more stable magnet that the cooling system can keep up with to maintain a large external field applied to the sample, and the need for simplified samples with a single trilayer of a magnetic material sandwiched between two heavy metals, all of which must be addressed in order to successfully extract interfacial DMI values.

Chapter 8

Conclusions

8.1 Summary

The projects described in this thesis truly speak to the versatility of Brillouin light scattering measurements for different materials and wave excitations. The magnetoelastic waves measured in a nickel film in Chapter 4, were excited by a surface acoustic wave, and allowed us to not only measure the decay length of this coupled wave but also a nonlinear $2f$ signal not visible in the electrical measurements. The thermal phonons measured in Chapter 5 for the glass and epoxy encapsulation materials allowed us to determine wave speeds for both bulk and surface phonons, which in turn allowed us to calculate elastic constants for these material. The Chapter 6 spin waves in Permalloy were driven by an antenna in a confined structure where we were able to study the magnetic dispersion curves as a spin wave traveled into a different geometry with respect to the excitation antenna and applied field. The spin waves generated near the antenna in the arms of the Y-structure were low-k, however when they moved to the base of the Y-structure they shifted to high-k spin waves, which provides the magnonics community an additional method for generating short wavelength spin waves. Chapter 7 looked at another confinement geometry, interfacial Dzyaloshinskii-Moriya interactions, and magnetic exchange values for a material with a metal-insulator transition near room temperature through BLS spin wave measurements. While the measurements presented in Chapter 7 were inconclusive, they were critical in revealing where we could improve our measurement system to produce a larger signal strength, reduce measurement time, and create more reliable data sets.

We started making system improvements with the addition of a second BLS system in 2018. I set up this second system in a different lab room that was retrofit with a new HVAC system that can control the temperature in the lab to $\pm$ 1.5°F (the previous lab could have daily fluctuations of 3 -10°F). This second BLS system has a brand new TFP2-HC interferometer (described in Sec-

tion 3.1.2) from Table Stable, which claims to have a higher contrast of 4 orders of magnitude over the TFP1 model that was a part of our original BLS system. Additionally, a new magnet along with a new heat exchanger was installed with our second BLS system, which boasts a stability of ± 0.1 Oe (3 - 4 orders of magnitude better than our original system) and can easily reach a field of 15 kOe without overheating (the magnet with the original system could only reach 7 kOe and that was with potential damage from overheating). The second BLS system also uses a 2.5 W laser that must be stepped down to ~ 200 mW to prevent damage to the optics used to steer the laser beam. The second BLS system laser also has a significantly smaller beam divergence so more of the beam is directed to the sample.

With the $60\times$ faster measurement time, $70\times$ lower background of the TFP2-HC interferometer, a magnet with over twice the field range and over three orders of magnitude better stability, many on going projects where the magnon or phonon signal is weak would benefit to have data retaken with the new BLS system. Additionally, this second BLS system is stable enough to make interfacial DMI measurements. The data shown in Section 7.3 took ten days of continuous measurement but the same data can be taken on our second BLS system in under a day, but with far less noise such that the frequency shifts between field directions or Stokes and anti-Stokes signals can be measured and used to calculate the interfacial DMI value.

In addition to the new BLS system, the original BLS interferometer has been upgraded from a TFP1 to a TFP2-HC so the beam paths inside both interferometers are identical. Though the original system still has the same magnet and laser as it did before the interferometer upgrade, the lab room housing the original system has also been retrofit with a new HVAC to provide ± 1°F, making the laser far more stable. This HVAC has slightly better temperature control due to the room being quite a bit smaller.

Bibliography

[1] International Roadmap for Devices and Systems (IRDS™) 2021 Edition. Tech. Rep., IEEE (2021).

[2] Khitun, A., Bao, M. & Wang, K. L. Magnonic logic circuits. *Journal of Physics D: Applied Physics* **43**, 264005 (2010).

[3] Carlotti, G. Elastic characterization of transparent and opaque films, multilayers and acoustic resonators by surface Brillouin scattering: A review. *Applied Sciences (Switzerland)* **8**, 124 (2018).

[4] Auld, B. A. *Acoustic Fields and Waves in Solids* (Wiley, New York, 1973).

[5] Farnell, G. W. & Adler, E. L. Elastic Wave Propagation in Thin Layers. In *Physical Acoustics*, vol. 9, chap. 2, 35–127 (ACADEMIC PRESS, INC., 1972).

[6] Calás, H., Rodriguez-Ramos, R., Otero, J. A., Leija, L., Ramos, A. & Monsivais, G. Dispersion curves of shear horizontal wave surface velocities in multilayer piezoelectric systems. *Journal of Applied Physics* **107**, 044511 (2010).

[7] Albuquerque, E. L., Loudon, R. & Tilley, D. R. Theory of Brillouin scattering by Love waves. *Journal of Physics C: Solid State Physics* **13**, 1775–1789 (1980).

[8] Rayleigh, L. On waves propagated along the plane surface of an elastic solid. *Proceedings of the London Mathematical Society* **s1-17**, 4–11 (1885).

[9] Camley, R. E. & Fulde, P. Theory of Rayleigh waves on paramagnetic rare-earth systems. *Physical Review B* **23**, 2614–2619 (1981).

[10] Kiselev, A. P. & Parker, D. F. Omni-directional Rayleigh, Stoneley and Schölte waves with general time dependence. *Proceedings of the Royal Society A: Mathematical, Physical and Engineering Sciences* **466**, 2241–2258 (2010).

[11] Sokolova, E. S., Kovalev, A. S., Maznev, A. A. & Mayer, A. P. Acoustic waves guided by the intersection of a surface and an interface of two elastic media. *Wave Motion* **49**, 388–393 (2012).

[12] Flores-Mendez, E., Carbajal-Romero, M., Flores-Guzmán, N., Sánchez-Martínez, R. & Rodríguez-Castellanos, A. Rayleigh's, Stoneley's, and Scholte's interface waves in elastic models using a boundary element method. *Journal of Applied Mathematics* **2012**, 313207 (2012).

[13] Stoneley, R. Elastic waves at the surface of separation of two solids. *Proceedings of the Royal Society of London. Series A, Containing Papers of a Mathematical and Physical Character* **106**, 416–428 (1924).

[14] Pilant, W. L. Complex Roots of the Stoneley-wave Equation. *Bullentin of the Seismological Society of America* **62**, 285–299 (1972).

[15] Albuquerque, E. L. Theory of Brillouin scattering by Stoneley waves. *Journal of Physics C: Solid State Physics* **13**, 2623–2639 (1980).

[16] Sezawa, K. & Kanai, K. The range of possible existence of Stoneley-waves, and some related problems. *Bulletin of the Earthquake Research Institute* **17**, 25 (1939).

[17] Mohanan, A. A., Islam, S., Hamid, S., Ali, M., Parthiban, R. & Ramakrishnan, N. Investigation into mass loading sensitivity of Sezawa wave mode-based surface acoustic wave sensors. *Sensors* **13**, 2164–2175 (2013).

[18] Kushibiki, J., Ishikawa, T. & Chubachi, N. Cut-off characteristics of leaky Sezawa and pseudo-Sezawa wave modes for thin-film characterization. *Appl. Phys. Lett* **57**, 1967 (1990).

[19] Lamb, H. On Waves in an elastic plate. *Proceedings of the Royal Society of London. Series A, Containing papers of a mathematical and physical character* **93**, 114–128 (1917).

[20] Torvik, P. J. Reflection of wave trains in semi-infinite plates. *The Journal of the Acoustical Society of America* **41**, 346 (1967).

[21] Cho, Y. & Rose, J. L. A boundary element solution for a mode conversion study on the edge reflection of Lamb waves. *The Journal of the Acoustical Society of America* **99**, 2097 (1996).

[22] Kittel, C. On the theory of ferromagnetic resonance absorption. *Physical Review* **73**, 155–161 (1948).

[23] Stancil, D. D. & Prabhakar, A. *Spin Waves Theory and Applications* (Springer, 2009).

[24] Serga, A. A., Chumak, A. V. & Hillebrands, B. YIG magnonics. *Journal of Physics D: Applied Physics* **43**, 264002 (2010).

[25] Kalinikos, B. A. & Slavin, A. N. Theory of dipole-exchange spin wave spectrum for ferromagnetic films with mixed exchange boundary conditions. *Journal of Physics C: Solid State Phyics* **19**, 7013–7033 (1986).

[26] Yang, W. G. & Schmidt, H. Acoustic control of magnetism toward energy-efficient applications. *Applied Physics Reviews* **8**, 021304 (2021).

[27] Cullity, B. & Graham, C. *Introduction to Magnetic Materials* (John Wiley & Sons, 2009), 2nd edn.

[28] Gao, C., Zeng, Z., Peng, S. & Shuai, C. Magnetostrictive alloys: Promising materials for biomedical applications. *Bioactive Materials* **8**, 177–195 (2022).

[29] Bhattacharya, B. Terfenol and Galfenols : Smart magnetostrictive metals for intelligent transduction. *Directions magazine (Indian Institute od Technology Kanpur)* **7**, 35–40 (2005).

[30] Clark, A. E. & Wun-Fogle, M. Modern magnetostricitive materials: classical and non-classical alloys. *Procedings of SPIE 4699, Smart Structures and Materials 2002: Active Materials: Behavior and Mechanics* **4699**, 421–436 (2002).

[31] Ostler, T. A., Cuadrado, R., Chantrell, R. W., Rushforth, A. W. & Cavill, S. A. Strain induced vortex core switching in planar magnetostrictive nanostructures. *Physical Review Letters* **115**, 067202 (2015).

[32] Tejada, J., Chudnovsky, E. M., Zarzuela, R., Statuto, N., Calvo-De La Rosa, J., Santos, P. V. & Hernández-Mínguez, A. Switching of magnetic moments of nanoparticles by surface acoustic waves. *Europhysics Letters* **118**, 37005 (2017).

[33] Sampath, V., D'Souza, N., Bhattacharya, D., Atkinson, G. M., Bandyopadhyay, S. & Atulasimha, J. Acoustic-wave-induced magnetization switching of magnetostrictive nanomagnets from single-domain to nonvolatile vortex states. *Nano Letters* **16**, 5681–5687 (2016).

[34] Kuszewski, P., Camara, I. S., Biarrotte, N., Becerra, L., Von Bardeleben, J., Savero Torres, W., Lemaître, A., Gourdon, C., Duquesne, J. Y. & Thevenard, L. Resonant magneto-acoustic switching: Influence of Rayleigh wave frequency and wavevector. *Journal of Physics Condensed Matter* **30**, 244003 (2018).

[35] Roy, K., Bandyopadhyay, S. & Atulasimha, J. Hybrid spintronics and straintronics: A magnetic technology for ultra low energy computing and signal processing. *Applied Physics Letters* **99**, 63108 (2011).

[36] Elhajjar, R., Law, C. T. & Pegoretti, A. Magnetostrictive polymer composites: Recent advances in materials, structures and properties. *Progress in Materials Science* **97**, 204–229 (2018).

[37] Joule, J. P. On a new class of magnetic forces. *Ann. Electr. Magn. Chem* **8**, 219–224 (1842).

[38] Joule, J. XVII. On the effects of magnetism upon the dimensions of iron and steel bars. *The London, Edinburgh, and Dublin Philosophical Magazine and Journal of Science* **30**, 76–87 (1847).

[39] Villari, E. Ueber die Aenderungen des magnetischen Moments, welche der Zug und das Hindurchleiten eines galvanischen Stroms in einem Stabe von Stahl oder Eisen hervorbringen. *Annalen der Physik und Chemie* **202**, 87–122 (1865).

[40] Brillouin, L. Diffusion de la lumière et des rayons X par un corps transparent homogène. Influence de l'agitation thermique. *Annales de Physique* **9**, 88–122 (1922).

[41] Mandelstam, L. I. Light scattering by inhomogeneous media. *Zh. Russ. Fiz. Khim. Ova* **58**, 146 (1926).

[42] Gross, E. Change of wave-length of light due to elastic heat waves at scattering in liquids. *Nature* **126**, 201–202 (1930).

[43] Gross, E. The splitting of spectral lines in scattering of light by liquids. *Nature* **126**, 400 (1930).

[44] Gross, E. über Änderung der WellenlÄnge bei Lichtzerstreuung in Kristallen. *Z. Physik* **63**, 685–687 (1930).

[45] Maiman, T. H. Optical and microwave-optical experiments in ruby. *Physical Review Letters* **4**, 564–566 (1960).

[46] Michelson, A. A. & Morley, E. W. On the relative motion of the Earth and the luminiferous ether. *American Journal of Science* **s3-34**, 333–345 (1887).

[47] Sandercock, J. Brillouin scattering study of SbSI using a double-passed, stabilised scanning interferometer. *Optics Communications* **2**, 73–76 (1970).

[48] Bradley, L. C. & Kuhn, H. Spectrum of Helium-3. *Nature* **162**, 412–413 (1948).

[49] Kuhn, H. The use of two Fabry-Perot interferometers in series for the detection of faint satellites. *Journal de Physique et le Radium* **11**, 425–426 (1950).

[50] Rank, D. H., Ruth, R. P. & Vander Sluis, K. L. The compound Fabry-Perot interferometer. *Journal of the Optical Society of America* **41**, 351–353 (1951).

[51] Dufour, C., Herpin, A. & Thomas, J.-P. Mise en évidence directe de la conductibilité d'un diélectrique mince soumis à un bombardement électronique. *Journal de Physique et le Radium* **12**, 887–888 (1951).

[52] Hariharan, P. & Sen, D. Double-passed Fabry-Perot interferometer. *Journal of the Optical Society of America* **51**, 398 (1961).

[53] Speziale, S., Marquardt, H. & Duffy, T. S. Brillouin scattering and its application in geosciences. *Reviews in Mineralogy and Geochemistry* **78**, 543–603 (2014).

[54] Schneider, D., Gomopoulos, N., Koh, C. Y., Papadopoulos, P., Kremer, F., Thomas, E. L. & Fytas, G. Nonlinear control of high-frequency phonons in spider silk. *Nature Materials* **15**, 1079–1083 (2016).

[55] Antonacci, G. & Braakman, S. Biomechanics of subcellular structures by non-invasive Brillouin microscopy. *Scientific Reports* **6**, 37217 (2016).

[56] Scarcelli, G. & Yun, S. H. Confocal Brillouin microscopy for three-dimensional mechanical imaging. *Nature Photonics* **2**, 39–43 (2008).

[57] Mattana, S., Mattarelli, M., Urbanelli, L., Sagini, K., Emiliani, C., Serra, M. D., Fioretto, D. & Caponi, S. Non-contact mechanical and chemical analysis of single living cells by microspectroscopic techniques. *Light: Science and Applications* **7**, 17139 (2018).

[58] Liu, H. J., Riley, G. A. & Buchanan, K. S. Directly Excited Backward Volume Spin Waves in Permalloy Microstrips. *IEEE Magnetics Letters* **6**, 4000304 (2015).

[59] Liu, H. J., Guerrero, A., Nygren, K. E., Swyt, M. & Buchanan, K. S. Spin wave wavevector up-conversion in Y-shaped Permalloy structures. *Applied Physics Letters* **119**, 172403 (2021).

[60] Haldar, A. & Buchanan, K. S. Magnetic antivortex formation in pound-key-like nanostructures. *Applied Physics Letters* **102**, 112401 (2013).

[61] Ordóñez-Romero, C. L., Kalinikos, B. A., Krivosik, P., Tong, W., Kabos, P. & Patton, C. E. Three-magnon splitting and confluence processes for spin-wave excitations in yttrium iron garnet films: Wave vector selective Brillouin light scattering measurements and analysis. *Physical Review B - Condensed Matter and Materials Physics* **79**, 144428 (2009).

[62] Mathieu, C., Liu, H. J., Buchanan, K. S. & Inturi, V. R. Volume exchange in soft FeCo films of high magnetization. *Journal of Applied Physics* **111**, 07A306 (2012).

[63] Bortolani, V., Nizzoli, F., Santoro, G. & Sandercock, J. R. Strong interference effects in surface Brillouin scattering from a supported transparent film. *Physical Review B* **25**, 3442–3445 (1982).

[64] Carlotti, G., Fioretto, D., Socino, G. & Verona, E. Brillouin scattering determination of the whole set of elastic constants of a single transparent film of hexagonal symmetry. *Journal of Physics: Condensed Matter* **7**, 9147–9153 (1995).

[65] Sandercock, J. R. & Wettling, W. Light scattering from surface and bulk thermal magnons in iron and nickel. *Journal of Applied Physics* **50**, 7784 (1979).

[66] Bassoli, L., Nizzoli, F. & Sandercock, J. R. Surface Brillouin scattering in polycrystalline gold. *Physical Review B* **34**, 1296–1299 (1986).

[67] Rowell, N. & Stegeman, G. I. Brillouin scattering from isotropic metals. *Solid State Communications* **26**, 809–812 (1978).

[68] Sandercock, J. & Wettling, W. Light scattering from thermal acoustic magnons in yttrium iron garnet. *Solid State Communications* **13**, 1729–1732 (1973).

[69] Litvinenko, A. N., Sadovnikov, A. V., Tikhonov, V. V. & Nikitov, S. A. Brillouin light scattering spectroscopy of magneto-acoustic resonances in a thin-film garnet resonator. *IEEE Magnetics Letters* **6**, 3200204 (2015).

[70] Panella, V., Carlotti, G., Socino, G., Giovanninii, L., Eddrief, M. & Sebenne, C. Elastic properties of GaSe films epitaxially grown on the Si(111)1 × 1-H surface, studied by Brillouin scattering. *Journal of Physics Condensed Matter* **11**, 6661–6668 (1999).

[71] Sandercock, J. R. Light scattering from surface acoustic phonons in metals and semiconductors. *Solid State Communications* **26**, 547–551 (1978).

[72] Rouxel, D., Thevenot, C., Nguyen, V. S. & Vincent, B. Brillouin Spectroscopy of Polymer Nanocomposites. In *Spectroscopy of Polymer Nanocomposites*, chap. 12, 362–392 (William Andrew Publishing, 2016).

[73] Loudon, R. & Sandercock, J. R. Analysis of the light-scattering cross section for surface ripples on solids. *Journal of Physics C: Solid State Physics* **13**, 2609–2622 (1980).

[74] Demidov, V. E., Kostylev, M. P., Rott, K., Krzysteczko, P., Reiss, G. & Demokritov, S. O. Generation of the second harmonic by spin waves propagating in microscopic stripes. *Physical Review B* **83**, 054408 (2011).

[75] Sandweg, C. W., Kajiwara, Y., Chumak, A. V., Serga, A. A., Vasyuchka, V. I., Jungfleisch, M. B., Saitoh, E. & Hillebrands, B. Spin pumping by parametrically excited exchange magnons. *Physical Review Letters* **106**, 216601 (2011).

[76] Sebastian, T., Schultheiss, K., Obry, B. B., Hillebrands, B. & Schultheiss, H. Micro-focused Brillouin light scattering: imaging spin waves at the nanoscale. *Frontiers in Physics* **3**, 35 (2015).

[77] Bottani, C. E. & Fioretto, D. Brillouin scattering of phonons in complex materials. *Advances in Physics: X* **3**, 607–633 (2018).

[78] Demidov, V. E., Demokritov, S. O., Rott, K., Krzysteczko, P. & Reiss, G. Linear and nonlinear spin-wave dynamics in macro- and microscopic magnetic confined structures. *Journal of Physics D: Applied Physics* **41**, 164012 (2008).

[79] Chaurasiya, A. K., Banerjee, C., Pan, S., Sahoo, S., Choudhury, S., Sinha, J. & Barman, A. Direct observation of interfacial Dzyaloshinskii-Moriya interaction from asymmetric spin-wave propagation in W/CoFeB/SiO2 heterostructures down to sub-nanometer CoFeB thickness. *Scientific Reports* **6**, 32592 (2016).

[80] Nembach, H. T., Shaw, J. M., Weiler, M., Jué, E. & Silva, T. J. Linear relation between Heisenberg exchange and interfacial Dzyaloshinskii-Moriya interaction in metal films. *Nature Physics* **11**, 825–829 (2015).

[81] Kim, N. H., Jung, J., Cho, J., Han, D. S., Yin, Y., Kim, J. S., Swagten, H. J. & You, C. Y. Interfacial Dzyaloshinskii-Moriya interaction, surface anisotropy energy, and spin pumping at spin orbit coupled Ir/Co interface. *Applied Physics Letters* **108**, 142406 (2016).

[82] Sebastian, T. *et al.* Low-damping spin-wave propagation in a micro-structured Co 2Mn 0.6Fe 0.4Si Heusler waveguide. *Applied Physics Letters* **100**, 112402 (2012).

[83] Mathieu, C., Synogatch, V. T. & Patton, C. E. Brillouin light scattering analysis of three-magnon splitting processes in yttrium iron garnet films. *Physical Review B - Condensed Matter and Materials Physics* **67**, 104402 (2003).

[84] Sandercock, J. R. Trends in Brillouin Scattering: Studies of Opaque Materials, Supported Films, and Central Modes. In Cardona, M. & Guntherodt, G. (eds.) *Light Scattering in Solids III. Topics in Applied Physics*, vol. 51, chap. 6 (Springer Berlin, Heidelberg, 1982).

[85] Kargar, F. & Balandin, A. A. Advances in Brillouin–Mandelstam light-scattering spectroscopy. *Nature Photonics* **15**, 720–731 (2021).

[86] Kojima, S. 100th Anniversary of Brillouin scattering: Impact on materials science. *Materials* **15**, 3518 (2022).

[87] Lockwood, D. J. Light Scattering from Electronic and Magnetic Excitations in Transition-Metal Halides. In Cardona, M. & Guntherodt, G. (eds.) *Light Scattering in Solids III. Topics in Applied Physics*, vol. 51, chap. 3 (Springer Berlin, Heidelberg, 1982).

[88] The Table Stable Ltd. Tandem Fabry-Perot Spectrometers TFP-1 AND TFP-2 HC Operators Manual v1.6 (2005). URL www.tablestable.com.

[89] Kalarickal, S. S. *Ferromagnetic relaxation in (1) metallic thin films and (2) bulk ferrites and composite materials or information storage device and microwave applications*. Ph.D. thesis, Colorado State University (2006).

[90] Neudecker, I., Woltersdorf, G., Heinrich, B., Okuno, T., Gubbiotti, G. & Back, C. H. Comparison of frequency, field, and time domain ferromagnetic resonance methods. *Journal of Magnetism and Magnetic Materials* **307**, 148–156 (2006).

[91] Barry, W. A broad-band, automated, stripline technique for the simultaneous measurement of complex permittivity and permeability. *IEEE Transactions on Microwave Theory and Techniques* **34**, 80–84 (1986).

[92] Weir, W. B. Automatic measurement of complex dielectric constant and permeability at microwave frequencies. *Proceedings of the IEEE* **62**, 33–36 (1974).

[93] Kalarickal, S. S., Krivosik, P., Wu, M., Patton, C. E., Schneider, M. L., Kabos, P., Silva, T. J. & Nibarger, J. P. Ferromagnetic resonance linewidth in metallic thin films: Comparison of measurement methods. *Journal of Applied Physics* **99**, 093909 (2006).

[94] Hurben, M. J. *Two Magnon Scattering and Relaxation in thin ferrite films*. Ph.D. thesis, Colorado State University (1996).

[95] Sun, Y. & Wu, M. Yttrium Iron Garnet Nano Films: Epitaxial Growth, Spin-pumping Efficiency, and Pt-Capping-Caused Damping. In Wu, M. & Hoffmann, A. (eds.) *Solid State Physics: Recent Advances in Magnetic Insulators - From Spintronics to Microwave Applications*, vol. 64, chap. 6, 157–191 (Elsevier Inc., 2013), 1 edn.

[96] Chumak, A. V., Vasyuchka, V. I., Serga, A. A. & Hillebrands, B. Magnon spintronics. *Nature Physics* **11**, 453–461 (2015).

[97] Shen, K. & Bauer, G. E. Theory of spin and lattice wave dynamics excited by focused laser pulses. *Journal of Physics D: Applied Physics* **51**, 224008 (2018).

[98] Serga, A. A., Sandweg, C. W., Vasyuchka, V. I., Jungfleisch, M. B., Hillebrands, B., Kreisel, A., Kopietz, P. & Kostylev, M. P. Brillouin light scattering spectroscopy of parametrically excited dipole-exchange magnons. *Physical Review B* **86**, 134403 (2012).

[99] Chen, C., Barra, A., Mal, A., Carman, G. & Sepulveda, A. Voltage induced mechanical/spin wave propagation over long distances. *Applied Physics Letters* **110**, 72401 (2017).

[100] Foerster, M. *et al.* Direct imaging of delayed magneto-dynamic modes induced by surface acoustic waves. *Nature Communications* **8**, 407 (2017).

[101] Casals, B., Statuto, N., Foerster, M., Hernández-Mínguez, A., Cichelero, R., Manshausen, P., Mandziak, A., Aballe, L., Hernàndez, J. M. & Macià, F. Generation and imaging of magnetoacoustic waves over millimeter distances. *Physical Review Letters* **124**, 137202 (2020).

[102] Labanowski, D., Bhallamudi, V. P., Guo, Q., Purser, C. M., McCullian, B. A., Chris Hammel, P., Salahuddin, S., Hammel, P. C. & Salahuddin, S. Voltage-driven, local, and efficient excitation of nitrogen-vacancy centers in diamond. *Science Advances* **4**, eaat6574 (2018).

[103] Weiler, M., Dreher, L., Heeg, C., Huebl, H., Gross, R., Brandt, M. S. & Goennenwein, S. T. B. B. Elastically driven ferromagnetic resonance in nickel thin films. *Physical Review Letters* **106**, 117601 (2011).

[104] Dreher, L., Weiler, M., Pernpeintner, M., Huebl, H., Gross, R., Brandt, M. S. & Goennenwein, S. T. B. B. Surface acoustic wave driven ferromagnetic resonance in nickel thin films: Theory and experiment. *Physical Review B* **86**, 134415 (2012).

[105] Labanowski, D., Jung, A. & Salahuddin, S. Power absorption in acoustically driven ferromagnetic resonance. *Applied Physics Letters* **108**, 22905 (2016).

[106] Li, X., Labanowski, D., Salahuddin, S. & Lynch, C. S. Spin wave generation by surface acoustic waves. *Journal of Applied Physics* **122**, 43904 (2017).

[107] Slobodnik, A. J. Surface acoustic waves and SAW materials. *Proceedings of the IEEE* **64**, 581–595 (1976).

[108] Zhou, H., Talbi, A., Tiercelin, N. & Bou Matar, O. Multilayer magnetostrictive structure based surface acoustic wave devices. *Applied Physics Letters* **104**, 114101 (2014).

[109] Campbell, C. K. Applications of Surface Acoustic and Shallow Bulk Acoustic Wave Devices. *Proceedings of the IEEE* **77**, 1453–1484 (1989).

[110] Carman, G. P. & Sun, N. Strain-mediated magnetoelectrics: Turning science fiction into reality. *MRS Bulletin* **43**, 822–828 (2018).

[111] Song, O., Ballentine, C. A. & O'Handley, R. C. Giant surface magnetostriction in polycrystalline Ni and NiFe films. *Applied Physics Letters* **64**, 2593–2595 (1994).

[112] Berger, L. Magnetostriction in Nickel Alloys. *Physical Review* **138**, A1083–A1087 (1965).

[113] Mason, W. P. A phenomenological derivation of the first- and second-order magnetostriction and morphic effects for a nickel crystal. *Physical Review* **82**, 715–723 (1951).

[114] Labanowski, D., Jung, A. & Salahuddin, S. Effect of magnetoelastic film thickness on power absorption in acoustically driven ferromagnetic resonance. *Applied Physics Letters* **111**, 102902–102905 (2017).

[115] Paskauskas, J., Rimeika, R. & Čiplys, D. Velocity and attenuation of surface acoustic waves in proton-exchanged 128°-rotated Y-cut LiNbO3. *Journal of Physics D: Applied Physics* **28**, 1419–1423 (1995).

[116] Geller, S. & Gilleo, M. A. Structure and ferrimagnetism of yttrium and rare-earth–iron garnets. *Acta Crystallographica* **10**, 239–239 (1957).

[117] Sun, Y., Song, Y.-Y. & Chang, H. Growth and ferromagnetic resonance properties of nanometer-thick yttrium iron garnet films. *Appl. Phys. Lett* **101**, 152405 (2012).

[118] Chang, H., Li, P., Zhang, W., Liu, T., Hoffmann, A., Deng, L. & Wu, M. Nanometer-thick yttrium iron garnet films with extremely low damping. *IEEE Magnetics Letters* **5**, 6700104 (2014).

[119] Padrón-Hernández, E., Azevedo, A. & Rezende, S. M. Amplification of spin waves in yttrium iron garnet films through the spin Hall effect. *Applied Physics Letters* **99**, 192511 (2011).

[120] Schloemann, E. F. Circulators for microwave and millimeter-wave integrated circuits. *Proceedings of the IEEE* **76**, 188–200 (1988).

[121] Rodrigue, G. P. A generation of microwave ferrite devices. *Proceedings of the IEEE* **76**, 121–137 (1988).

[122] Roumie, M., Samad, B. A., Tabbal, M., Abi-Akl, M., Blanc-Mignon, M. F. & Nsouli, B. Effect of deposition temperature on the properties of sputtered YIG films grown on quartz. *Materials Chemistry and Physics* **124**, 188–191 (2010).

[123] Shone, M. The technology of YIG film growth. *Circuits, Systems, and Signal Processing* **4**, 89–103 (1985).

[124] Dubs, C., Surzhenko, O., Thomas, R., Osten, J., Schneider, T., Lenz, K., Grenzer, J., Hübner, R. & Wendler, E. Low damping and microstructural perfection of sub-40nm-thin yttrium iron garnet films grown by liquid phase epitaxy. *Physical Review Materials* **4**, 024416 (2020).

[125] Manriquez, J. M., Yee, G. T., Mclean, R. S., Epstein, A. J. & Miller, J. S. A room-temperature molecular / organic-based magnet. *Science* **252**, 1415–1417 (1991).

[126] Liu, H. *et al.* Organic-based magnon spintronics. *Nature Materials* **17**, 308–312 (2018).

[127] Zhu, N., Zhang, X., Froning, I. H., Flatté, M. E., Johnston-Halperin, E. & Tang, H. X. Low loss spin wave resonances in organic-based ferrimagnet vanadium tetracyanoethylene thin films. *Applied Physics Letters* **109**, 082402 (2016).

[128] Franson, A., Zhu, N., Kurfman, S., Chilcote, M., Candido, D. R., Buchanan, K. S., Flatté, M. E., Tang, H. X. & Johnston-Halperin, E. Low-damping ferromagnetic resonance in electron-beam patterned, high- Q vanadium tetracyanoethylene magnon cavities. *APL Materials* **7**, 121113 (2019).

[129] Yu, H., Harberts, M., Adur, R., Lu, Y., Hammel, P. C., Johnston-Halperin, E. & Epstein, A. J. Ultra-narrow ferromagnetic resonance in organic-based thin films grown via low temperature chemical vapor deposition. *Applied Physics Letters* **105**, 12407 (2014).

[130] Pokhodnya, K. I., Epstein, A. J. & Miller, J. S. Thin-film V[TCNE]x magnets. *Adv. Mater* **12**, 410–413 (2000).

[131] Pokhodnya, K. I., Bonner, M. & Miller, J. S. Parylene protection coatings for thin film V[TCNE]x room temperature magnets. *Chemistry of Materials* **16**, 5114–5119 (2004).

[132] de Caro, D., Basso-Bert, M., Sakah, J., Casellas, H., Legros, J.-P., Valade, L. & Cassoux, P. CVD-grown thin films of molecule-based magnets. *Chemistry of Materials* **12**, 587–589 (2000).

[133] Prigodin, V. N., Raju, N. P., Pokhodnya, K. I., Miller, J. S. & Epstein, A. J. Spin-driven resistance in organic-based magnetic semiconductor V[TCNE]x. *Advanced Materials* **14**, 1230–1233 (2002).

[134] Plachy, R., Pokhodnya, K. I., Taylor, P. C., Shi, J., Miller, J. S. & Epstein, A. J. Ferrimagnetic resonance in films of vanadium [tetracyanoethanide]x, grown by chemical vapor deposition. *Physical Review B - Condensed Matter and Materials Physics* **70**, 064411 (2004).

[135] Miller, J. S. Oliver Kahn Lecture: Composition and structure of the V[TCNE]x (TCNE = tetracyanoethylene) room-temperature, organic-based magnet - A personal perspective. *Polyhedron* **28**, 1596–1605 (2009).

[136] Tengstedt, C., De Jong, M. P., Kanciurzewska, A., Carlegrim, E. & Fahlman, M. X-ray magnetic circular dichroism and resonant photomission of V(TCNE)x hybrid magnets. *Physical Review Letters* **96**, 057209 (2006).

[137] Harberts, M., Lu, Y., Yu, H., Epstein, A. J. & Johnston-Halperin, E. Chemical vapor deposition of an organic magnet, vanadium tetracyanoethylene. *Journal of Visualized Experiments* **101**, e52891 (2015).

[138] Johnston-Halperin, E. Personal communication.

[139] Chilcote, M. *et al.* Spin-wave confinement and coupling in organic-based magnetic nanostructures. *APL Materials* **7**, 111108 (2019).

[140] Yoo, J. W., Chen, C. Y., Jang, H. W., Bark, C. W., Prigodin, V. N., Eom, C. B. & Epstein, A. J. Spin injection/detection using an organic-based magnetic semiconductor. *Nature Materials* **9**, 638–642 (2010).

[141] Froning, I. H., Harberts, M., Lu, Y., Yu, H., Epstein, A. J. & Johnston-Halperin, E. Thin-film encapsulation of the air-sensitive organic-based ferrimagnet vanadium tetracyanoethylene. *Applied Physics Letters* **106**, 122403 (2015).

[142] Kurfman, S., Franson, A., Shah, P., Shi, Y., Flatté, M., Srinivasan, G., Page, M. & Johnston-Halperin, E. Electric-Field Control of Strain-Driven Tuning of FMR in the Low-Loss Ferrimagnetic Coordination Compound V[TCNE]$_x$. In *APS March Meeting Abstracts*, vol. 2021 of *APS Meeting Abstracts*, S51.006 (2021).

[143] Cheung, H. F. H., Chilcote, M., Yusuf, H., Cormode, D. S., Shi, Y., Kurfman, S., Franson, A., Flatté, M. E., Johnston-Halperin, E. & Fuchs, G. D. Raman spectroscopy and aging of the low-loss ferrimagnet vanadium tetracyanoethylene. *Journal of Physical Chemistry C* **125**, 20380–20388 (2021).

[144] Thomson, W. T. Transmission of elastic waves through a stratified solid medium. *Journal of Applied Physics* **21**, 89–93 (1950).

[145] Haskell, N. A. The dispersion of surface waves on multilayered media. *Bulletin of the Seismological Society of America* **43**, 17–34 (1953).

[146] Buchen, P. W. & Ben-Hador, R. Free-mode surface-wave computations. *Geophysical Journal International* **124**, 869–887 (1996).

[147] Meehan, T. Evolution of the propagator matrix method and its implementation in seismology. *arXiv* 1–12 (2018).

[148] Briggs, A. (ed.) *Advances in Acoustic Microscopy* (Springer US, Boston, MA, 1995).

[149] Orphal, D. L., Anderson, C. E., Behner, T. & Templeton, D. W. Failure and penetration response of borosilicate glass during multiple short-rod impact. *International Journal of Impact Engineering* **36**, 1173–1181 (2009).

[150] Prassianakis, J. N. Correlation of mechanical and acoustical properties of plasticized epoxy polymers. *Journal of Applied Polymer Science* **39**, 2031–2041 (1990).

[151] Oral, I., Guzel, H. & Ahmetli, G. Determining the mechanical properties of epoxy resin (DGEBA) composites by ultrasonic velocity measurement. *Journal of Applied Polymer Science* **127**, 1667–1675 (2013).

[152] Kao, C. Y., Yoo, J. W., Min, Y. & Epstein, A. J. Molecular layer deposition of an organic-based magnetic semiconducting laminate. *ACS Applied Materials and Interfaces* **4**, 137–141 (2012).

[153] Bandhu, R. S., Zhang, X., Sooryakumar, R. & Bussmann, K. Acoustic vibrations in free-standing double layer membranes. *Physical Review B* **70**, 75409 (2004).

[154] Khitun, A. & Wang, K. L. Nano scale computational architectures with spin wave bus. *Superlattices and Microstructures* **38**, 184–200 (2005).

[155] Kostylev, M. P., Serga, A. A., Schneider, T., Leven, B. & Hillebrands, B. Spin-wave logical gates. *Applied Physics Letters* **87**, 153501 (2005).

[156] Barman, A. *et al.* The 2021 Magnonics Roadmap. *Journal of Physics: Condensed Matter* **33**, 413001 (2021).

[157] Mahmoud, A., Ciubotaru, F., Vanderveken, F., Chumak, A. V., Hamdioui, S., Adelmann, C. & Cotofana, S. Introduction to spin wave computing. *Journal of Applied Physics* **128**, 161101 (2020).

[158] Sato, N., Sekiguchi, K. & Nozaki, Y. Electrical demonstration of spin-wave logic operation. *Applied Physics Express* **6**, 063001 (2013).

[159] Nanayakkara, K., Anferov, A., Jacob, A. P., Allen, S. J. & Kozhanov, A. Cross junction spin wave logic architecture. *IEEE Transactions on Magnetics* **50**, 3402204 (2014).

[160] Klingler, S., Pirro, P., Brächer, T., Leven, B., Hillebrands, B. & Chumak, A. V. Spin-wave logic devices based on isotropic forward volume magnetostatic waves. *Applied Physics Letters* **106**, 212406 (2015).

[161] Nanayakkara, K., Jacob, A. P. & Kozhanov, A. Spin wave scattering and interference in ferromagnetic cross. *Journal of Applied Physics* **118**, 163904 (2015).

[162] Balinskiy, M., Gutierrez, D., Chiang, H., Filimonov, Y., Kozhevnikov, A. & Khitun, A. Spin wave interference in YIG cross junction. *AIP Advances* **7**, 056633 (2017).

[163] Csaba, G., Papp, Á. & Porod, W. Perspectives of using spin waves for computing and signal processing. *Physics Letters, Section A: General, Atomic and Solid State Physics* **381**, 1471–1476 (2017).

[164] Fischer, T., Kewenig, M., Bozhko, D. A., Serga, A. A., Syvorotka, I. I., Ciubotaru, F., Adelmann, C., Hillebrands, B. & Chumak, A. V. Experimental prototype of a spin-wave majority gate. *Applied Physics Letters* **110**, 152401 (2017).

[165] Papp, Á., Porod, W., Csurgay, Á. I. & Csaba, G. Nanoscale spectrum analyzer based on spin-wave interference. *Scientific Reports* **7**, 9245 (2017).

[166] Balynskiy, M., Chiang, H., Gutierrez, D., Kozhevnikov, A., Filimonov, Y. & Khitun, A. Reversible magnetic logic gates based on spin wave interference. *Journal of Applied Physics* **123**, 144501 (2018).

[167] Papp, A., Csaba, G., Dey, H., Madami, M., Porod, W. & Carlotti, G. Waveguides as sources of short-wavelength spin waves for low-energy ICT applications. *European Physical Journal B* **91**, 107 (2018).

[168] Yu, H., D'Allivy Kelly, O., Cros, V., Bernard, R., Bortolotti, P., Anane, A., Brandl, F., Heimbach, F. & Grundler, D. Approaching soft X-ray wavelengths in nanomagnet-based microwave technology. *Nature Communications* **7**, 11255 (2016).

[169] Kurebayashi, H., Dzyapko, O., Demidov, V. E., Fang, D., Ferguson, A. J. & Demokritov, S. O. Spin pumping by parametrically excited short-wavelength spin waves. *Applied Physics Letters* **99**, 162502 (2011).

[170] Demokritov, S. O. *Spin wave confinement* (Pan Stanford Publishing, Portland, 2009).

[171] Demidov, V. E., Kostylev, M. P., Rott, K., Mnchenberger, J., Reiss, G. & Demokritov, S. O. Excitation of short-wavelength spin waves in magnonic waveguides. *Applied Physics Letters* **99**, 082507 (2011).

[172] Vogt, K., Schultheiss, H., Jain, S., Pearson, J. E., Hoffmann, A., Bader, S. D. & Hillebrands, B. Spin waves turning a corner. *Applied Physics Letters* **101**, 042410 (2012).

[173] Vogt, K., Fradin, F. Y., Pearson, J. E., Sebastian, T., Bader, S. D., Hillebrands, B., Hoffmann, A. & Schultheiss, H. Realization of a spin-wave multiplexer. *Nature Communications* **5**, 3727 (2014).

[174] Demokritov, S. O. & Demidov, V. E. Micro-brillouin light scattering spectroscopy of magnetic nanostructures. *IEEE Transactions on Magnetics* **44**, 6–12 (2008).

[175] Vansteenkiste, A., Leliaert, J., Dvornik, M., Helsen, M., Garcia-Sanchez, F. & Van Waeyenberge, B. The design and verification of MuMax3. *AIP Advances* **4**, 107133 (2014).

[176] Demidov, V. E., Demokritov, S. O., Rott, K., Krzysteczko, P. & Reiss, G. Mode interference and periodic self-focusing of spin waves in Permalloy microstripes. *Physical Review B - Condensed Matter and Materials Physics* **77**, 064406 (2008).

[177] Bhaskar, U. K., Talmelli, G., Ciubotaru, F., Adelmann, C. & Devolder, T. Backward volume vs Damon-Eshbach: A traveling spin wave spectroscopy comparison. *Journal of Applied Physics* **127**, 033902 (2020).

[178] Chumak, A. V., Serga, A. A. & Hillebrands, B. Magnonic crystals for data processing. *Journal of Physics D: Applied Physics* **50**, 244001 (2017).

[179] Vidyasagar, R., Alves Santos, O., Holanda, J., Cunha, R. O., Machado, F. L., Ribeiro, P. R., Rodrigues, A. R., Mendes, J. B., Azevedo, A. & Rezende, S. M. Giant Zeeman shifts in the optical transitions of yttrium iron garnet thin films. *Applied Physics Letters* **109**, 122402 (2016).

[180] Demidov, V. E. *et al.* Direct observation of dynamic modes excited in a magnetic insulator by pure spin current. *Scientific Reports* **6**, 32781 (2016).

[181] Evelt, M. *et al.* High-efficiency control of spin-wave propagation in ultra-thin yttrium iron garnet by the spin-orbit torque. *Applied Physics Letters* **108**, 172406 (2016).

[182] Imada, M., Fujimori, A. & Tokura, Y. Metal-insulator transitions. *Reviews of Modern Physics* **70**, 1039–1263 (1998).

[183] Sharoni, A., Ramírez, J. G. & Schuller, I. K. Multiple avalanches across the metal-insulator transition of vanadium oxide nanoscaled junctions. *Physical Review Letters* **101**, 026404 (2008).

[184] Ramírez, J. G., Schmidt, R., Sharoni, A., Gómez, M. E., Schuller, I. K. & Patiño, E. J. Ultra-thin filaments revealed by the dielectric response across the metal-insulator transition in VO2. *Applied Physics Letters* **102**, 063110 (2013).

[185] Asayesh-Ardakani, H. *et al.* Atomic origins of monoclinic-tetragonal (rutile) phase transition in doped VO2 nanowires. *Nano Letters* **15**, 7179–7188 (2015).

[186] Nagaosa, N. & Tokura, Y. Topological properties and dynamics of magnetic skyrmions. *Nature Nanotechnology* **8**, 899–911 (2013).

[187] Mühlbauer, S. Skyrmion lattice in a chiral magnet. *Science* **323**, 915 (2009).

[188] Huang, S., Zhou, C., Chen, G., Shen, H., Schmid, A. K., Liu, K. & Wu, Y. Stabilization and current-induced motion of antiskyrmion in the presence of anisotropic Dzyaloshinskii-Moriya interaction. *Physical Review B* **96**, 144412 (2017).

[189] Woo, S. *et al.* Observation of room-temperature magnetic skyrmions and their current-driven dynamics in ultrathin metallic ferromagnets. *Nature Materials* **15**, 501–506 (2016).

[190] Dzyaloshinsky, I. A thermodynamic theory of "weak" ferromagnetism of antiferromagnetics. *Journal of Physics and Chemistry of Solids* **4**, 241–255 (1958).

[191] Moriya, T. New mechanism of anisotropic superexchange interaction. *Physical Review Letters* **4**, 228–230 (1960).

[192] Moriya, T. Anisotropic superexchange interaction and weak ferromagnetism. *Physical Review* **120**, 91–98 (1960).

[193] Fert, A. & Levy, P. M. Role of anisotropic exchange interactions in determining the properties of spin-glasses. *Physical Review letters* **44**, 1538–1541 (1980).

[194] Moon, J. H., Seo, S. M., Lee, K. J., Kim, K. W., Ryu, J., Lee, H. W., McMichael, R. D. & Stiles, M. D. Spin-wave propagation in the presence of interfacial Dzyaloshinskii-Moriya interaction. *Physical Review B - Condensed Matter and Materials Physics* **88**, 184404 (2013).

[195] Hrabec, A., Porter, N. A., Wells, A., Benitez, M. J., Burnell, G., McVitie, S., McGrouther, D., Moore, T. A. & Marrows, C. H. Measuring and tailoring the Dzyaloshinskii-Moriya interaction in perpendicularly magnetized thin films. *Physical Review B - Condensed Matter and Materials Physics* **90**, 020402(R) (2014).

[196] Hrabec, A., Belmeguenai, M., Stashkevich, A., Chérif, S. M., Rohart, S., Roussigné, Y. & Thiaville, A. Making the Dzyaloshinskii-Moriya interaction visible. *Applied Physics Letters* **110**, 242402 (2017).

[197] Guslienko, K. Y., Demokritov, S. O., Hillebrands, B. & Slavin, A. N. Effective dipolar boundary conditions for dynamic magnetization in thin magnetic stripes. *Physical Review B - Condensed Matter and Materials Physics* **66**, 132402 (2002).

[198] Aharoni, A. Demagnetizing factors for rectangular ferromagnetic prisms. *Journal of Applied Physics* **83**, 3432–3434 (1998).

Appendix A

Supplemental Materials: Spin wave up conversion of K-vectors in Y structures

This chapter consists of the supplementary materials for the paper *Spin wave wavevector up-conversion in Y-shaped Permalloy structures*, which was published in Applied Physics Letters in 2021.[2] See the online supplementary material [59] for animations (.mp4 videos) of the spin wave amplitudes noted with (Multimedia view), a still frame will be shown below for reference.

Animations of spin waves in Y-structures

Micromagnetic simulations of spin waves in 40-nm thick Permalloy structures with widths of w = 2.7 μm are shown in Figures A.1, A.2, and A.3 (Multimedia view). The simulations were conducted using a static magnetic field of $\mu_0 H$ = 60 mT applied in-plane, parallel (or almost parallel in the case of Figure A.3 (Multimedia view)) to the antenna, and a driving magnetic field of $h = h_o \sin(2\pi f t)$ was applied in-plane and perpendicular to the antenna within the antenna region. The driving frequency of f = 7.25 GHz corresponds to the strongest excitation amplitude for a microstrip tilted at an angle of 45° with respect to H (45° case, see Figure 6.1). The same material parameters were used for the simulations presented in Figures 6.1(d) and 6.3; the cell size is 21 $\times$ 21 $\times$ 40 nm^3 and the antenna width is 2 μm.

Figure A.1 (Multimedia view) shows the spin wave modes in a long straight Permalloy microstrip oriented at 45° with respect to H (45° case), and Figures A.2 and A.3 (Multimedia view) show the spin waves in the Y structure (Y case) with the field along the antenna, also the y-direction, and misaligned by an angle of -3°, respectively. Figures A.2 and A.3 (Multimedia view) correspond to Figure A.3(c) and (d), respectively. In the 45° case (Figure A.1 (Multimedia view)),

[2]Reproduced here with the permission of AIP Publishing. H. J. Jason Liu, Aron Guerrero, Katherine E. Nygren, Mitchell Swyt, and Kristen S. Buchanan. *Appl. Phys. Lett.* **119**, 172403 (2021).

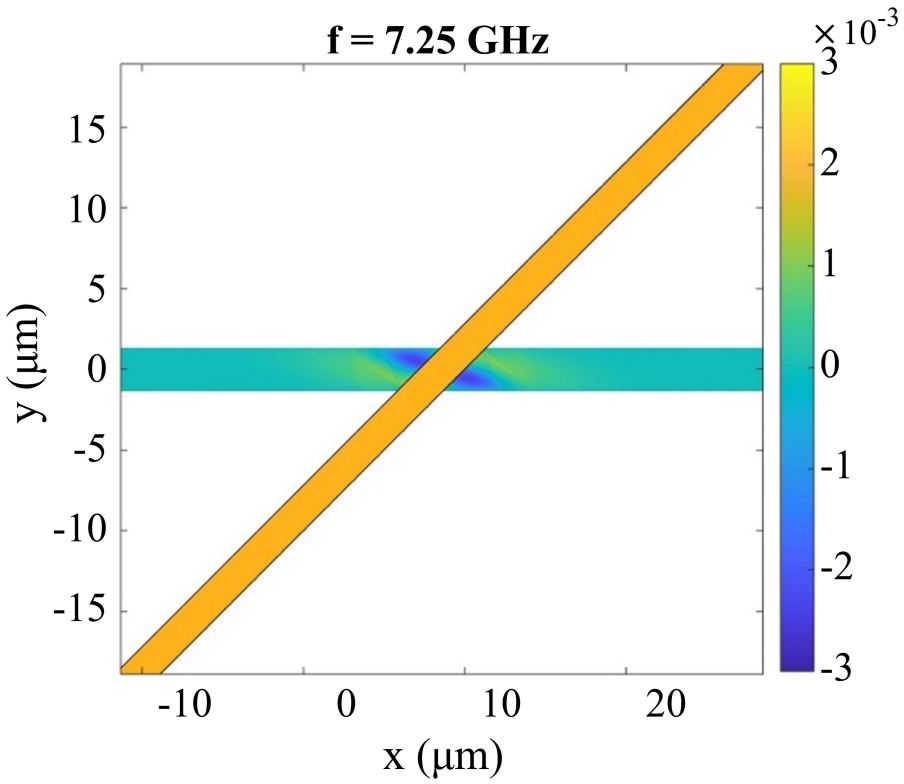

Figure A.1: Calculated spin wave amplitude vs. position for a long straight magnetic microstrip with H along the antenna and at 45° to the microstrip (45° case) with f = 7.25 GHz and $\mu_0 h_0$ = 0.1 mT. The orange rectangle illustrates the location of the antenna and the colormap shows the z-component of the magnetization. (Multimedia view).

the spin waves have a long wavelength and damp out over a short distance (a few micrometers), and they also exhibit backward volume character, i.e., the phase velocity is inward, opposite to the outward-directed group velocity. Figures A.2 and A.3 (Multimedia view) shows that low-k spin waves in the arms of a Y structure will convert into available modes in the base that have larger k_L and shorter wavelengths along the microstrip. When the alignment is perfect the two lowest-order, odd, width-quantized modes are observed in the simulations, whereas with a -3° misalignment the lowest-order, even mode is observed.

The odd modes can be most easily observed in Figure A.2 (Multimedia view) at x = 5 μm where the magnetization is positive near the center with two negative side lobes centered at $y = \pm 0.88\,\mu$m. The magnetization across the width is due to the sum of the n = 1 and n = 3 width-quantized modes that have one and three antinodes across the width, respectively, and are largely in

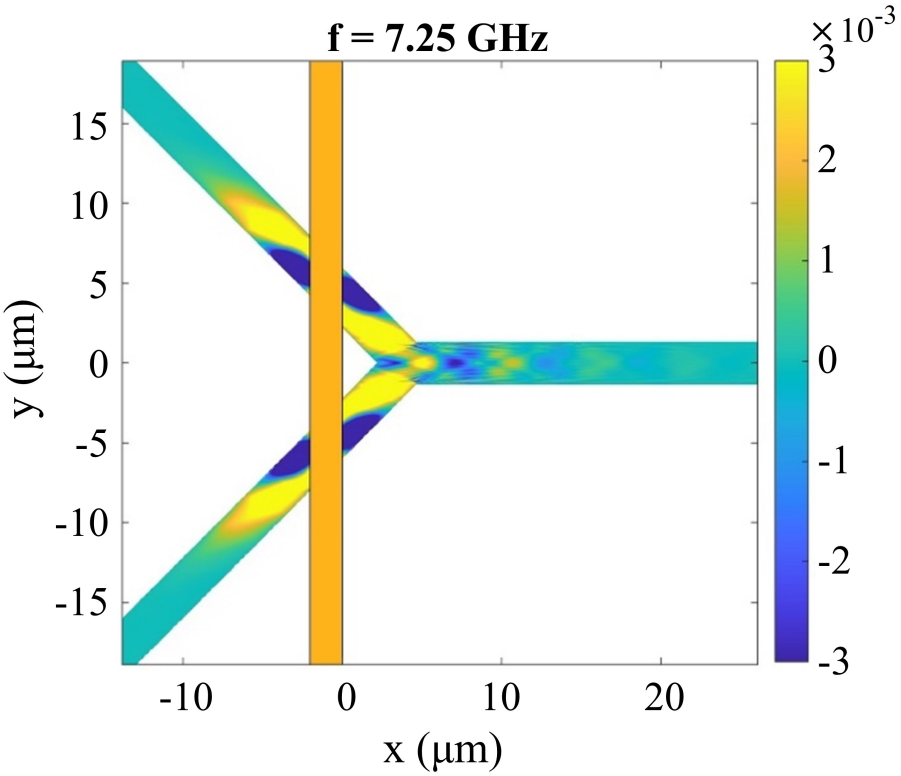

Figure A.2: Calculated spin wave amplitude vs. position for a Y-shaped magnetic structure with H along the antenna with f = 7.25 GHz and $\mu_0 h_0$ = 0.6 mT. The orange rectangle illustrates the location of the antenna and the colormap shows the z-component of the magnetization. (Multimedia view).

phase at x = 5 μm. For larger x the two modes separate in space because they have slightly different group velocities. The interference of these two modes leads to modulation of the amplitude vs. distance and to the bumps that are shown in Figure 6.2(c). In Figure A.3 (Multimedia view), the n = 2 mode is identifiable by the maximum and minimum observed at (5.2 μm, 0.4 μm) and (5.2 μm, -0.4 μm), respectively that move together along the microstrip. This change in the dominant modes with field angle suggests that there are opportunities not only for converting spin waves to larger k, but also for selection of the dominant width-quantized modes.

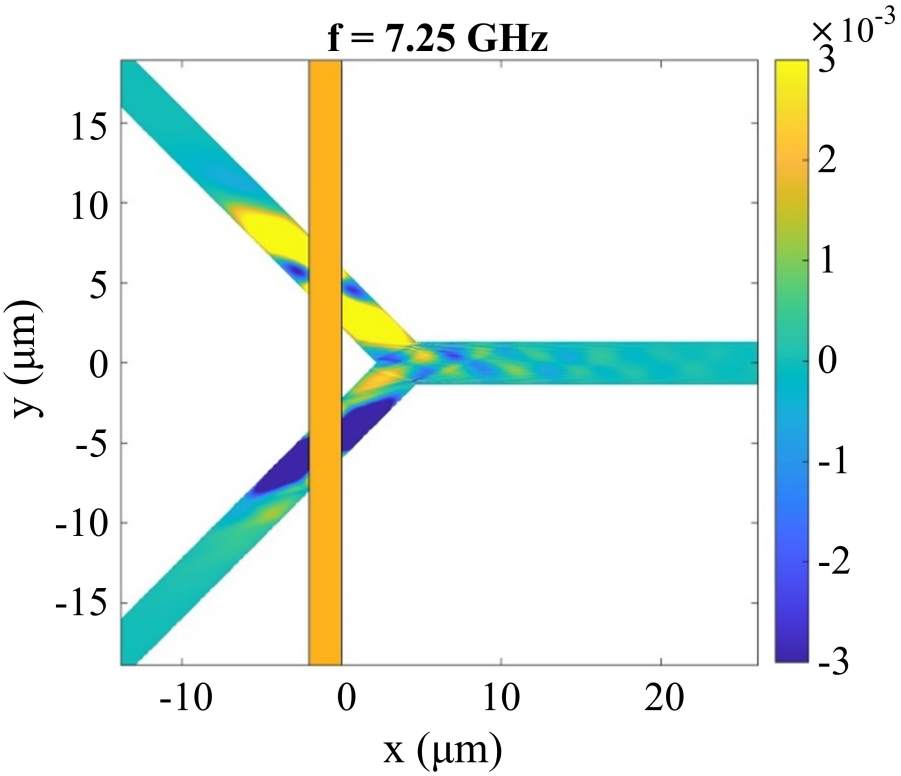

Figure A.3: Calculated spin wave amplitude vs. position for a Y-shaped magnetic structure with H at an angle of -3° with respect to the antenna with f = 7.25 GHz and $\mu_0 h_0$ = 0.6 mT. The orange rectangle illustrates the location of the antenna and the colormap shows the z-component of the magnetization. (Multimedia view).

Scaling of the up-conversion process in Y-structures

The scalability of the up-conversion process is important for applications. To estimate the up-conversion magnitude, spin wave dispersion relation calculations were used in combination with simple approximations for the demagnetization factors of the microstrip and the quantized wavevectors across the microstrip width w. Spin wave dispersion relations were calculated using the theory for magnetic thin films outlined by Kalinikos and Slavin [25]. Assuming that the magnetic strips are saturated in-plane with unpinned surface spins, Eqs. 45 and 46 along with A12 can be used to obtain the dispersion relations. Working in cgs units, the frequencies are

$$\omega_n^2 = \left(\omega_H + \alpha\omega_M k_n^2\right)\left(\omega_H + \alpha\omega_M k_n^2 + \omega_M F_{nn}\right) \tag{A.1}$$

where $\omega_M = \gamma 4\pi M_s$, $\omega_H = \gamma H$, γ is the gyromagnetic ratio, k_n is the net in-plane wavevector, defined in Figure A.4, and α is the exchange stiffness parameter ($\alpha = 2A_{\text{ex}}/M_s$, where A_{ex} is the exchange parameter used in micromagnetics, and M_s is the saturation magnetization). Normally k_n also includes the thickness-quantized wavevector k_z in the out-of-plane direction but for thin films with thickness L on the order of tens of nanometers, only the lowest-order thickness mode with $k_z = 0$ is observed experimentally. The parameter F_{nn} is

$$F_{nn} = P_{nn} + \sin^2\theta(1 - P_{nn}(1 + \cos^2\phi) + \omega_M \frac{P_{nn}(1 - P_{nn})\sin^2\phi}{(\omega_H + \alpha\omega_M k_n^2)} \tag{A.2}$$

where θ is the angle of the magnetization with respect to the surface normal and ϕ is the angle between $\overrightarrow{M}$ and $\overrightarrow{k}_n$ (see Figure A.4), and $P_{00} = 1 - \frac{1}{2}F_0$ with $F_0 = \frac{2}{k_n L}[1 - \exp(-k_n L)]$.

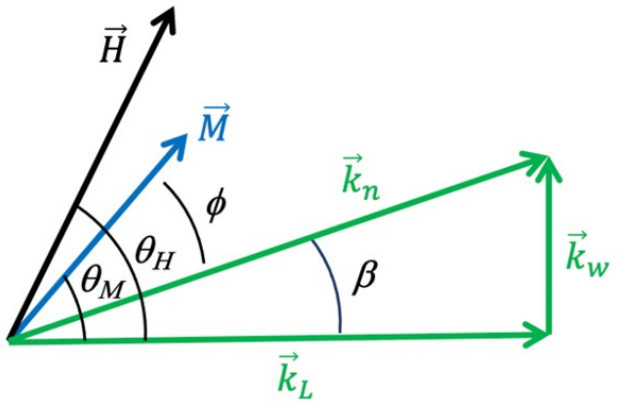

Figure A.4: Diagram illustrating the wavevector components where $\overrightarrow{k}_L$ is the component along the length of the microstrip, $\overrightarrow{k}_w$ is the quantized component along the width of the microstrip and $\overrightarrow{k}_n$ is the net wavevector. All vectors and angles are in the plane of the film. The magnetization $\overrightarrow{M}$ direction is set by a combination of the external magnetic field $\overrightarrow{H}$ and shape anisotropy.

The finite width of a magnetic micro- or nano-strip has two consequences that must be accounted for: the wavevectors are quantized across the width, and the sizeable static demagnetization field along the width. The wavevectors are quantized across the width with $k_w = n\pi/w_{\text{eff}}$, where $w_{\text{eff}} = w\left(\frac{D}{D-2}\right)$, $D\frac{2\pi}{p\left(1+2\ln\left(\frac{1}{p}\right)\right)}$, and $p = L/w$ [176, 197], and the net wavevector is the

vector sum of $\overrightarrow{k}_L$ and $\overrightarrow{k}_w$, so

$$k_n^2 = k_L^2 + k_w^2. \tag{A.3}$$

To account for the static demagnetization field along the microstrip width, $\omega_H = \gamma((H\sin\theta_H - N_w 4\pi M_s \sin\theta_M)^2 + H^2\cos^2\theta_H)$ is used, which is an approach that has been shown to describe DE spin waves [58]. Along the width, the demagnetization field is [198]

$$N_w = \frac{1}{\pi}\left(\frac{1-p^2}{2p}\ln(1-p^2) + p\ln(p) + 2\arctan\left(\frac{1}{p}\right)\right). \tag{A.4}$$

For long microstrips, the demagnetization factors along the microstrip length and in the out-of-plane direction are $N_l = 0$ and $N_z = 1 - N_w$, respectively. The angle of the magnetization θ_M is determined using the vector sum of the external field $\overrightarrow{H}$ and the static demagnetization field $\overrightarrow{H}_{\text{demag}}$, where $H_{\text{demag},w} = -N_w 4\pi M_s \sin\theta_M$ and $H_{\text{demag},l} = 0$.

To estimate the up-conversion magnitude as a function of w and H, dispersion relations were first calculated for $\theta_H = 45°$ and 90°. The up-conversion potential for a Y-shaped structure was then estimated by determining the wavevector in the DE-magnetized base of the Y that corresponds to the $k_L = 0$ frequency for $\theta_H = 45°$ for each w and H. Figure A.5 shows the results obtained for a film thickness of L = 40 nm and using material parameters for Permalloy: $M_s = 8 \times 10^5$ A/m (800 emu/cm^3), exchange $A_{\text{ex}} = 1.3 \times 10^{-11}$ J/m (1.3 μerg/cm), $\alpha = 3.25 \times 10^{-5}\,\mu\text{m}^{-1}$. Figure A.5(a) shows that N_w increases with decreasing w. As shown in Figure A.5(b), the magnetization is pulled towards the long axis of the nanostrip because of the shape anisotropy, and $\theta_M < \theta_H$ for $\theta_H = 45°$. This effect is more pronounced for smaller w. Conversely, for larger w and H, θ_M approaches θ_H. Figure A.5(c) shows the frequencies at $k_L = 0$ as a function of w for $\theta_H = 45°$ (the configuration in the arms) and $\theta_H = 90°$ (the surface wave/DE geometry). The $k_L = 0$ frequencies decrease with decreasing w in the DE geometry and increase with decreasing w for $\theta_H = 45°$, due in part to the differences in the static demagnetization fields. The wavevector in the base k_{base}, which is at the $k_L = 0$ frequency for $\theta_H = 45°$ represents the wavevector up-conversion magnitude. Figure A.5(d) shows that k_{base} increases dramatically for decreasing w. These calculations

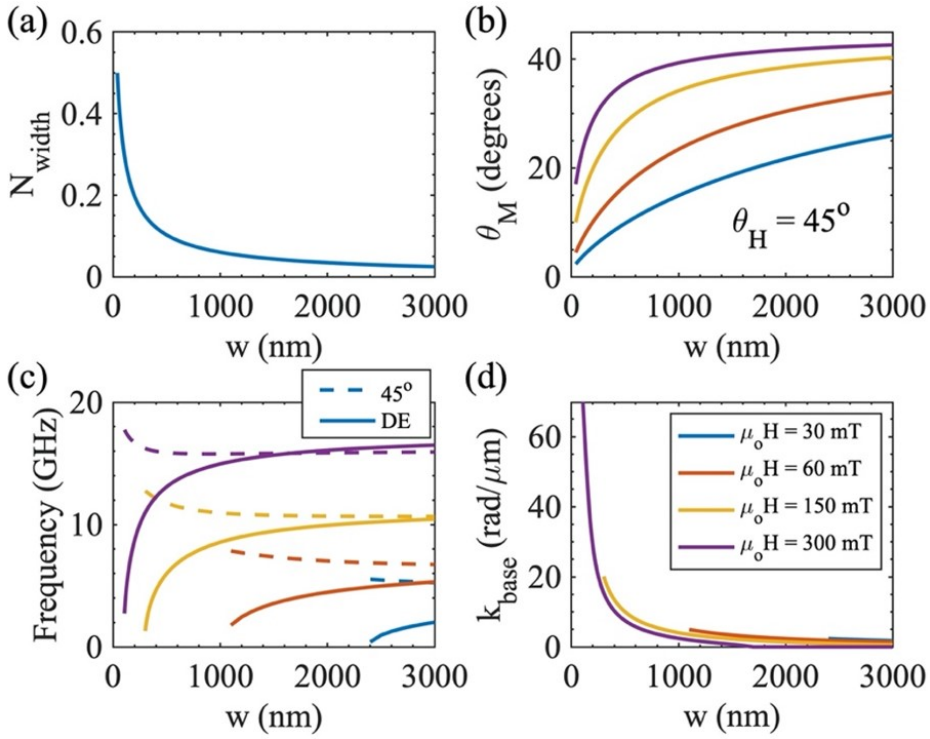

Figure A.5: (a) Demagnetization factor along the micro-or nano-strip width N_w vs. w. (b) θ_M vs. w for θ_H = 45° for H = 30, 60 150, and 300 mT. (c) The frequencies for k_L = 0 are shown for θ_H = 45° and for the DE case (θ_H = 90°) for the same H values considered in (b). Frequencies are shown only for the cases where H is sufficient to saturate the micro- or nano-strip. (d) The expected wavevector in the base k_{base} for k_L = 0 at θ_H = 45° provides an estimate of the expected wavevector up-conversion. The legend in (d) applies to (b), (c), and (d).

suggest that wavevector up-conversion of more than 70 rad/ μm is possible in Y-shaped structures, which can likely be extended further by optimizing the material, thickness, and the angle of the arms.